Cmv5^{s} Drives Inflammation and Macrophage Loss, Promoting Viral Infection-Induced Tissue Damage and Corrupting Protective NK Cell Immunity.

Jessica Lynne Annis-Bacon
Redford, Michigan

Master of Science, Colorado State University, 2016
Bachelor of Science, Eastern Michigan University, 2014

A Dissertation presented to the Graduate Faculty of the University of Virginia in Candidacy for the Degree of Doctor of Philosophy

Department of Microbiology, Immunology and Cancer Biology

University of Virginia
May 2024

Table of Contents

Abstract

MHC class I (MHC-I) molecule H-2D^k conveys resistance to murine cytomegalovirus (MCMV) infection in both C57L and MA/My mice, mediated by a subset of NK cells bearing the H-2D^k-binding Ly49G2 receptor. M.H2$^{k/b}$ mice are MA/My congenic aside from a C57L-derived region surrounding the MHC, which dominantly drives susceptibility and tissue damage during MCMV infection, despite expression of H-2D^k and presence of Ly49G2+ NK cells. The interval for which the M.H2$^{k/b}$ mice are heterozygous is denoted *Cmv5*, while the C57L-derived phenotype-associated haplotype is referred to as *Cmv5*^{s}. The originally described *Cmv5*^{s} interval encompassed the entire MHC region and many other genes that could be driving pathology. To determine the role of the MHC and associated sub-regions, we generated and tested several *Cmv5*-recombinant strains, substantially narrowing the phenotype-associated interval and cementing the contribution of at least 2 independent loci to *Cmv5*^{s} pathology during infection. *Cmv5*^{s} corrupts the ability of otherwise protective Ly49G2+ NK cells to control MCMV infection. To determine how this may be occurring, we asked at what stage of the immune response *Cmv5*^{s} inhibits NK cell function. We found no differences in NK cell phenotype or function prior to infection, and no *Cmv5*^{s}-driven defects in the early activation or expansion of the Ly49G2+ subset. By 4 days post infection (dpi), *Cmv5*^{s} NK cells had increased expression of activation markers and checkpoint receptors, however there was no loss of functionality when stimulated *in vitro*. Marginal zone (MZ) histopathology consistent with necrosis was the first apparent *Cmv5*^{s} phenotype, occurring prior to divergence in weight loss, viral load, or NK cell phenotype, and progressing to a widespread loss of spleen cellularity by 4dpi. Following this earliest *Cmv5*^{s}-driven phenotype, we found increased neutrophil infiltration, death, and oxidative

stress at the MZ, along with increased global IL-6 and TGF-β1 in *Cmv5*^{s} spleens by 2dpi. Neutrophils were required for increased cell death and oxidative stress, but not necrotic MZ histopathology, leading us to ask about the state of other MZ populations at this timepoint. Marginal zone macrophages (MZMs), but not similarly localized stromal cells, were lost in both strains by 2dpi, and analysis at 36 hours post infection (hpi) revealed infection of SIGNR1+ MZMs and recruitment of neutrophils to areas of increased MCMV positivity and spread. Depletion confirmed that macrophages were required for MZ neutrophil recruitment and the differences between strains in spleen IL-6 and TGF-β1. By 4dpi, *Cmv5*^{s} spleens showed buildup of MZM debris and substantial red pulp macrophage loss with widespread oxidative stress. These data identify macrophage loss and inflammation mirroring the spatial and temporal appearance of *Cmv5*^{s}-driven tissue damage in the spleen during acute MCMV infection. Bringing our data together into a model of how *Cmv5*^{s} may drive pathology during MCMV infection, we conclude that macrophage activation and loss underlie spleen histopathology, and are likely the primary targets of *Cmv5*^{s}. This *Cmv5*^{s}-modified tissue environment marked by increased cell death, oxidative stress, and inappropriate inflammation further serves to inhibit NK cell function, preventing effective viral control.

Acknowledgements

First of all, I'd like to thank my mentor Dr. Michael Brown, who dragged me kicking and screaming into the world of immunogenetics, giving me a beautiful puzzle of a mouse model with the freedom to explore it as my interests, and the data, led the way. You have been a patient and supportive mentor, and I am incredibly grateful to have gotten the opportunity to work with and learn from you these past several years.

I am also grateful to the current and former members of the Brown Lab: Shreya Jetty, Anna Kuzma, Rowena Crittenden, Rene Menchaca, Dr. Jack Cronk, and Dr. Awndre Gamache, who have provided technical and administrative assistance, as well as thoughtful discussions during lab meetings. In this line, a special shout-out goes to John Benjamin Duncan, who provided an incredible amount of assistance during his rotation with us.

I'm very fortunate to have had a wonderful thesis committee, Dr. Victor Engelhard, Dr. James Zimring, Dr. Sara Ewald, and Dr. Ulrike Lorenz have provided invaluable feedback and discussion throughout my PhD work. I want to give additional thanks my thesis committee chair, Dr. Victor Engelhard, and Dr. James Zimring, who have given additional time and energy offering advice and helping me to improve my research outside of the committee.

Sheri VanHoose and Lisa Vohwinkel at the UVA Research Histology Core have been an enormous resource, and over the last 5 years have done an incredible amount of tissue embedding, H&E staining, and cryosectioning, which has allowed me to progress the work I've outlined herein. I am very grateful to them and their contribution to this research. Additionally, I am grateful to Helen Billcheck and Jeremy Gatesman from the UVA Center for Comparative Medicine, who have provided assistance with various mouse treatments.

Last, but certainly not least, I would like to thank my family: my incredible husband and partner, Michael Bacon, and our cats, Smores and Cicero. Michael, you have gone above and beyond to encourage and support me, being a constant source of comfort, light, and

love at every step of this journey. Words cannot describe how grateful I am for you and everything you've done for me, and I wouldn't be where I am today without you.

List of Figures

List of Tables

Abbreviations

4HNE	4-Hydroxynonenal
cCasp	Cleaved Caspase 3
cLy6G	Ly6G+ Neutrophil Clusters
DAMP	Damage-Associated Molecular Pattern
dpi	Days Post Infection
GWAS	Genome-Wide Association Studies
hpi	Hours Post Infection
IEI	Inborn Errors of Immunity
IF	Immunofluorescent
IFN	Interferon
MCMV	Murine Cytomegalovirus
Mb	Megabase
MHC	Major Histocompatibility Complex
MHC-I	MHC Class I Molecule
MHC-II	MHC Class II Molecule
MZ	Marginal Zone
MZM	Marginal Zone-Localized Macrophage
MZRC	Marginal Zone Reticular Cell
NKC	Natural Killer Cell Gene Complex
NWP	Non-White Pulp
PAMP	Pathogen-Associated Molecular Pattern
PCG	Protein-Coding Genes
PRR	Pattern Recognition Receptor
QTL	Quantitative Trait Loci

RPM Red Pulp Macrophage

RS Reactive Species (Reactive Oxygen/Nitrogen Species)

TUNEL Terminal Deoxynucleotidyl Transferase dUTP Nick End

UHD Ultra-High Dose

Chapter I: Introduction

Host Genetics Influence Outcomes of Viral Infection.

It has long been appreciated that host genetic makeup plays an important role in the development of disease during infections, contributing to the variation in outcomes between individuals exposed to the same pathogen[1]. Mutations that prevent the appropriate function of key immune mediators or pathways are associated with severe disease during infections[2], however mutations with less overt functional implications, such as a small increase in binding affinity to a ligand or cell signaling molecule, can also significantly alter the strength or functional output of an immune stimulation[3-5]. While mutations leading to smaller differences in protein function don't always have noticeable global effects by themselves, combinations of small effects can lead to larger downstream differences in the development of infection-induced pathology. Viruses, as obligate intracellular pathogens, are intricately intertwined with the life and functions of their host cell, with progression of infection driving interaction of viral factors with many aspects of host cell biology[6]. Genetic variation in any of these factors mediating host-virus interaction has the ability to create an intracellular environment that is more or less permissive to viral infection and replication, which can have significant impacts on the development of infection-associated disease. In addition to host-virus interactions, the antiviral immune response requires a complex communication network between the infected cell and

surrounding non-immune tissue cells, as well as local and systemic immune mediators. During viral infection, the host needs to be able to recognize the presence of a pathogen, distinguish between healthy and infected cells, develop a coordinated response that eliminates the invading pathogen with minimal collateral damage, and then shut down once that pathogen has been cleared. Genetic variation in any one of these pathways has the potential to tip the balance away from an effective and appropriate antiviral immune response, toward tissue damage, long term-morbidity, and death.

Monogenic defects in various parts of the immune response that lead to the development of severe disease are known as inborn errors of immunity (IEIs). IEIs have been noted since the advent of genetic screening, and as the technology has become more advanced and the practice more widespread, IEIs have been identified in nearly every aspect of the antiviral immune response[7, 8]: from innate antiviral sensing and interferon signaling to the activation of innate and adaptive immune cells and their ability to exert effector functions. IEIs in antiviral response mechanisms carry the ability to make individuals more susceptible to viral infections, but are also implicated in many instances of chronic inflammatory disorders and autoimmunity[7]. Characterization of IEIs and associated phenotypes have provided key insights into how genetic variation can contribute to disease severity upon infection, but IEIs involving these key immune mediators are rare, and even when found they do not present complete phenotypic penetrance or homogeneity[9]. Overall, monogenic IEIs cannot account for the majority of variation in patient response to viral infections[10, 11].

While IEIs are associated with larger downstream impacts on disease, variability in the immune response can also come from polymorphisms that don't necessarily lead to

noticeable defects in immunity by themselves[12]. Polymorphism in antiviral immune mediators can lead to variability in the ability of these mediators to bind targets and induce signaling pathways, and due to the complex communication mechanisms required during an antiviral immune response, polymorphisms have the combined ability to cause meaningful differences in the response to even an identical immune stimulus[13]. Variations between humans are found throughout immune pathways[14], and these variations, despite not necessarily conveying a singular phenotype, can interact with other polymorphisms and pathways that change the progression of the immune response, leading to differences in response to infection based on host genetic makeup. Bioinformatic analyses have begun assessing these polygenic risk factors, or how combinations of different gene mutations can lead to increased risk of severe disease upon infection[12]. Despite potential promise, these approaches are limited by our understanding of genetic heritability, interactions, and the development of disease pathology, as well as the need for large sample sizes and diverse populations[15, 16].

The major histocompatibility complex (MHC) is a highly polymorphic and gene dense region that spans 3-4 Mb and houses a myriad of immune-relevant mediators, including those involved with antigen presentation, cellular metabolism, cell signaling pathways, and inflammation[17, 18]. The MHC is functionally and mostly organizationally conserved between mice and humans[19], with variation in this region associated with a variety of disease outcomes, including many viral infections[20, 21]. Among the immunological mediators found within the MHC are MHC class I (MHC-I) and MHC class II (MHC-II) molecules, which are critical for immune surveillance and activation, particularly during innate immunity to intracellular pathogens or cancer[22-24] and antigen specific adaptive immunity[25-27]. Most nucleated cells express MHC-I on their cell surface, functioning as a marker of “self” and

presenting samples of the intracellular proteome extracellularly, allowing immune system access to the otherwise hidden intracellular environment for surveillance of pathogens[28]. There are several highly polymorphic MHC-I genes in the MHC, and this genetic variation is important in allowing the immune system to recognize a variety of different antigens[29, 30]. Outcomes of many viral infections are associated with the MHC region, but very few of these diseases can be traced back to any one gene variant or protein polymorphism[20, 31], suggesting that intra- and extra- MHC interactions may be an important yet poorly understood determinant of disease pathology. A better understanding of how genetic and molecular interactions can be changed by polymorphism, and how these changes impact cell- and tissue-level function to promote pathology, will be required to translate the identification of genetic risk factors and use of genetic screening to the development of effective medical interventions.

Genome-wide association studies (GWAS) seek to use the overwhelming amount of genetic variability in populations to hone in on mutations and regions that are linked to disease progression. While GWAS has led to the discovery of important genetic risk factors associated with severe disease, it has problems with highly polymorphic, gene dense regions such as the MHC[32]. Many of these issues come from the associated heritability of these regions (linkage disequilibrium), and how variation in genes can influence other genes, which manifest phenotypes in cells and tissue (epistasis), causing pathology[32, 33]. Much of biomedical research is conducted using a handful of inbred mice and closely related sub-strains, maintaining controlled genetic backgrounds to minimize variables for the study of the immune response and progression of infection *in vivo*. Unfortunately, this elimination of genetic variability undermines the importance of genetic makeup as a factor in disease progression, and the focused development of scientific and

genetic tools in these specific strains has hindered the ability of researchers to study models outside these systems. The collaborative cross is a system of mouse interbreeding that seeks to introduce large amounts of genetic variation into a population of mice, who then can be used for GWAS analysis[34]. Use of the collaborative cross has proven highly informative to bringing some of the genetic information we have regarding human datasets into more easily manipulatable mouse models[34], however, these systems suffer from the same complications that arise with population level analysis of genetic variability and responses in humans, which when coupled with the availability of fewer tools in these mixed genetic backgrounds, limits the usability of these mice for more in depth analysis of genetic pathways. Prior to the development of targeted genetic tools and large-scale sequencing, researchers used inter mouse breeding and backcrossing to isolate regions associated with a phenotype, and then moved backwards from the phenotype to ascertain mechanism (forward genetics). Substantial discovery has been made using this method[35], and its coarse genetic mapping allows for better interrogation of interacting genetic factors than fine mapping approaches such as large scale GWAS. Additionally, the generation and testing of mice with known region polymorphisms on otherwise homogenous backgrounds allows a greater level of control than use of the collaborative cross, without reverting to completely homogenous inbred mouse populations.

Overall, host genetics play an important role in the pathology of viral infections, with the ability to predispose individuals to more or less severe outcomes. The extent of host cell-virus interactions and complex communication mechanisms used by the immune system makes polymorphism within many aspects of cell biology and immunity potentially relevant to viral pathology. In addition, gaps in our understanding of linkage disequilibrium and epistasis within highly polymorphic immune-relevant regions compounds the complexity

of potential genetic involvement, contributing to missing disease heritability. Phenotype-driven coarse genetic mapping methods have the ability to offer unique insights into understanding these regions and their contributions to viral infection outcomes without completely sacrificing the benefits of inbred backgrounds. Together, a better understanding of how host genetic makeup influences the immune response and outcomes of viral infection serves to aid in the identification high-risk individuals and to increase our overall understanding of how viruses interact with their host cell and the immune system, leading to the development of more effective medical interventions.

Mechanisms of Viral Infection-Induced Tissue Damage.

Severe outcomes of viral infections are caused by the accumulation of damage in host tissues that drive cell death and prevent proper function. This pathology highlights the delicate immunological balance between host defense, or the desire to eliminate invading pathogens, and self-tolerance, or the need to protect host tissues. The immune response to a viral infection can cause tissue damage if not properly controlled through excess/prolonged inflammation or direct cell-mediated autoimmunity[36-39]. Insufficient immune activation or inappropriate inhibition also has the ability to drive tissue damage by allowing the virus to spread uncontrolled through tissues[37, 40, 41]. Tissue damage is a major cause of morbidity and mortality during viral infections, and a better understanding of how viral infection leads to tissue damage in different contexts is instrumental to the development of medical interventions to treat and prevent severe viral disease.

Tissue damage caused by the immune system is referred to as immunopathology, and can occur through many different mechanisms during viral infections. Inflammation is an

important part of the immune response to a pathogen; however, accumulation of excess inflammation can lead to cell death and tissue damage via cytokine-induced death pathways, buildup of oxidative stress, and via directly toxic immune mediators. Cytokine-induced cell death is associated with interferons (IFNs)[42-44] as well as classical inflammatory cytokines TNFα[45-47] and IL-6[48, 49], and some damage-associated molecular patterns (DAMPs)[50-53]. Inflammation is heavily associated with oxidative stress, which occurs when the generation of reactive species (RS) overwhelms a cell's ability to detoxify them, which can lead to cell damage and death[54, 55]. RS are produced during myeloid cell activation, particularly in macrophages and neutrophils, and are important for killing extracellular and phagocytosed microbes[56, 57], however the benefit of RS during viral infections is not as well defined and generally associated with tissue pathology[57]. Toxic mediators, such as those found in granulocyte granules or neutrophil extracellular traps, are used to combat pathogen survival in the extracellular space by chelating important cofactors, driving oxidative stress, and breaking down pathogen macromolecules[58-60]. While potently antimicrobial, these factors are generally not explicitly pathogen-targeted, and are associated with host tissue damage during disease[61-66]. Overall, while inflammatory factors are important for host control of viral infections, they are also associated with pathology and severe disease. Genetic predisposition of certain individuals to damaging inflammatory responses have been documented in many viral diseases[8, 67, 68], but often verified mechanisms of action for these risk factors are missing.

Effective antiviral immunity requires the killing of infected host cells, generally through the activation and targeting of cytotoxic lymphocytes such as NK cells and CD8+ T cells[69, 70]. These processes are highly regulated; however, dysfunction can occur at any point in the process, leading to targeted autoimmunity and tissue damage. Viral infection-induced

autoimmune disorders are documented, and generally associated with genetic susceptibility[39], however mechanisms of action for the genetic risk factors are largely uncharacterized.

While immunopathology is a prominent cause of severe outcomes during viral infections, tissue damage can also be directly mediated by lack of an appropriate antiviral response, resulting in uncontrolled viral spread. Individuals with immune impairments leading to the development of severe disease during infections are referred to as immunocompromised, and this immunocompromised status can be conveyed by genetics (primary immunodeficiencies/inborn errors of immunity)[7], as well as presence of other diseases, certain medical treatments, and physiological states (secondary immunodeficiencies)[71]. In these cases, tissue damage and severe outcomes of infection can come directly from viral infection and spread through tissues. Mechanisms of action for severe disease in immunocompromised patients can vary based on the mechanism of immune impairment and the pathogen itself, with some mechanisms better understood than others. Overall, tissue damage during viral infection can occur via several mechanisms, and many of these mechanisms have genetic links that are incompletely understood. Further research into how host genetic makeup influences antiviral immunity and the development of tissue damage is critical toward the development of therapeutics to prevent and protect from severe viral disease.

Regulation and Function of NK Cells in Antiviral Immunity.

NK cells are innate lymphocytes important for antiviral immunity that parse signals from germline encoded activating and inhibitory receptors to mediate effector functions[72]. Upon

activation, NK cells are able to directly recognize and kill virally infected cells via receptor-mediated induction of apoptosis[73-75] or through the release of cytotoxic granules containing perforin and granzymes[73, 76, 77]. Activated NK cells secrete important antiviral cytokine IFNγ and inflammatory TNFα[78], as well as GM-CSF and various chemokines[79] important for the recruitment and activation of myeloid and other immune cells. NK cells are required for resistance in preclinical models of viral disease[80], and humans with NK cell deficiencies or defects in function display increased susceptibility to viral infections[81]. This data highlights the importance of NK cells in the antiviral immune response, and opportunities for modulation of NK cell function in the treatment of many viral diseases.

NK cells are responsive to many cytokines[82], allowing the tissue environment to tune NK cell activation and function depending on the context of insult. In line with their antiviral functionality, NK cells are highly activated by type I IFNs, which are early antiviral factors produced by tissue cells upon infection[83, 84], and IL-12 and IL-18, which are produced by activated myeloid cells[85]. These factors serve to potently increase NK cell cytotoxicity and IFNγ production, respectively. As effector cells predominantly associated with a “type 1” immune response to intracellular pathogens, “type 2” cytokines predominantly associated with an extracellular pathogen, such as IL-4[86] and IL-6[87] can serve to inhibit NK cell function, directing the immune response to more appropriate mediators for that type of threat. Just as important as the initiation of immunity is its resolution, and inhibition of NK cells has been demonstrated upon exposure to cytokines associated with the resolution of inflammation, such as TGF-β[88]. Together, NK cell function is regulated by the tissue environment, and an inappropriate environment has the potential to prevent effective NK cell-mediated immunity.

NK cell cytotoxicity is mediated by inhibitory and activating receptors that allow them to distinguish between healthy and virally infected cells in tissues[23]. Activating receptors expressed by NK cells generally bind ligands associated with cell stress[89-93] and viral infection[94-97]. To minimize inappropriate activation, NK cells also express a variety of inhibitory receptors that bind ligands expressed on healthy host cells, including self MHC-I[23, 98, 99]. As potentially damaging cytotoxic effector cells, NK cells upregulate additional inhibitory receptors upon activation, serving as checkpoints to disable effector functions and protect host tissues[100]. NK cell expression of inhibitory checkpoint receptors TIM-3[101-103], TIGIT[104, 105], and LAG-3[106, 107] are noted, binding ligands such as phosphatidylserine on apoptotic cells and cell debris, damage associated molecular patterns (DAMPs), cell adhesion molecules, and MHC-II[100]. While checkpoint receptors are important for protecting host tissues during an immune response, increasing upregulation of these receptors prior to threat clearance can prevent effective immunity.

NK cells express inhibitory MHC-I-binding Ly49 receptors in variegated patterns, with individual cells expressing different numbers and combinations of receptors[108]. Genes for these receptors are located within the natural killer cell gene complex (NKC), which displays a considerable amount of polymorphism[109], similar to their ligands encoded within the MHC. NK cells expressing an inhibitory Ly49 molecule that binds to host MHC-I are considered licensed on that molecule, and licensed NK cells are more tuned to recognize and respond to instances of MHC-I downregulation ("missing self")[23, 24], a commonly used immune evasion mechanism, and viral alterations to MHC-I molecules ("altered self")[110]. In line with this, certain pairs of Ly49/MHC-I, or analogous human KIR/HLA genes, are associated with protection from severe outcomes during highly clinically relevant viral infections such as human immunodeficiency virus (HIV)[111, 112] and hepatitis viruses[113-115],

as well as oncogenic viruses such as human papilloma virus (HPV)[116]. Despite abundant evidence alluding to the importance of NK cell licensing in viral infection outcomes, how these NK cells convey protection and why certain pairings are more protective than others is not well understood. Additionally, not every patient with a protective genotype will display phenotypic resistance to infection, suggesting that genetic and/or environmental differences can modify this protection through mechanisms that remain to be fully investigated. A better understanding of how licensed NK cells convey protection against viral infection and what interferes with their ability to drive resistance in different hosts and environmental contexts serves to aid in the development of more effective therapeutics for many damaging viral diseases.

Acute MCMV Infection in the Spleen.

The spleen is an intricately organized secondary lymphoid organ with key roles including the surveillance of blood for damaged/dying cells and pathogens[117]. The white pulp of the spleen predominantly contains cells involved with adaptive immunity, home to large populations of T cells, B cells, and dendritic cells organized similarly to a lymph node[117, 118]. This is in contrast to the red pulp, which contains innate immune cells such as NK cells, granulocytes, and monocytes[117, 118]. The marginal zone (MZ) is a distinct structure that lies between these compartments straddling the marginal zone sinus, a major site of blood flow into the spleen, functioning in blood surveillance and bridging the adaptive and innate compartments[117]. The spleen is home to many specialized macrophage populations, including MZ-localized macrophage populations (MZMs) marked by expression of SIGNR1 and/or CD169[119] and red pulp-localized macrophages (RPMs) marked by F480 and CD68[120]. The architectural setup of the spleen places MZMs as direct

mediators between innate and adaptive immunity, with key functions in the clearance of pathogens from the blood[121-125], cooperation with dendritic cells to induce adaptive immune responses[122, 126, 127], and the induction of tolerance to apoptotic cell-associated antigens[128]. RPMs play important roles in in clearance of damaged/dying red blood cells[120, 129], maintenance of splenic structure[130], and stress-induced extramedullary hematopoiesis[131]. Overall, the spleen is an important immune organ that relies on different populations of specialized macrophages for optimal function at homeostasis and during infection.

Murine cytomegalovirus (MCMV) is a large, dsDNA β-herpesvirus that predominantly infects myeloid, stromal, and parenchymal cells[132], with the ability to spread to various tissues throughout the body via circulating myeloid cells[133, 134]. The spleen is an important early reservoir for MCMV infection, and splenectomized mice displayed reduced systemic infection and mortality[135]. MCMV enters the spleen hours after infection at the MZ, and spreads into the red pulp starting around 2dpi[136]. While there is evidence that MCMV may infect marginal zone stromal cells early during infection, they do not appear to be the predominant infected cell type for spleen replication and progression[136]. Despite decades of research using MCMV, early progression of infection through cells in the spleen is not well characterized. Spleen and liver histopathology have been noted during acute MCMV infection in susceptible mice[137], however the cellular and/or molecular mediators of this phenotype remain mostly uncharacterized. As time progresses, MCMV spreads systemically, infecting cells in most major organs, where it will establish latency[138, 139]. The importance of the spleen as an early reservoir and the association of MCMV with multiple organs suggests that a better understanding of how spleen pathology develops during

early infection has the potential to offer widespread insights into mechanisms of infection-induced tissue damage throughout the body.

Cmv5^{s} Corrupts H-2D^{k}-Mediated MCMV Resistance and Drives Spleen Histopathology During Acute MCMV Infection.

MCMV has been used to study genetic regulation of NK cell-mediated immunity, as NK cells are required for acute viral control[140-142], and different inbred mouse strains vary in levels of resistance or susceptibility to the virus[142, 143]. Much of this variability is due to the highly polymorphic Major Histocompatibility (MHC) and Natural Killer Cell (NKC) genetic regions[143, 144], encoding MHC class I (MHC-I) molecules and Ly49 receptors, respectively. MA/My and C57L mice have NKC-Ly49 haplotypes that are very similar[109], however MA/My (H-2^{k}) mice are much more resistant to MCMV infection than C57L (H-2^{b}) mice[142]. Previous work identified MHC-I molecule H-2D^{k} in MA/My mice, which interacts with inhibitory Ly49G2 receptor on NK cells to mediate protection against MCMV infection[145-147]. These Ly49G2+ NK cells licensed on H-2D^{k} show substantial expansion with increased activation and effector function during acute MCMV infection *in vivo* compared to Ly49G2- counterparts[145, 147]. Importantly, this protection mediated by Ly49G2+ NK cells can be transferred to C57L mice with genetic addition of the H-2D^{k} molecule[146].

M.H2$^{k/b}$ mice are identical to MA/My parent strain aside from heterozygosity for a C57L-derived region surrounding the MHC on chromosome 17[148]. Despite the expression of H-2D^{k} and the presence of effector Ly49G2+ NK cells, M.H2$^{k/b}$ mice display increased susceptibility to acute MCMV infection over MA/My counterparts[149]. The genetic interval for which M.H2$^{k/b}$ mice are heterozygous is referred to as *Cmv5*, while the C57L-derived

haplotype that conveys susceptibility to MCMV infection is denoted *Cmv5*^{s}. The presence of *Cmv5*^{s} does not convey increased MCMV susceptibility in H-2D^{k} transgenic C57L mice or MA/MyxC57L F_1 hybrid mice[149-151], demonstrating the presence of a dominant mitigating factor within the C57L background. This contribution of multiple loci within the MHC to antiviral immunity with a consideration for genetic background mirrors previously reported observations in MCMV[143] and other viruses[152, 153]. These reports suggest that further exploration of intra- and extra- MHC interactions is relevant not only to MCMV in MA/My background mice, but in other models of viral pathology in various genetic backgrounds. In addition to the relevance in preclinical models, human genetic risk factors are rarely completely penetrant, and a better understanding of how polymorphism can modify the ability of a gene or genetic region to covey a phenotype offers insight into potential mechanisms[154].

In addition to the increased MCMV susceptibility, *Cmv5*^{s} was also noted to significantly disrupt splenic architecture by 4dpi[149]. Histologically, it was noted that the distinct marginal zone structures seen in the spleens of uninfected mice were no longer well defined, and that *Cmv5*^{s}-bearing spleens had an additional loss of cellularity in the red pulp with increased evidence of infection and necrosis[149]. This *Cmv5*^{s}-driven spleen histopathology was seen in M.H2^{b} mice (homozygous for *Cmv5*^{s}) with or without an H-2D^{k} transgene, and in M.H2$^{k/b}$ mice[149], demonstrating a dominant presentation on the MA/My background that was not dependent on H-2D^{k}. Depletion of Ly49G2+ NK cells was unable to alleviate spleen histopathology in M.H2^{b}-D^{k} mice, and depletion of MA/My mice was unable to induce it, suggesting a mechanism independent of Ly49G2+ NK cells[149]. Further assessment of the spleen at 4dpi in M.H2^{b} and M.H2^{b}-D^{k} mice by immunofluorescent (IF) imaging revealed apparent disorganization of the white pulp T and B cell zones and

abnormal NK cell morphology in *Cmv5*^{s}-bearing mice[149]. While this data provides insight into the disruption of spleen structure, there was minimal to no assessment of marginal zone and red pulp populations that may be behind *Cmv5*^{s} histopathology. The entirety of available data regarding *Cmv5*^{s}-driven structural disruption in the spleen is confined to *Cmv5*^{s} homozygous mice in a single figure and supplemental sub-figure[149], identifying a phenotype without much of any additional exploration. As tissue damage and dysfunction are the major causes of severe outcomes during viral infection, additional understanding of this phenotype is potentially highly clinically relevant.

Thesis Rationale

Host genetics play an important role during viral infections and have the ability to predispose individuals to more or less severe outcomes[155]. The MHC is a highly polymorphic and gene dense region with associations to many human diseases with incomplete penetrance[20], and mouse models have identified polymorphism in MHC-associated regions with consideration for genetic background in the pathology of MCMV[143] and other viruses[152, 156]. *Cmv5*^{s} drives acute MCMV susceptibility and spleen tissue damage in M.H2$^{k/b}$ mice despite the presence of an MHC-I/Ly49 genetic pair associated with licensed NK cell-mediated protection[149]. Identification of the genetic mediator or mediators behind *Cmv5*^{s}-driven MCMV susceptibility and tissue damage is of key importance, particularly given the clinical relevance of MHC polymorphism, tissue damage, and viral infection outcomes. As translation of findings into human patient populations is unlikely to come at the genetic level, an understanding of how genetic drivers of *Cmv5*^{s} lead to changes in protein-level mediators that regulate cellular functions and tissue pathology, will also be required. This works seeks to increase our

understanding of how MHC polymorphism can corrupt otherwise protective NK cell-mediated antiviral immunity and drive tissue damage in the spleen during acute MCMV infection.

Chapter II: Multiple Immune and Genetic Mechanisms Contribute to *Cmv5*^{s}-Driven Susceptibility and Tissue Damage during Acute MCMV Infection

Abstract.

The MHC class I (MHC-I) molecule H-2D^{k} conveys resistance to acute murine cytomegalovirus (MCMV) infection in both C57L (H-2D^{k} transgenic) and MA/My mice. M.H2$^{k/b}$ mice are MA/My background aside from a C57L-derived region spanning the MHC (*Cmv5*^{s}), which diminishes this resistance and causes significant spleen histopathology. To hone in on the effector elements within the *Cmv5*^{s} interval, we generated several *Cmv5*-recombinant congenic mouse strains and screened them *in vivo*, allowing us to narrow the phenotype-associated interval more than 6 times and segment the genetic mechanism to at least 2 independent loci within the MHC region. In addition, we sought to further characterize the *Cmv5*^{s}-associated phenotypes in their temporal appearance and potential direct relation to viral load. To this end, we found that *Cmv5*^{s} histopathology and NK cell activation could not be fully mirrored in the MA/My mice with increased viral dose, and that marginal zone destruction was the first apparent *Cmv5*^{s} phenotype, being reliably quantified as early as 2 days post infection (dpi) in the M.H2$^{k/b}$ mice, prior to divergence in viral load, weight loss, or NK cell phenotype. Finally, we further dissect NK cell involvement, finding no intrinsic differences in NK cell function, despite increased upregulation of activation markers and checkpoint receptors. In conclusion, these data dissect the genetic and immunologic underpinnings of *Cmv5* and reveal a model in which polymorphism within the MHC region of the genome leads to the development of tissue damage and corrupts protective NK cell immunity during acute viral infection.

Key Points.

Cmv5^{s}, comprising the MHC, impedes NK cell control of acute MCMV and drives tissue damage.

Neither major MHC-I locus alone is sufficient to convey *Cmv5*^{s} susceptibility and damage.

Cmv5^{s} NK cells display increased upregulation of activation markers and checkpoint receptors.

Cmv5^{s} splenic damage precedes divergence in weight loss, viral load, or NK cell phenotype.

The Work in this Chapter is Published in the Journal of Immunology:

Annis JL, Duncan JBW, Billcheck HO, Kuzma AG, Crittenden RB, Brown MG. Multiple Immune and Genetic Mechanisms Contribute to *Cmv5*^{s}-Driven Susceptibility and Tissue Damage during Acute Murine Cytomegalovirus Infection. J Immunol. 2024 Jan 15:ji2300648. doi: 10.4049/jimmunol.2300648. PMID: 38224204.

Co-Author Contributions.

Anna G. Kuzma and Rowena B. Crittenden did most of the mouse genotyping, which resulted in their identification of the *Cmv5*-recombinant strains tested in this work. Anna additionally assisted in running a couple PCRs for viral load. Helen O. Billcheck assisted in some of the MCMV injections. John Benjamin W. Duncan assisted in piloting the *in vitro* NK cell stimulation assay.

Graphical Abstract.

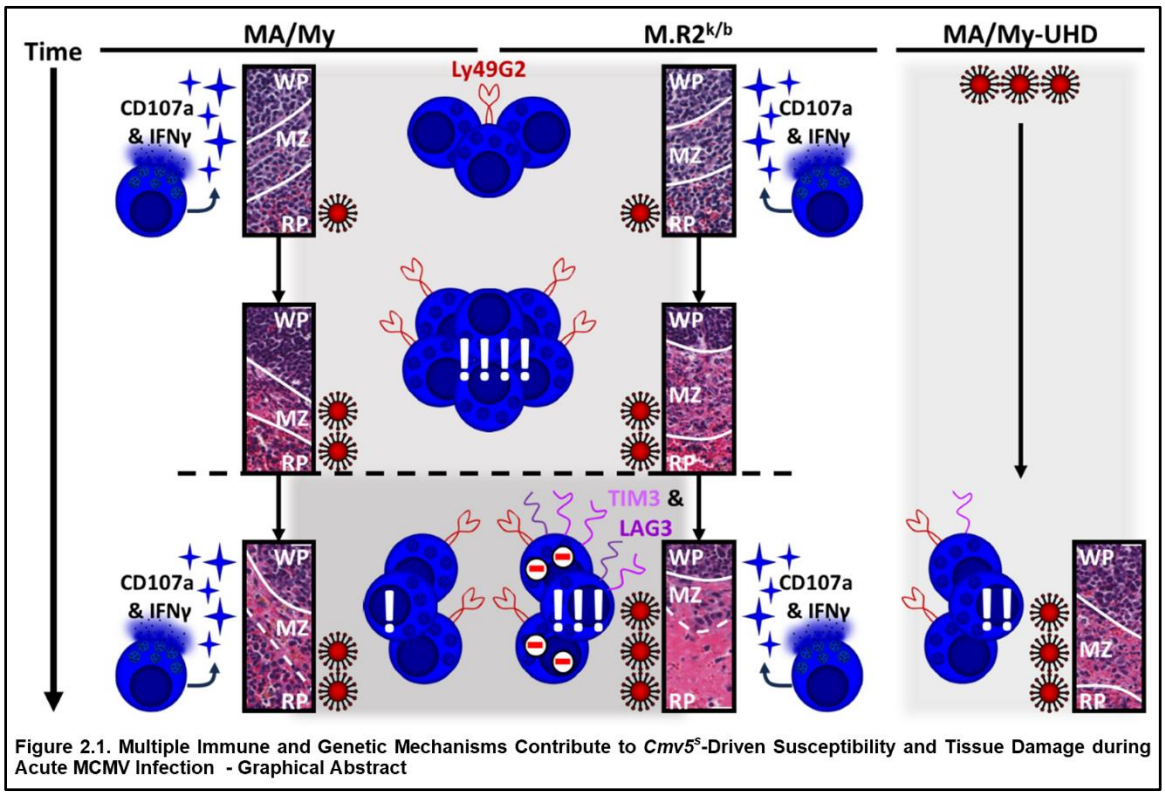

Figure 2.1. Multiple Immune and Genetic Mechanisms Contribute to *Cmv5*^{s}-Driven Susceptibility and Tissue Damage during Acute MCMV Infection - Graphical Abstract

Introduction.

Innate immunity to viral infection is a topic of high clinical relevance that is heavily influenced by the genetic makeup of the host, with the ability to predispose individuals to severe outcomes of infection[155]. NK cells are important innate antiviral effector cells that use a balance of activating and inhibitory signals to distinguish healthy from infected or cancerous cells[157], and mount an immune response through direct cytotoxic activity and production of effector cytokines such as IFNγ[72]. Interactions between inhibitory Ly49 receptors on NK cells and host cell MHC-I molecules contribute to NK cell-mediated antiviral immunity, preventing NK cells from mounting an autoimmune response, but also augmenting NK cell function in a process termed NK cell licensing[147, 158-160]. Licensed NK cells are tuned by this interaction to recognize and respond to instances of missing or altered “self” MHC-I expression, seen when cells become infected or cancerous[159, 161].

Murine cytomegalovirus (MCMV) has been used to study genetic regulation of NK cell-mediated immunity, as NK cells are required for acute viral control[140-142], and different inbred mouse strains vary in levels of resistance or susceptibility to the virus[142, 143]. Much of this variability in response is due to the highly polymorphic Major Histocompatibility (MHC) and Natural Killer Cell (NKC) genetic regions[143, 144], encoding MHC class I (MHC-I) molecules and Ly49 receptors, respectively. MA/My and C57L mice have NKC-Ly49 haplotypes that are very similar[109], however MA/My (H-2^k) mice are much more resistant to MCMV infection than C57L (H-2^b) mice[142]. Previous work identified MHC-I molecule H-$2D^k$ in MA/My mice, which interacts with inhibitory Ly49G2 receptor on NK cells to mediate protection against MCMV infection[145-147]. These Ly49G2+ NK cells licensed on H-$2D^k$ show substantial expansion with increased activation and effector function during acute MCMV infection *in vivo* compared to Ly49G2- counterparts[145, 147]. Importantly, this protection mediated by Ly49G2+ NK cells can be transferred to C57L mice with genetic addition of the H-$2D^k$ molecule[146].

The MHC region of the genome itself is over 3-Megabases (Mb) in size and contains more than 150 protein-coding genes, including host MHC-I and MHC class II (MHC-II) molecules[19, 162]. While many diseases are associated with polymorphisms in the MHC region, very few of these diseases can be fully traced to any one gene variant or protein polymorphism[32], suggesting that interactions between MHC-linked genes may be an important yet poorly understood determinant of disease pathology. In line with this idea, we identified a C57L-derived, MHC-linked Quantitative Trait Locus (QTL) that significantly diminishes resistance to MCMV infection and causes substantial splenic tissue damage in MA/My background mice[149, 163] despite the presence of the protective H-$2D^k$-Ly49G2

pair. This QTL-containing genetic interval is referred to as *Cmv5*, whereas the C57L-derived allele that conveys MCMV susceptibility and tissue damage is referred to as *Cmv5*^{s}, initially described at approximately 23-Mb in size[149, 163, 164] (Table II). As mice homozygous for the *Cmv5*^{s} interval do not express H-2D^{k}, to better understand how *Cmv5*^{s} corrupts this otherwise protective H-2D^{k}-driven response, we limited our analysis to *Cmv5* heterozygous mice.

Since the publication of the original *Cmv5*^{s}-bearing M.H2$^{k/b}$ mouse strain, we have substantially narrowed the size of the QTL interval and more rigorously defined the genetic boundaries and interval-associated phenotypes in several new *Cmv5*-recombinant congenic mouse strains. We discovered that at least two immune-modulatory loci within the region contribute to acute MCMV susceptibility and tissue damage in *Cmv5*^{s} mice. Additionally, we have separated the tissue damage phenotype in the spleen from the increased viral load and provide evidence suggesting *Cmv5*^{s} causes the development of an environment not conducive to effective NK cell antiviral immunity rather than causing an inherent defect in the NK cell's ability to function.

Together this work sheds light on complex genetic networks within the MHC region that contribute to variation in susceptibility during acute viral infection via profound effects on the innate immune environment. These results and this model system together offer insight into how polymorphism within the MHC can mask the effects of known resistance factors in heterogeneous populations, and further characterization of these genetic networks serves to enhance not only our understanding of early immunity to viral infections, but also the predictive ability of genetic screening, offering the opportunity for more efficient and effective medical intervention.

Results.

M.R2$^{k/b}$ Mice Bear Cmv5^{s} MCMV Susceptibility and Spleen Tissue Damage. To hone in on the location of *Cmv5*^{s} effectors, we continued backcrossing M.H2$^{k/b}$ congenic mice to MA/My parent strain and screened offspring for *Cmv5*-region recombination events. Using this method, we identified *Cmv5*-recombianant M.R2$^{k/b}$ mice (see methods for *Cmv5*-recombinant nomenclature), which are heterozygous for a 5.58-Mb C57L-derived region surrounding the MHC (Fig. 2.2A). *In vivo* screening for MCMV susceptibility

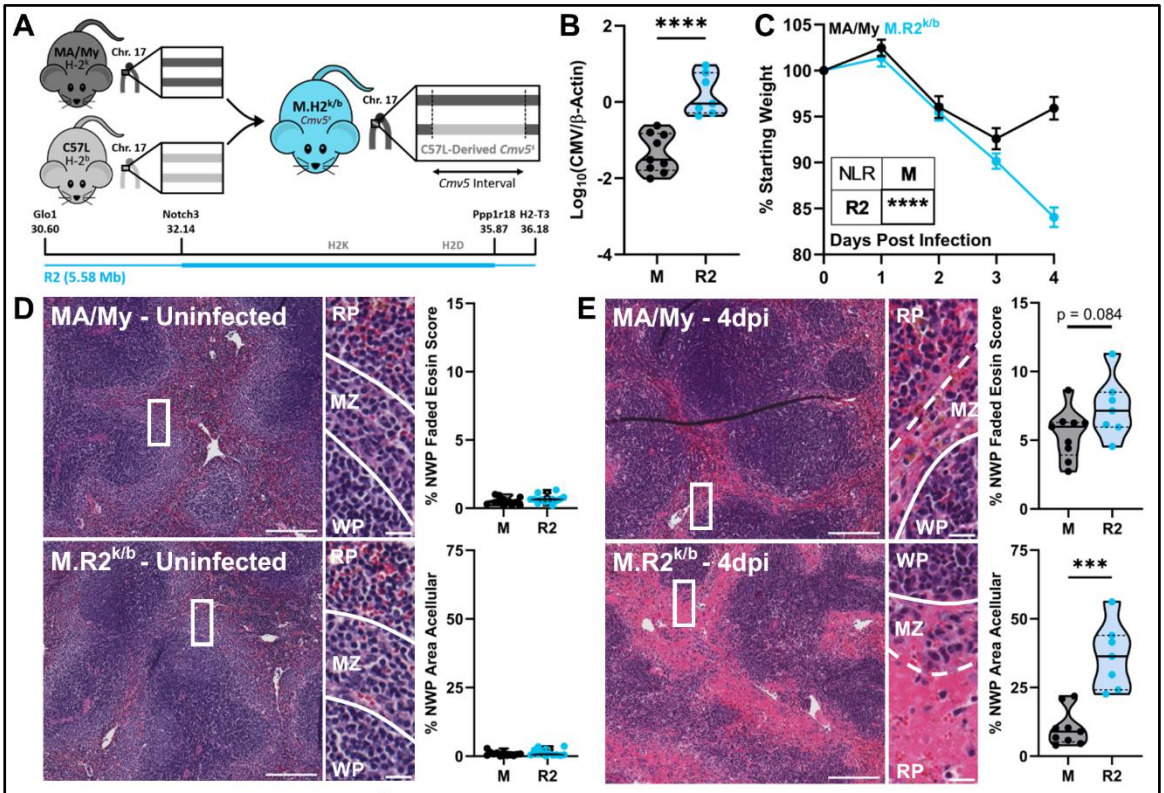

Figure 2.2. M.R2$^{k/b}$ Mice Bear *Cmv5*^{s} MCMV Susceptibility and Spleen Tissue Damage. (A) Schematic depicting the genetic origins of the *Cmv5* recombinant MA/My-congenic mouse with inside and outside border locations for the M.R2$^{k/b}$ (R2) recombinant interval. **(B)** Viral load by quantitative PCR from 4dpi spleen DNA. **(C)** Mouse weight loss during infection as % of starting weight, Error bars represent SEM. Representative images of H&E-stained spleen sections with quantification (NWP = non-white pulp) from uninfected **(D)** or 4dpi **(E)** mice of indicated strains. Zoomed insert contains lines highlighting borders between white pulp (WP)/marginal zone (MZ)/red pulp (RP) regions. Full image scale bar at 200 microns, insert scale bar at 20 microns. **(F)** 4dpi approximate spleen size (area, trapezoid), weight, and cellularity as splenocytes/mg tissue. Violin plots depict median (solid line) and quartile (dashed line) values. **(B, C, E)** pooled from 2 independent experiments with total 7-9 mice per group, **(D)** pooled from 4 independent experiments with total 12-13 mice per group, **(F)** pooled from 2 independent experiments with total 9-10 mice per group. Outliers are omitted when identified by Grubb's outlier test at alpha = 0.05. Statistical comparisons made using unpaired Welch's t-test **(B, D-F)**. Weight loss curves **(C)** are assessed by non-linear (cubic) regression (NLR) with an extra sum of squares F-test (inset table). * p < 0.05, ** p < 0.01, *** p < 0.001, **** p < 0.0001.

identified these M.R2$^{k/b}$ mice as *Cmv5*^{s}, displaying increased viral load (Fig. 2.2B) and

weight loss (Fig. 2.2C) over MA/My counterparts by 4 days post infection (dpi). In addition to the increased weight loss seen at the 4 dpi timepoint, M.R2$^{k/b}$ mice continued to lose weight after 3dpi, while the MA/My mice began to recover (Fig. 2.2C).

M.H2$^{k/b}$ mice were additionally found to display a substantial level of tissue damage in the spleen by 4dpi[163]. While uninfected spleens from *Cmv5*-disparate mice showed clear and cellular white pulp, marginal zone, and red pulp regions (Fig. 2.2D), infected spleens had less cellular marginal zones with abnormal cell morphology and ill-defined boundaries (Fig. 2.2E). In depth assessment of marginal zone histopathology revealed signs of necrosis[165] in both strains, including loss of cellular definition, nuclear swelling, and pale cytoplasmic eosin staining. Additional destruction of the red pulp in M.R2$^{k/b}$ mice was visually apparent by a striking loss of cellularity compared to MA/My (Fig. 2.2E). To better describe splenic damage in *Cmv5*^{s} mice, we quantified the two most apparent aspects of the tissue disruption: marginal zone histopathology consistent with necrosis was quantified by using a faded eosin score (see methods), and red pulp destruction was quantified by acellular area. Using this analysis, we found no evidence of histopathology in *Cmv5*-disparate spleens prior to infection (Fig. 2.2D). However, by 4dpi both strains showed significant tissue remodeling, with increased red pulp acellularity evident in the M.R2$^{k/b}$ spleens (Fig. 2.2E). In line with evidence of increased histopathology in the spleen, we found no difference in approximate spleen area or weight, but a measurable loss of cellularity in the M.R2$^{k/b}$ spleens (Fig. 2.2F). We did not see any differences in histology sections of other major organs at this timepoint (Fig. 2.3). Together this data identifies M.R2$^{k/b}$ mice as *Cmv5*^{s}, displaying characteristic MCMV susceptibility and splenic

damage, which is dissected and quantified in terms of marginal zone necrosis and red pulp cell loss.

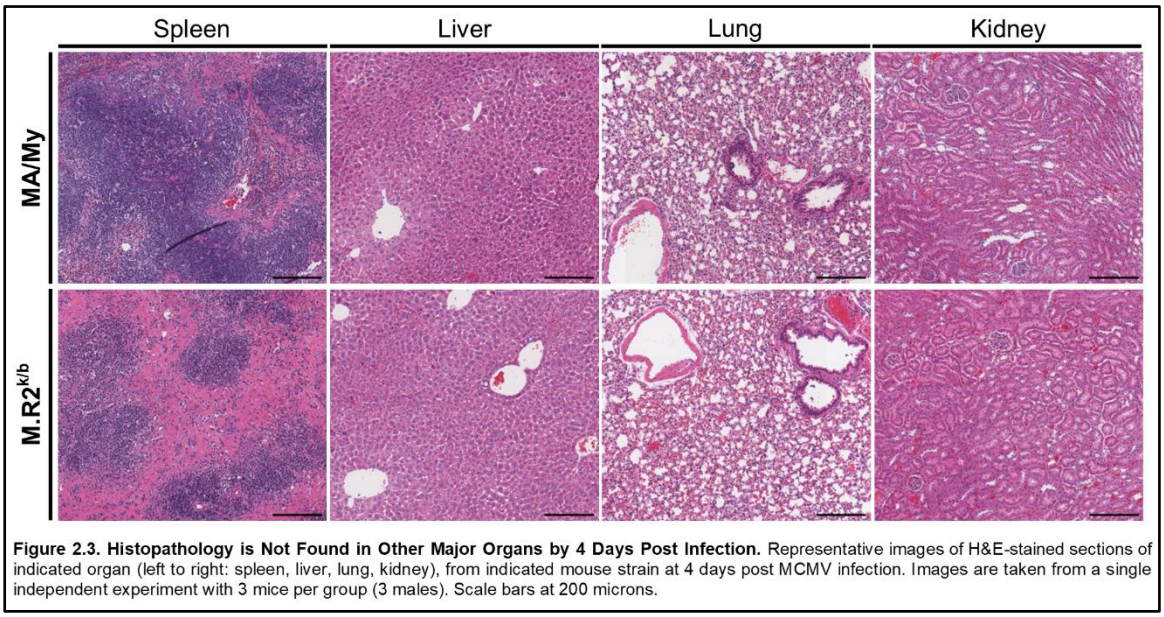

Figure 2.3. Histopathology is Not Found in Other Major Organs by 4 Days Post Infection. Representative images of H&E-stained sections of indicated organ (left to right: spleen, liver, lung, kidney), from indicated mouse strain at 4 days post MCMV infection. Images are taken from a single independent experiment with 3 mice per group (3 males). Scale bars at 200 microns.

Cmv5^{s} NK Cells Upregulate Activation Markers and Checkpoint Receptors at 4 Days Post Infection. As the importance of NK cells in early MCMV control has been established[140-142], we sought to assess NK cell populations in *Cmv5*-disparate spleens at 4dpi. While the percentage of NK cells in the splenocyte population was the same between strains (Fig. 2.4A), the loss of cellularity in M.R2$^{k/b}$ spleens resulted in an overall loss in NK cell numbers (Fig. 2.4B). Interestingly, the remaining NK cells were larger and more granular (Fig. 2.4C), consistent with increased activation[166]. To better assess the state of NK cells, we employed the use of three activation markers: CD25, a component of the high-affinity IL-2 receptor used for NK cell expansion[167]; KLRG1, a maturation marker that is further upregulated in NK cells upon activation during MCMV infection[168, 169]; and Tim-3, an activation-induced checkpoint receptor[102]. We found that at 4dpi, M.R2$^{k/b}$ NK cells

had significantly increased expression of all three markers compared to their MA/My counterparts (Fig. 2.4D), demonstrating an increased state of activation.

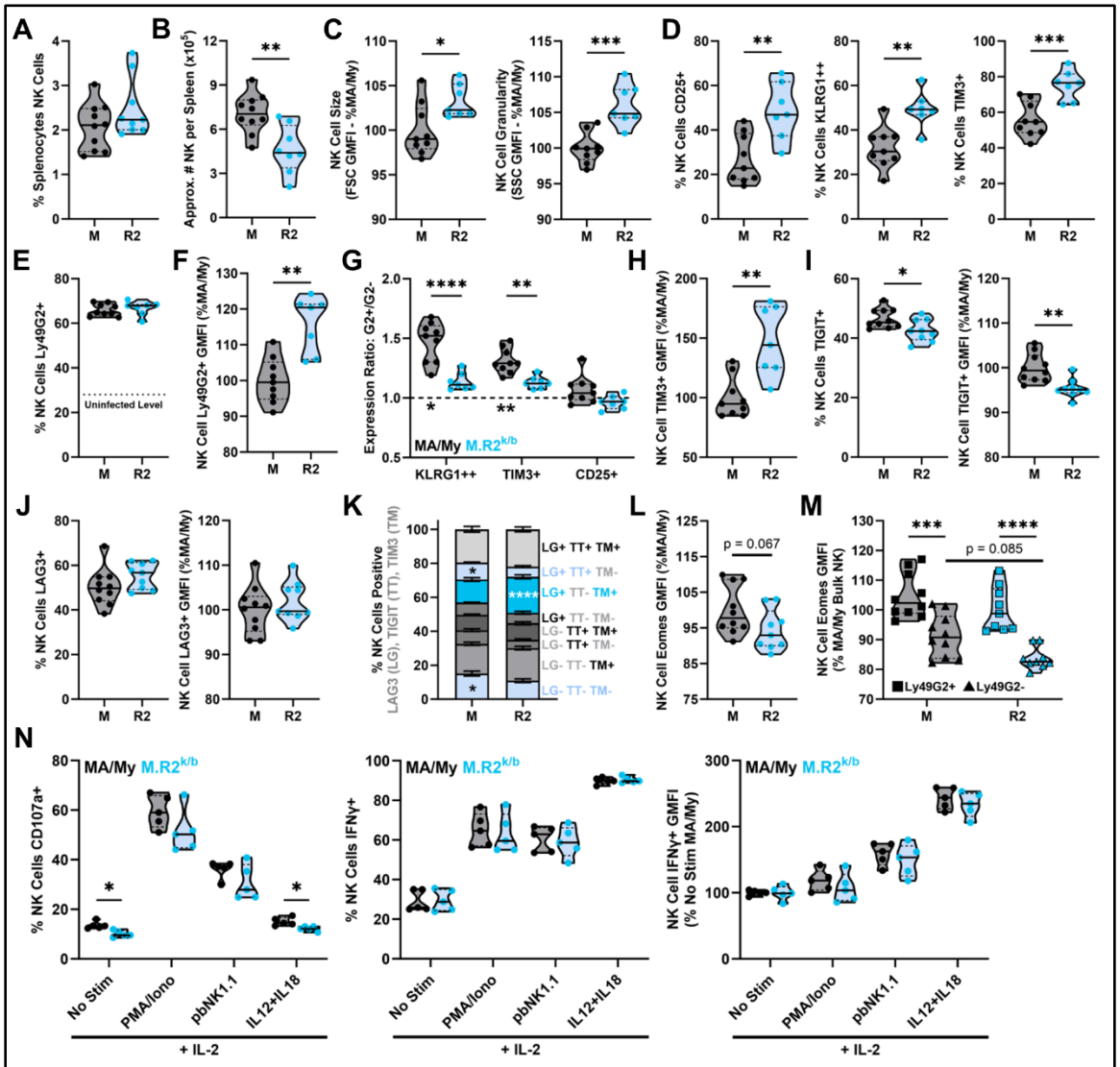

Figure 2.4. *Cmv5*^{s} NK Cells Upregulate Activation Markers and Checkpoint Receptors at 4 Days Post Infection . (A, C-M) Flow cytometry data from splenocytes harvested at 4dpi, pre-gated as described in methods on NK cells or NK cells further segmented by expression of Ly49G2. **(B)** Approximate number of NK cells per spleen was calculated using flow cytometry, cell count, and spleen weight data. **(G)** G2+/G2- expression ratio, top statistics indicate differences in ratios between groups, bottom statistics indicate differences between ratio and y = 1 (statistical differences between G2+ and G2- values). **(K)** Total NK cells divided by their expression of 3 assessed checkpoint molecules: LG = LAG-3, TT = TIGIT, TM = TIM-3. **(N)** NK cells isolated from 4dpi spleens were stimulated *in vitro* and assessed by flow cytometry for CD107a expression (degranulation) and production of IFNγ. Violin plots depict median (solid line) and quartile (dashed line) values. **(A, C-H)** pooled from 2 independent experiments with total 7-9 mice per group. **(B, I-M)** pooled from 2 independent experiments with total 9-10 mice per group. **(N)** representative experiment shown from a total of 2 independent experiments. Outliers omitted if identified by Grubb's outlier test at alpha = 0.05. Statistical comparisons made using unpaired Welch's t-test **(A-F, H-J, L)**, 2-way ANOVAs with Sidak's multiple comparisons test **(G, K, M)**, or multiple unpaired Welch's t-tests with Holm-Sidak corrections for multiple comparisons **(N)**. * p < 0.05, ** p < 0.01, *** p < 0.001, **** p < 0.0001.

H-2D^{k} confers MCMV resistance through licensed Ly49G2+ NK cells, which demonstrate increased proliferation and activation over Ly49G2- NK cells in the same animal[145, 147].

While both MA/My and M.R2$^{k/b}$ mice express H-2D^{k}, M.R2$^{k/b}$ mice are heterozygous, which led us to hypothesize that *Cmv5*^{s} might convey susceptibility to MCMV infection by interfering with the function of Ly49G2+ licensed NK cells. At 4dpi, both strains showed a robust and equivalent expansion of Ly49G2+ NK cells, composing significantly more of the NK cell pool compared to baseline (Fig. 2.4E). Ly49G2+ NK cells from M.R2$^{k/b}$ mice had higher Ly49G2 GMFI compared to MA/My NK cells (Fig. 2.4F), likely due to H-2D^{k} heterozygosity, in line with data for other Ly49/MHC-I pairs[170]. Consistent with what we have seen in other models of H-2D^{k}-driven resistance[147], MA/My mice showed increased expression of activation markers in Ly49G2+ NK cells compared to their Ly49G2- counterparts, showing higher Ly49G2+/Ly49G2- expression ratios for KLRG1^{high} and Tim-3 (Fig. 2.4G). Interestingly, these ratios were significantly diminished in M.R2$^{k/b}$ NK cells (Fig. 2.4G). These data suggest that *Cmv5*^{s} may impede the ability of licensed Ly49G2+ NK cells to become specifically activated over Ly49G2- counterparts, which could prevent them from controlling MCMV infection.

Prior work has shown that Tim-3 is upregulated acutely on activated NK cells, functioning in an inhibitory manner designed to tamper potentially damaging immune activation[102], but build-up of high Tim-3 expression can be associated with dysfunctional NK cells[101]. Not only did M.R2$^{k/b}$ mice have a higher frequency of NK cells expressing Tim-3 (Fig. 2.4D), they also had higher levels of Tim-3 expression (Fig. 2.4H). To better assess if M.R2$^{k/b}$ NK cells may be exhibiting a phenotype consistent with dysfunction *in vivo*, we looked at additional checkpoint receptors, Lag-3 and Tigit[171]. We found that M.R2$^{k/b}$ NK cells showed decreased expression of Tigit (Fig. 2.4I), and comparable expression of Lag-3 to MA/My mice (Fig. 2.4J). Interestingly, M.R2$^{k/b}$ NK cells showed increased co-expression of Tim-3 and Lag-3, as well as an associated decrease in NK cells expressing none of the three

assessed checkpoint markers (Fig. 2.4K). To better understand if these M.R2$^{k/b}$ NK cells may differ functionally, we assessed intracellular expression of Eomesodermin (Eomes), an important transcription factor for NK cell development and function whose downregulation has been associated with dysfunctional NK cells[172, 173]. We found that Eomes expression in M.R2$^{k/b}$ NK cells trended lower than that seen in MA/My NK cells (Fig. 2.4L), and this reduced expression seemed to occur within the Ly49G2- NK cell population (Fig. 2.4M). This data showing increased upregulation of checkpoint receptors and downregulation of Eomes may suggest that M.R2$^{k/b}$ NK cells are dysfunctional[101, 171-173]. To test this, we isolated NK cells from 4dpi spleens and stimulated them *in vitro*. This assay revealed no differences in NK cell degranulation or IFN-γ production under basic stimulatory conditions (Fig. 2.4N). While CD107a values for the no stimulation and IL-12/IL-18 stimulation conditions did technically reach statistical significance, the difference was minute (~3%) and we were unable to verify it in a repeat experiment. M.R2$^{k/b}$ NK cells thus are not inherently dysfunctional at 4dpi, but the upregulation of checkpoint receptors suggests they may be more sensitive to inhibition by the *in vivo* environment.

MA/My and M.R2$^{k/b}$ NK Cells are Similar in Phenotype and Function at Baseline. To determine if M.R2$^{k/b}$ NK cells display any intrinsic differences in phenotype or function when compared to MA/My, we assessed NK cells from uninfected mice. We found no differences in spleen size, weight, or cellularity prior to MCMV infection (Fig. 2.5A, 2.5B), nor were there any differences in the quantity of NK cells, NK cell morphology, or percent of NK cells Ly49G2+ (Fig. 2.5C, 2.5D). Additionally, we saw no appreciable differences between strains in assessed markers of NK cell maturation (Fig. 2.5E). While NK cells from uninfected animals had minimal expression of activation markers and checkpoint receptors, there was a baseline expression of Tim-3 on ~6% of total NK cells (Fig. 2.5F),

which was almost entirely localized to the Ly49G2- NK cell population (Fig. 2.5G). We additionally found that M.R2$^{k/b}$ NK cells may have lower expression of Eomes at baseline, and that expression of Eomes was higher in the Ly49G2+ NK cells (Fig. 2.5H, 2.5I). To test if the reduced expression of Eomes in M.R2$^{k/b}$ NK cells was associated with a reduced ability to exert effector functions, we stimulated NK cells from uninfected mice *in vitro*, finding no differences in degranulation or IFN-γ production between strains (Fig. 2.5J). Overall, these results show only minor differences in NK cell phenotype, and no differences in basic NK cell function between MA/My and M.R2$^{k/b}$ mice at baseline.

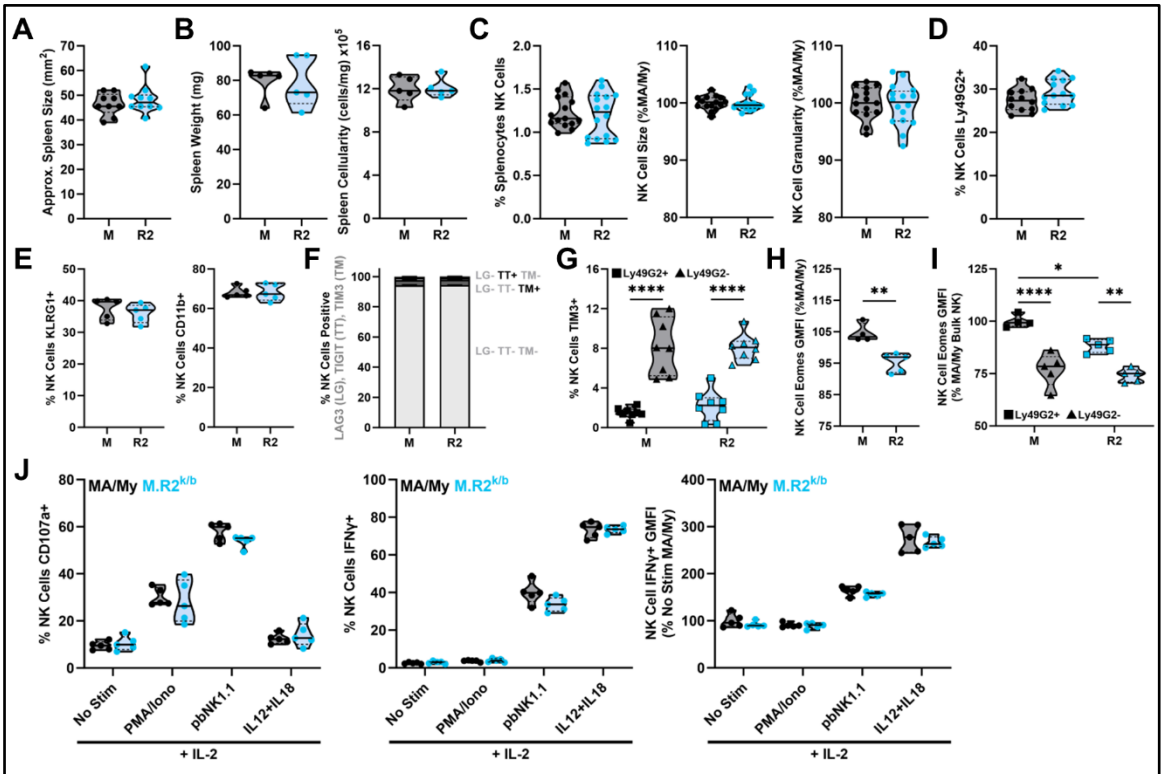

Figure 2.5. MA/My and M.R2$^{k/b}$ NK Cells are Similar in Phenotype and Function at Baseline. (A) Approximate spleen size (area, trapezoid), **(B)** weight and cellularity as splenocytes/mg tissue in uninfected mice of indicated strain. **(C-I)** Flow cytometry data of splenocytes harvested from uninfected mice. **(J)** NK cells isolated from uninfected spleens were stimulated in vitro and assessed by flow cytometry for CD107a expression (degranulation) and production of IFNγ. Violin plots depict median (solid line) and quartile (dashed line) values. **(A)** pooled from 2 independent experiments with total 9-10 mice per group, **(B, E, F, H, I, J)** data from 1 independent experiment with 5 mice per group. **(C)** pooled from 4 independent experiments with total 15-16 mice per group. **(D)** pooled from 3 independent experiments with total 12-13 mice per group. **(G)** pooled from 2 independent experiments with total 8 mice per group. Outliers removed if identified by a Grubb's outlier test at alpha = 0.05. Statistical comparisons are made using an unpaired Welch's t-test **(A-E, H)**, an ordinary 2-way ANOVA with Tukey's (**G, I**) or Sidak's **(F)** multiple comparisons test. **(J)** was assessed by multiple unpaired Welch's t-tests with Holm-Sidak correction for multiple comparisons. * $p < 0.05$, ** $p < 0.01$, *** $p < 0.001$, **** $p < 0.0001$.

Increased Viral Replication is Insufficient to Cause Cmv5^s-like Tissue Damage and NK Cell Activation in MA/My Mice. MCMV enters the spleen at the marginal zone approximately 6-8 hours after systemic infection and progresses rapidly through the red pulp using stromal and myeloid populations as host cells[135, 136, 174]. With this information we hypothesized that a *Cmv5^s*-driven increase in viral load could be responsible for marginal zone and downstream red pulp tissue damage, as well as the increased NK cell activation phenotype. To test this, we increased the viral dose given to the MA/My mice (MA/My - Ultra High Dose (UHD)) to match the 4dpi viral load seen in the M.R2$^{k/b}$ counterparts given the standard dose (Fig. 2.6A). MA/My-UHD mice showed increased weight loss over both standard dose infected MA/My and M.R2$^{k/b}$ mice at 3dpi but did not continue to lose weight after 3dpi like the M.R2$^{k/b}$ animals. Non-linear regression confirmed unique fitted curves for each group (Fig. 2.6B). Thus, even with the increased viral load, MA/My weights began stabilizing by 4dpi. While MA/My-UHD NK cells appeared more activated than their standard dose-infected MA/My counterparts, they did not reach the levels of the M.R2$^{k/b}$ NK cells in morphology (Fig. 2.6C) or any of the assessed surface markers, with the possible exception of KLRG1^{high} (Fig. 2.6D, 2.6E). Here our data suggests that the increased expression of NK cell activation markers CD25 and Tim-3 in M.R2$^{k/b}$ mice is at least in part due to a difference in the infected *Cmv5^s* immune environment. While a slightly smaller population of MA/My-UHD NK cells expressed Ly49G2 in comparison to either strain given the standard dose-infection (Fig. 2.6F), Ly49G2+ NK cells were still selectively activated in the UHD setting (Fig. 2.6G).

Turning to the spleen histology sections, we saw that MA/My-UHD mice displayed increased evidence of marginal zone necrosis over both standard dose-infected groups. However, this did not translate into the substantial cell loss seen at the marginal zone and

throughout the red pulp in the standard dose-infected M.R2$^{k/b}$ spleens (Fig. 2.6H, 2.6I). This data suggests that the necrotic histopathology at the marginal zone may be driven by viral replication or spread, while *Cmv5*^{s}-mediated cell loss occurs via a separate mechanism in the M.R2$^{k/b}$ spleen. Interestingly, necrosis at the marginal zone in MA/My-UHD spleen tissue was associated with inflammatory infiltrates, while the M.R2$^{k/b}$ mice showed a more progressed dissolution of the marginal zone structure. These results demonstrate that the increased viral load and marginal zone necrosis in MA/My-UHD mice is insufficient to drive the dramatic cell loss seen in M.R2$^{k/b}$ spleens.

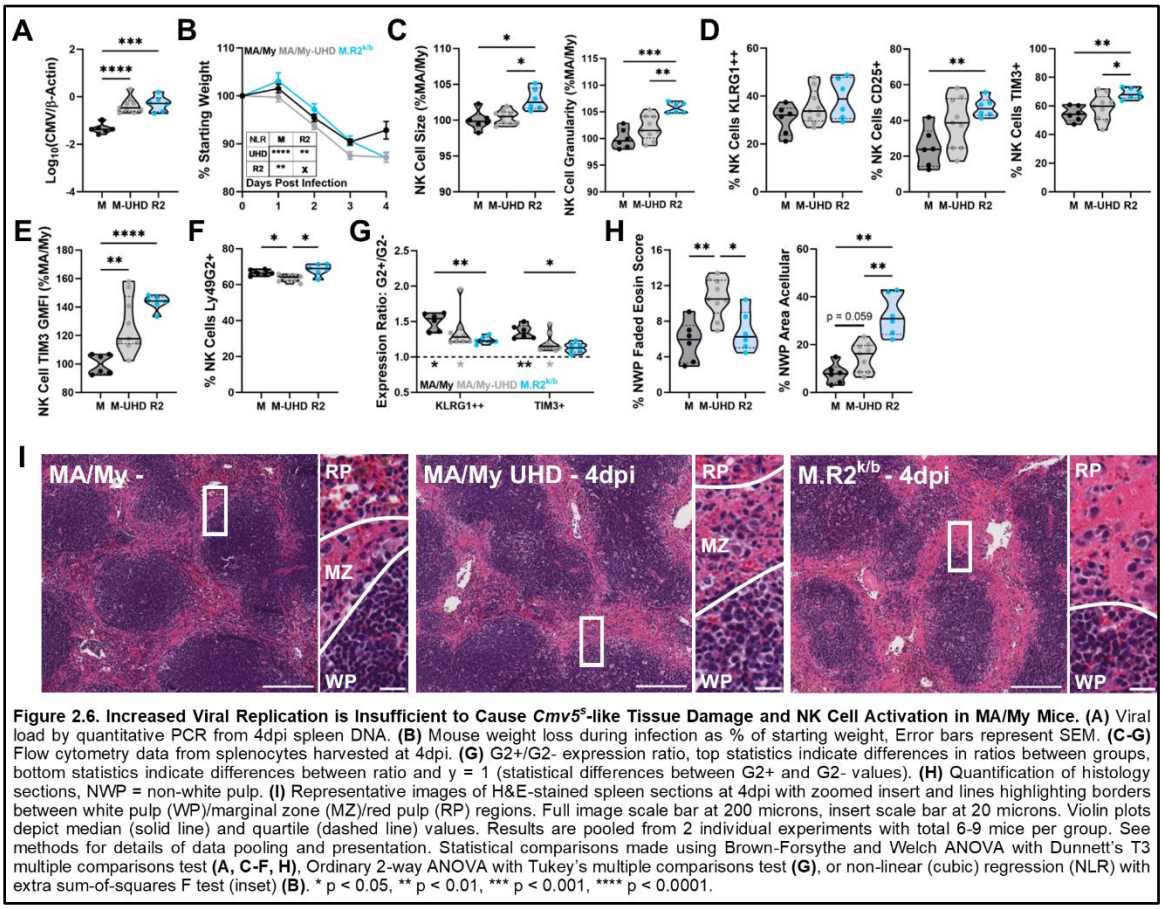

Figure 2.6. Increased Viral Replication is Insufficient to Cause *Cmv5*^{s}-like Tissue Damage and NK Cell Activation in MA/My Mice. (A) Viral load by quantitative PCR from 4dpi spleen DNA. **(B)** Mouse weight loss during infection as % of starting weight, Error bars represent SEM. **(C-G)** Flow cytometry data from splenocytes harvested at 4dpi. **(G)** G2+/G2- expression ratio, top statistics indicate differences in ratios between groups, bottom statistics indicate differences between ratio and y = 1 (statistical differences between G2+ and G2- values). **(H)** Quantification of histology sections, NWP = non-white pulp. **(I)** Representative images of H&E-stained spleen sections at 4dpi with zoomed insert and lines highlighting borders between white pulp (WP)/marginal zone (MZ)/red pulp (RP) regions. Full image scale bar at 200 microns, insert scale bar at 20 microns. Violin plots depict median (solid line) and quartile (dashed line) values. Results are pooled from 2 individual experiments with total 6-9 mice per group. See methods for details of data pooling and presentation. Statistical comparisons made using Brown-Forsythe and Welch ANOVA with Dunnett's T3 multiple comparisons test **(A, C-F, H)**, Ordinary 2-way ANOVA with Tukey's multiple comparisons test **(G)**, or non-linear (cubic) regression (NLR) with extra sum-of-squares F test (inset) **(B)**. * $p < 0.05$, ** $p < 0.01$, *** $p < 0.001$, **** $p < 0.0001$.

Cmv5^s Histopathology at the Marginal Zone Precedes Divergence in Viral Load and NK Cell Phenotype. To better explore the idea of a temporal difference in the response to MCMV between *Cmv5*-disparate mice, and as a way to reveal the phenotypes more likely to be a direct result of the genetic mechanism of action, we assessed *Cmv5^s* phenotypes at 2dpi, just prior to any evidence of divergence in weight loss (Fig. 2.2C). At this timepoint we found no discernable differences in spleen size, cellularity, or viral load between the strains (Fig. 2.7A, 2.7B). While we found a significant loss in the NK cell population from baseline (Fig. 2.7C; compare to Fig. 2.5C), an increase in the proportion of NK cells expressing Ly49G2 (Fig. 2.7D), and evidence of early NK cell activation (Fig. 2.7F, 2.7G); there was no difference between MA/My and M.R2$^{k/b}$ in any of the assessed metrics (Fig. 2.7E-2.7G). While there were no differences between strains, Ly49G2+ NK cells had surpassed Ly49G2- counterparts in expression of Tim-3 (Fig. 2.7H), providing evidence of specific activation. This data suggests that the initial process of NK cell activation and Ly49G2+ population expansion is separate from the differences in NK cell phenotype seen later during infection.

Interestingly, histology sections from 2dpi spleens showed significant disruption at the marginal zone in both strains (Fig. 2.7I, 2.7J), which is consistent with early MCMV entry and replication in marginal zone cells[136]. However, the MA/My marginal zone had seemingly collapsed from its uninfected state, appearing thinner and less organized, while the M.R2$^{k/b}$ marginal zones were bloated and showed significant signs of necrosis, displaying a loss of cellular definition and faded cytoplasmic staining alongside evidence of cellular infiltrates (Fig. 2.7J; compare to Fig. 2.2D). Here we identify marginal zone necrotic histopathology as the first apparent *Cmv5^s* phenotype during MCMV infection, and further assert that differences between *Cmv5*-disparate mice cannot be solely traced

back to increased viral replication. Our data additionally suggest that initial NK cell recognition and activation during MCMV infection are not diminished in *Cmv5*^{s} mice.

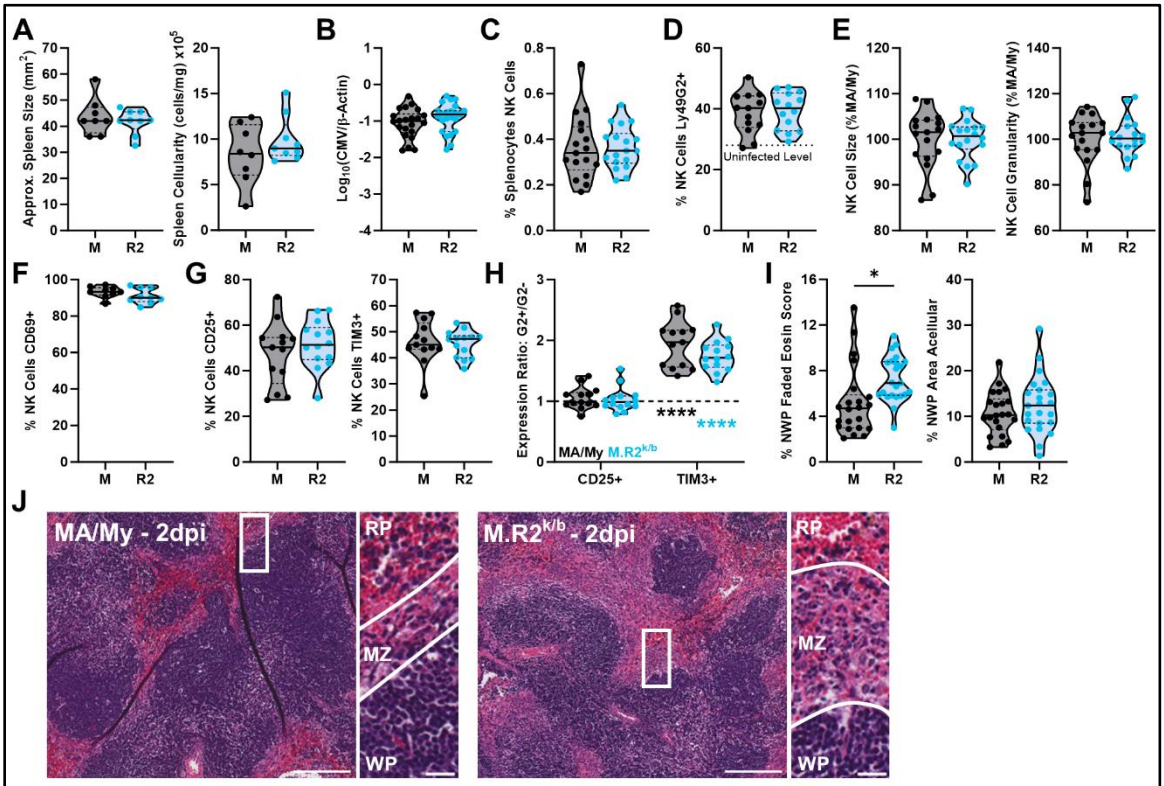

Figure 2.7. *Cmv5*^{s} Histopathology at the Marginal Zone Precedes Divergence in Viral Load and NK Cell Phenotype. (A) Approximate spleen size (area, trapezoid) and cellularity represented as cells/mg spleen. **(B)** Viral load by quantitative PCR from 2dpi spleen DNA **(C-H)** Flow cytometry data from splenocytes harvested at 2dpi. **(H)** G2+/G2- expression ratio, bottom statistics indicate differences between ratio and y = 1 (statistical differences between G2+ and G2- values). **(I)** Quantification of histology sections, NWP = non-white pulp, **(J)** Representative images of H&E-stained spleen sections from different strains at 2dpi with zoomed insert and lines highlighting borders between white pulp (WP)/marginal zone (MZ)/red pulp (RP) regions. Full image scale bar at 200 microns, insert scale bar at 20 microns. Violin plots depict median (solid line) and quartile (dashed line) values. **(A)** Data pooled from 2 independent experiments with total 9-10 mice per group, **(B, I)** pooled from 5 independent experiments with total 22-23 mice per group, **(C, E)** pooled from 4 independent experiments with total 17-18 mice per group, **(F)** pooled from 2 independent experiments with total 9 mice per group, **(D, G, H)** pooled from 3 independent experiments with total 13-14 mice per group. Statistical comparisons made using an unpaired Welch's t-test **(A-G, I)**, or an ordinary 2-way ANOVA with Sidak's multiple comparisons test **(H)**. * $p < 0.05$, ** $p < 0.01$, *** $p < 0.001$, **** $p < 0.0001$.

H2K/Mhc-II Region Cmv5 Recombinants Display Splenic Marginal Zone Damage. In seeking to further narrow the genetic underpinnings of *Cmv5*^{s}-mediated MCMV susceptibility and tissue damage, we generated additional *Cmv5*-recombinant congenic mice: M.R4 $^{k/b}$ (R4), which contain a 3.78Mb C57L-derived region, and M.R5$^{k/b}$ (R5) which contain a 1.44-Mb C57L-derived region. Both M.R5$^{k/b}$ and M.R4$^{k/b}$ intervals encompass the *H2K*/*Mhc-II* region (Fig. 2.8A). While these M.R5$^{k/b}$ and M.R4$^{k/b}$ intervals do not contain

H2D, we continued using heterozygous mice for the sake of consistency. Neither M.R5$^{k/b}$ nor M.R4$^{k/b}$ mice showed increased viral load or weight loss compared to MA/My counterparts (Fig. 2.8B, 2.8C). Additionally, M.R5$^{k/b}$ and M.R4$^{k/b}$ mice showed NK cell morphology and activation marker expression in line with the MA/My group (Fig. 2.8D, 2.8E). Tim-3 expression on the M.R5$^{k/b}$ and M.R4$^{k/b}$ NK cells was higher than MA/My mice, as indicated by the Tim-3 GMFI (Fig. 2.8F), however it did not reach the level of expression seen in the M.R2$^{k/b}$ NK cells. Like MA/My NK cells, M.R5$^{k/b}$ and M.R4$^{k/b}$ NK cells maintained the increased Ly49G2+ activation marker expression ratio (Fig. 2.8G). Interestingly, histopathology in the spleen was apparent, showing evidence of necrosis and acellularity, however this damage was highly localized to the marginal zone area without apparent spread into the red pulp (Fig. 2.8H, 2.8I). While quantification of histology sections identified higher acellular area in M.R5$^{k/b}$ and M.R4$^{k/b}$ spleens, confinement to the marginal zone regions significantly reduced the overall area affected when compared to that seen in M.R2$^{k/b}$ mice (Fig. 2.8H). Here we identified a similar partial phenotype in two different *Cmv5*-recombinant strains overlapping the same *H2K*/*Mhc-II* genomic region. Data from these mice suggest that tissue damage at the marginal zone may be separate from the appearance of acellularity in the red pulp and independent of increased viral load. Additionally, the identification of a partial phenotype in the M.R5$^{k/b}$ mice asserts that a locus in this R5 interval, along with at least one other currently unknown locus, contributes to the *Cmv5*^{s} MCMV susceptibility and tissue damage phenotype seen in the M.R2$^{k/b}$ mice.

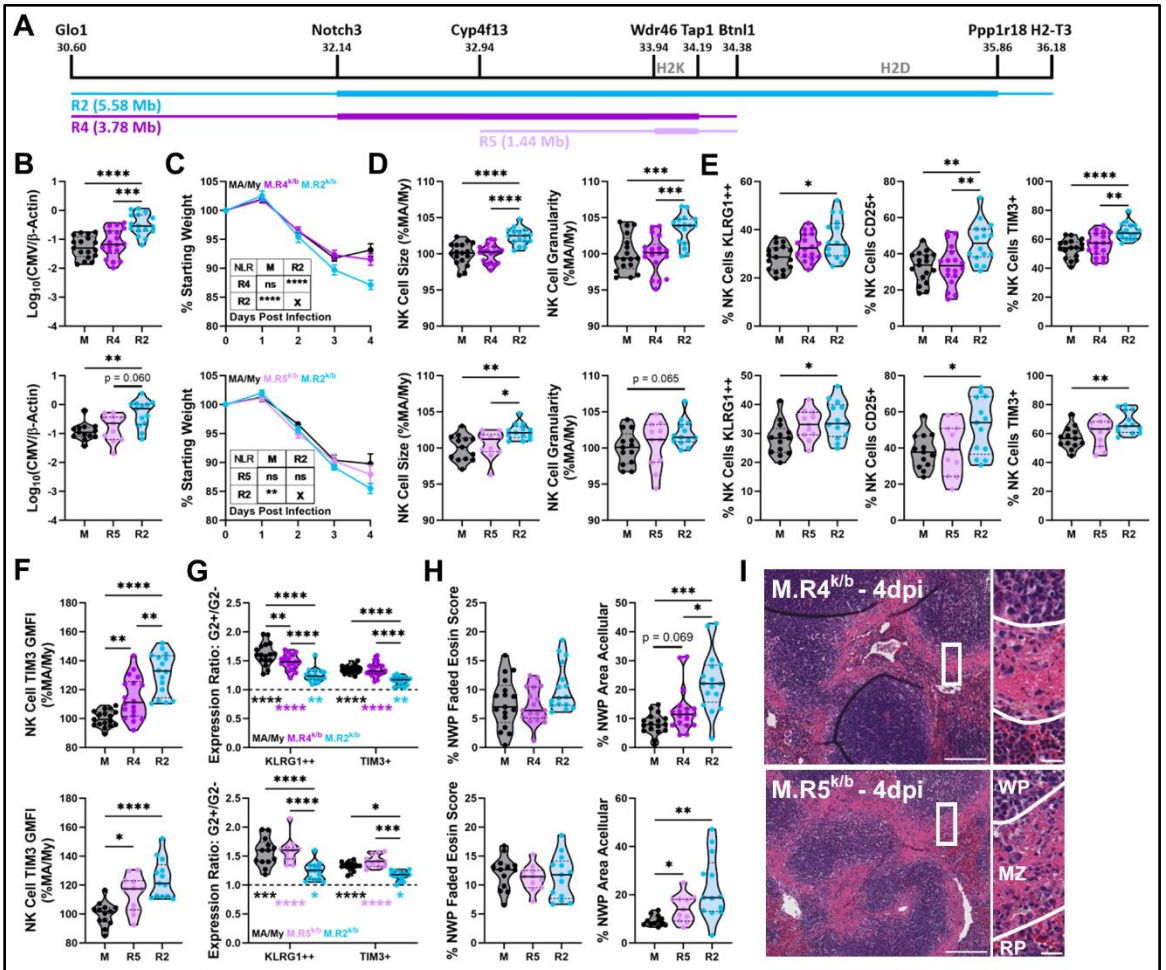

Figure 2.8. *H2K/MHC-II* Region *Cmv5* Recombinants Display Splenic Marginal Zone Damage without MCMV Susceptibility. (A) Schematic depicting the M.R4$^{k/b}$ (R4) and M.R5$^{k/b}$ (R5) C57L-derived interval locations. **(B)** Viral load by quantitative PCR from 4dpi spleen DNA. **(C)** Mouse weight loss during infection as % of starting weight, Error bars represent SEM. NLR = non-linear regression. **(D-G)** Flow cytometry data from splenocytes harvested at 4dpi. **(G)** G2+/G2- expression ratio, top statistics indicate differences in ratios between groups, bottom statistics indicate differences between ratio and y = 1 (statistical differences between G2+ and G2- values). **(H)** Quantification of histology sections, NWP = non-white pulp. **(I)** Representative image of H&E-stained spleen sections at 4dpi with zoomed insert and lines highlighting borders between white pulp (WP)/marginal zone (MZ)/red pulp (RP) regions. Full image scale bar at 200 microns, insert scale bar at 20 microns. Violin plots depict median (solid line) and quartile (dashed line) values. Data pooled from R4 - 5 independent experiments with total 16-18 mice per group, or R5 - 3 independent experiments with total 11-13 mice per group. See methods for details of data pooling and presentation. Outliers omitted if identified by Grubb's outlier test at p = 0.05. Statistical comparisons are made using Brown-Forsythe and Welch ANOVA with Dunnett's T3 multiple comparisons test **(B, D-F, H)**, ordinary 2-way ANOVA with Tukey's multiple comparisons test **(G)**, or non-linear (cubic) regression (NLR) with extra sum-of-squares F test (inset) **(C)**. * p < 0.05, ** p < 0.01, *** p < 0.001, **** p < 0.0001.

C57L-Derived H2D Locus is Insufficient to Convey MCMV Susceptibility or Tissue Damage. We additionally generated two *Cmv5*-recombinant strains encompassing the *H2D* locus: M.R6$^{k/b}$ (R6) mice, which bear a 1.11Mb C57L-derived interval; and M.R8$^{k/b}$ (R8) mice, which bear a 3.82 Mb interval encompassing *H2D* and the *H2K*/*Mhc-II* regions (Fig. 2.9A). Considering the importance of H-2D^{k} as a resistance factor for MCMV in this model, we were surprised to find no difference between MA/My and M.R6$^{k/b}$ viral loads.

However, higher viral loads in M.R8$^{k/b}$ mice were on par with M.R2$^{k/b}$ mice (Fig. 2.9B). Similar to the pattern seen in the MA/My-UHD mice (Fig. 4B), the M.R6$^{k/b}$ mice lost more weight than the MA/My mice but began to stabilize between 3-4dpi while both the M.R2$^{k/b}$ and M.R8$^{k/b}$ mice continued to lose weight (Fig. 2.9C). Non-linear regression analysis identified three unique weight loss curves from the four strains: a shared curve for both M.R2$^{k/b}$ and M.R8$^{k/b}$ mice, and distinct curves for both MA/My and M.R6$^{k/b}$ mice. Both M.R6$^{k/b}$ and M.R8$^{k/b}$ mice displayed increased NK cell size and KLRG1-high expression, while only M.R8$^{k/b}$ matched the M.R2$^{k/b}$ NK cell granularity and expression of CD25 and Tim-3 (Fig. 2.9D-2.9G). Interestingly, all the *Cmv5*-recombinant mice heterozygous at *H2D* showed a reduction in selective activation of Ly49G2+ NK cells (Fig. 2.9H) and increased Ly49G2 GMFI (Fig 2.9I), suggesting these features are unlikely to be causative in *Cmv5*^{s} reduced MCMV control.

In line with M.R8$^{k/b}$ mice displaying a full *Cmv5*^{s} phenotype on par with the M.R2$^{k/b}$ mice, M.R8$^{k/b}$ spleens showed significant spleen histopathology marked by a loss of organized marginal zone, evidence of marginal zone necrosis, and widespread acellularity (Fig. 2.9J, 2.9K). The identification of M.R8$^{k/b}$ mice as bearing *Cmv5*^{s} reduces the phenotype-associated genetic interval from ~23-Mb to 3.82-Mb. Additionally, the minimal phenotype in M.R6$^{k/b}$ mice excludes the *H2D* locus as being solely responsible for *Cmv5*^{s} MCMV susceptibility and tissue damage.

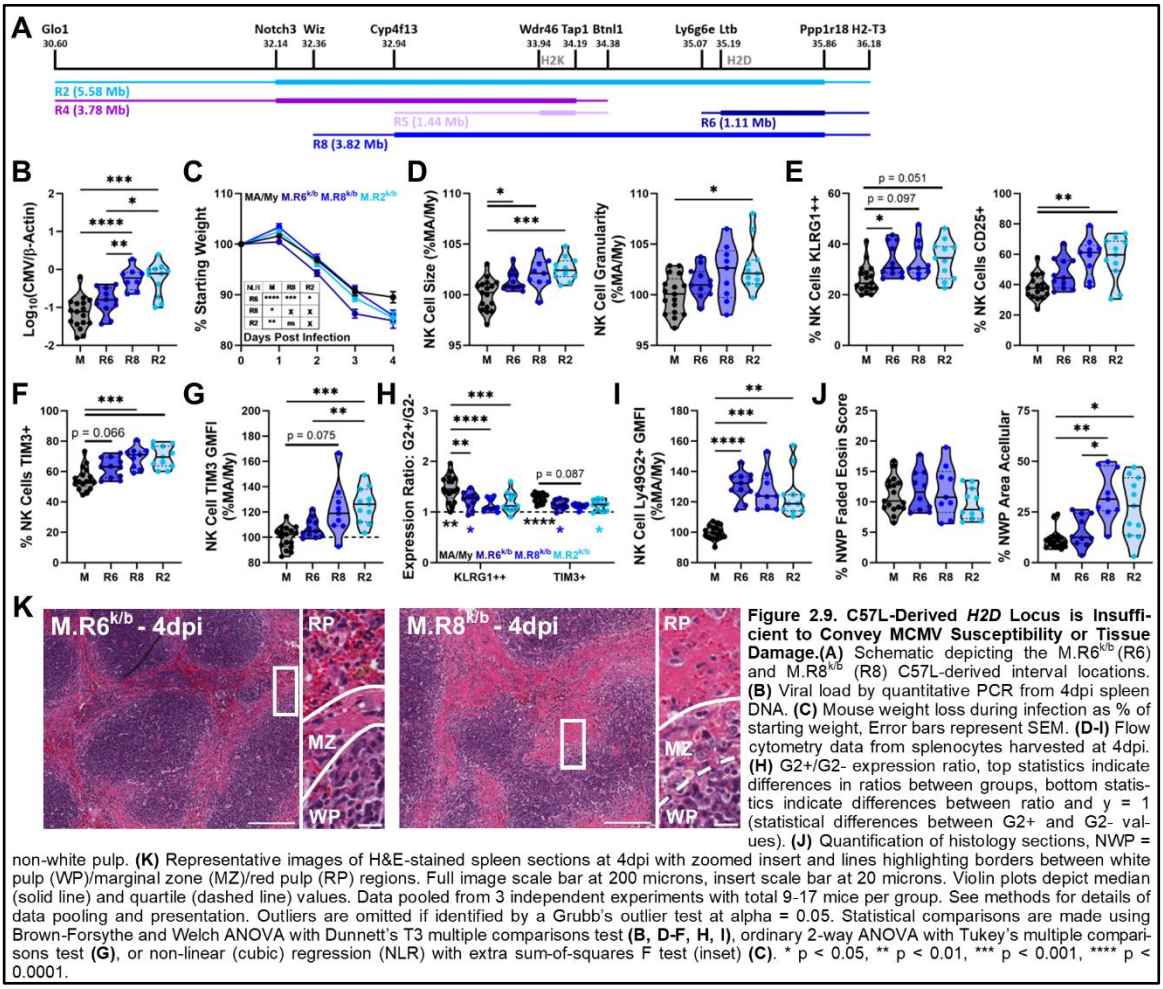

Figure 2.9. C57L-Derived *H2D* Locus is Insufficient to Convey MCMV Susceptibility or Tissue Damage.(A) Schematic depicting the M.R6$^{k/b}$ (R6) and M.R8$^{k/b}$ (R8) C57L-derived interval locations. **(B)** Viral load by quantitative PCR from 4dpi spleen DNA. **(C)** Mouse weight loss during infection as % of starting weight, Error bars represent SEM. **(D-I)** Flow cytometry data from splenocytes harvested at 4dpi. **(H)** G2+/G2- expression ratio, top statistics indicate differences in ratios between groups, bottom statistics indicate differences between ratio and y = 1 (statistical differences between G2+ and G2- values). **(J)** Quantification of histology sections, NWP = non-white pulp. **(K)** Representative images of H&E-stained spleen sections at 4dpi with zoomed insert and lines highlighting borders between white pulp (WP)/marginal zone (MZ)/red pulp (RP) regions. Full image scale bar at 200 microns, insert scale bar at 20 microns. Violin plots depict median (solid line) and quartile (dashed line) values. Data pooled from 3 independent experiments with total 9-17 mice per group. See methods for details of data pooling and presentation. Outliers are omitted if identified by a Grubb's outlier test at alpha = 0.05. Statistical comparisons are made using Brown-Forsythe and Welch ANOVA with Dunnett's T3 multiple comparisons test **(B, D-F, H, I)**, ordinary 2-way ANOVA with Tukey's multiple comparisons test **(G)**, or non-linear (cubic) regression (NLR) with extra sum-of-squares F test (inset) **(C)**. * $p < 0.05$, ** $p < 0.01$, *** $p < 0.001$, **** $p < 0.0001$.

Discussion.

Genetic mechanisms surrounding morbidity and mortality during acute viral infection are largely unknown, with current information unable to account for most of the variability in outcome among patients[32, 155]. In seeking to better understand the relationship between genetics and viral control, our lab previously identified MHC-linked *Cmv5*^{s}, which conveys susceptibility to acute MCMV infection and severe splenic tissue damage despite a protective MHC-I/Ly49 pair and the presence of effector NK cells[149, 163].

When initially described, the *Cmv5* QTL interval spanned more than 23-Mb, including the entire MHC region and over 400 genes[149] (Table II). In this work, we expanded our genotyping coverage of the *Cmv5* interval, which allowed the identification and testing of several novel *Cmv5*-recombinant congenic lines. Using these recombinant strains, we defined *Cmv5*^{s} traits starting with necrotic pathology at the marginal zone, loss of cellularity throughout the red pulp, and increased NK cell expression of activation and checkpoint markers at 4dpi. From these definitions we further assessed the temporal and genetic mapping of *Cmv5*^{s}. We identified marginal zone destruction as the first apparent *Cmv5*^{s} phenotype at 2dpi and linked its appearance to the R5 genetic interval. Interestingly, R5 spleen marginal zone necrosis was separated from the loss of red pulp cellularity and increased viral susceptibility observed in R2 and R8 mice with regions overlapping R5. Evidence of a partial phenotype controlled by the R5 interval cements the contribution of at least two distinct loci within the MHC region to *Cmv5*^{s} susceptibility and tissue damage during MCMV infection. Analysis of the *H2D*-bearing interval in R6 mice demonstrated that polymorphism of known MCMV resistance locus *H2D* is not sufficient to induce *Cmv5*^{s} pathology. While we cannot rule out the potential that R5 and R6 intervals work together in a synergistic manner to disrupt viral control and tissue tolerance in the red pulp, it is

likely that a non-MHC-I/II locus residing in the region between the R5 and R6 intervals plays a role in recapitulating the R2/R8 *Cmv5*^{s} pathology.

On top of the interactions between loci within the MHC region, *Cmv5*^{s}-driven susceptibility relies on additional interaction with the MA/My background, as it is not pathogenic in MA/MyxC57L F_1 hybrid mice or H-2D^{k} transgenic C57L mice[146, 163]. This contribution of multiple loci within the MHC to antiviral immunity with a consideration for genetic background mirrors previously reported observations in MCMV[143] and other viruses[152, 153]. These reports suggest that further exploration of intra- and extra- MHC interactions is relevant not only to MCMV in MA/My background mice, but in other models of viral pathology in various genetic backgrounds.

Understanding how host genetic makeup influences the progression of tissue damage during acute viral infection is of high clinical significance. MCMV can be found at the spleen marginal zone as early as 6 hours post infection, progressing to widespread prevalence throughout the red pulp by 2dpi[136]. In line with the idea that tissue damage in *Cmv5*^{s} spleens follows the spread of the virus, we see necrotic marginal zone histopathology as the first apparent *Cmv5*^{s} phenotype by 2dpi, and histopathology at the marginal zone is apparent in MA/My mice given an increased viral dose by 4 dpi. Of note, M.R4$^{k/b}$/ M.R5$^{k/b}$ mice show significant marginal zone pathology without an associated increase in viral load. However, there are several differences between M.R4$^{k/b}$/ M.R5$^{k/b}$ splenic pathology compared to that seen in MA/My-UHD mice. Most apparent were the cellular infiltrates and high faded eosin score in the MA/My-UHD mice that was not observed in the M.R4$^{k/b}$/ M.R5$^{k/b}$ spleens. Instead, M.R4$^{k/b}$/ M.R5$^{k/b}$ marginal zone damage consisted of strikingly localized acellularity. The marginal zones of 2dpi M.R2$^{k/b}$ spleens

more closely mirrored the MA/My-UHD pathology, but like the M.R4$^{k/b}$/ M.R5$^{k/b}$ spleens, it was not associated with increased viral load. Additionally, marginal zone disruption in the 2dpi M.R2$^{k/b}$ spleens gave way to widespread red pulp acellularity that was not matched in M.R4$^{k/b}$/ M.R5$^{k/b}$ or MA/My-UHD mice. *Cmv5*^{s} pathology therefore is distinct from that observed in MA/My-UHD; and the genetic separation of phenotype by region further demonstrates *Cmv5*^{s} comprises multiple loci acting together.

In an assessment of *Cmv5* from an immunological standpoint, we provide evidence that the failure of *Cmv5*^{s} NK cells to control MCMV infection is not due to an inherent defect in the ability of the NK cell to become activated and exert effector functions, but rather the establishment of a tissue environment not conducive to effective antiviral NK cell function. Interestingly, our data shows that *Cmv5*^{s} NK cells upregulate non-classical checkpoint receptors Tim-3 and Lag-3 to a greater extent than their MA/My counterparts. In an MCMV infected spleen environment marked by tissue damage starting as early as 2dpi, inhibitory receptors with ligands including Damage-Associated Molecular Patterns (DAMPs) and MHC-II[171] could drastically alter the way *Cmv5*^{s} NK cells respond. Whether this contributes to, or is a symptom of, the inability to control viral infection is unclear and will require further exploration.

While we ruled out the reduced Ly49G2+/Ly49G2- NK cell activation ratio in the M.R2$^{k/b}$ mice as a cause of reduced viral control, we did note interesting stratifications in phenotypes between Ly49G2+ and Ly49G2- NK cells in both strains. In particular, the finding that Ly49G2+ NK cells have higher expression of Eomes than Ly49G2- counterparts may suggest a role for Eomes in Ly49G2-mediated NK cell licensing, in line with previous data associating reduced Eomes in NK cells with reduced ability to kill MHC-

I deficient targets[173]. This is an intriguing finding that may provide additional insight into protective H-2D^k-Ly49G2 NK cell licensing with further study and verification.

Overall, these data explore the immunological and genetic underpinnings of a system where polymorphism in the MHC region and host genetic background promotes the formation of acute viral infection-induced tissue damage and corrupts an otherwise protective antiviral NK cell response. Ongoing work will further delineate the genetic and downstream immunological mechanisms contributing to host susceptibility and tissue damage in this model, advancing our understanding of genetically driven variation in infection outcomes.

Chapter III: Inflammation and Macrophage Loss Mark Susceptibility in a Genetic Model of Acute Viral Infection-Induced Tissue Damage

Abstract.

M.R2$^{k/b}$ mice are identical to MA/My parent strain aside from a 5.58-Mb C57L-derived region on chromosome 17 (*Cmv5*^{s}) that causes increased susceptibility to acute murine CMV (MCMV) infection and the development of significant spleen tissue damage. Spleen pathology begins at the marginal zone (MZ), apparent by 2 days post infection (dpi), and progresses throughout the red pulp by 4 dpi. To better understand how M.R2$^{k/b}$ mice respond to infection and how *Cmv5*^{s} contributes to tissue damage in the spleen, we assessed the regulation of myeloid cells and inflammation during acute (MCMV) infection in MA/My and M.R2$^{k/b}$ mice. We found that *Cmv5*^{s} drove increased neutrophil accumulation, cell death, and oxidative stress at the MZ corresponding with increased spleen IL-6 and TGF-β1 early during infection. Further assessment of MCMV infection dynamics at the early MZ revealed infected SIGNR1+ MZ-localized macrophages (MZMs) as the first apparent cell type lost during infection in these mice, and the likely target of early neutrophil recruitment. Spleen macrophages were also identified as the mediators of differential spleen IL-6 and TGF-β1 in MA/My and M.R2$^{k/b}$ mice. Interrogation of MCMV progression past 2dpi revealed substantial M.R2$^{k/b}$ F480+ red pulp macrophage loss along with buildup of oxidative stress and MZM debris that was not neutrophil-dependent. Together we identify *Cmv5*^{s}-driven macrophage loss and inflammation during acute MCMV infection corresponding with the spatial and temporal development of spleen tissue damage.

Key Points.

Neutrophils swarm *Cmv5*^{s} marginal zones early and die, bringing oxidative stress.

Neutrophil clusters and spreading virus surround highly infected SIGNR1+ MZMs.

Ongoing inflammation in *Cmv5*^{s} spleens marks loss of RPMs and buildup of MZM debris.

Macrophage loss mirrors spatial and temporal appearance of *Cmv5*^{s} tissue damage.

The Work in this Chapter has been Submitted for Publication:

Annis JL, Brown MG. Inflammation and Macrophage Loss Mark Susceptibility in a Genetic Model of Acute Viral Infection-Induced Tissue Damage. 2024.

Graphical Abstract.

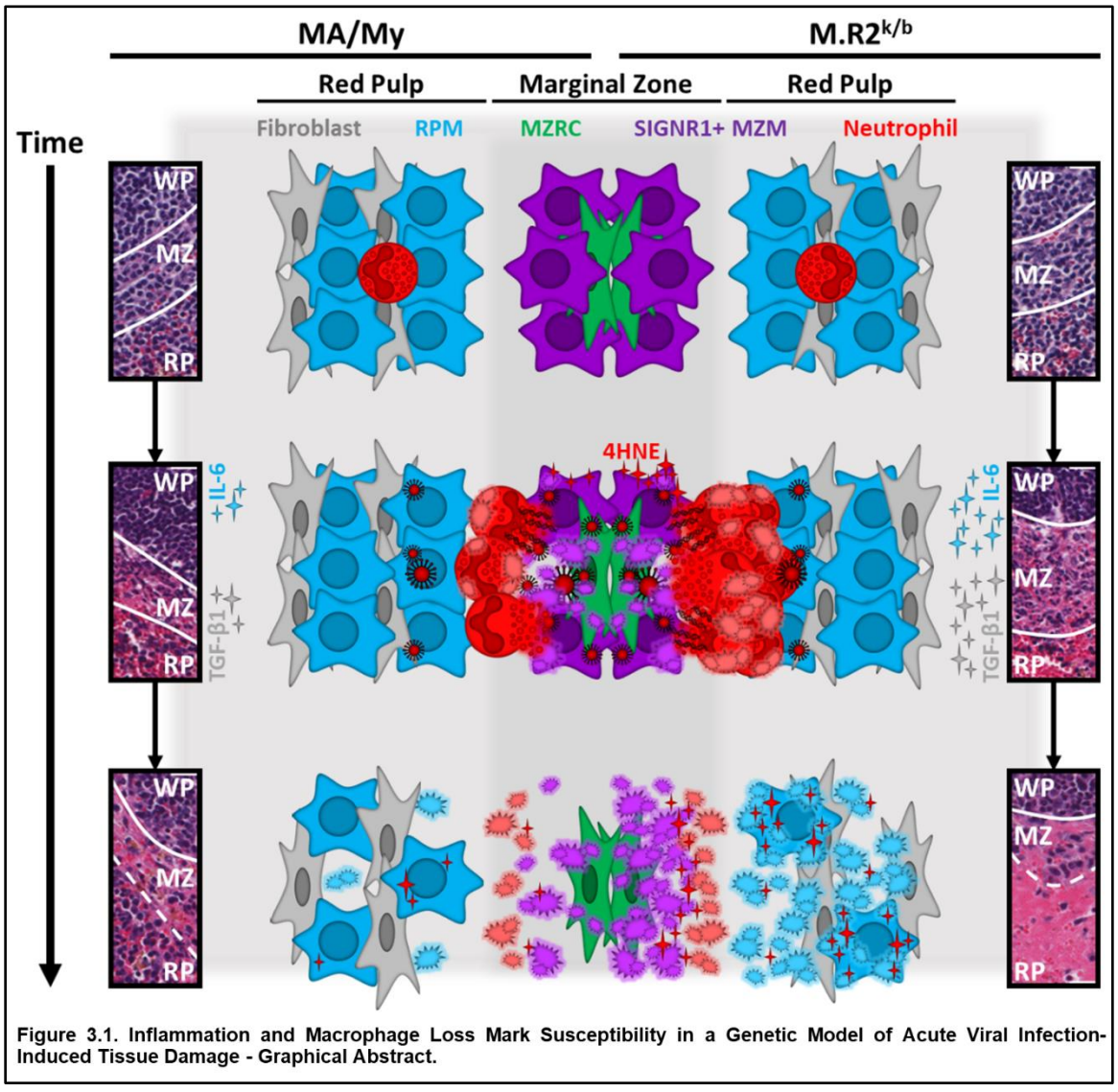

Figure 3.1. Inflammation and Macrophage Loss Mark Susceptibility in a Genetic Model of Acute Viral Infection-Induced Tissue Damage - Graphical Abstract.

Introduction.

It has long been appreciated that host genetic makeup plays an important role in the development of pathology during infections[1], and mutations that prevent appropriate function of many different key immune mediators or pathways are associated with the development of severe disease[2]. In addition to monogenic risk alleles, natural polymorphism between humans are found throughout immune pathways[14], and these variations, despite not necessarily conveying a singular phenotype, can interact with other polymorphisms and pathways that change the progression of the immune response, leading to differences in response to infection based on host genetic makeup. Severe outcomes of viral infections are caused by the accumulation of damage in host tissues that drive cell death and prevent proper function, making host tissue damage the major cause of morbidity and mortality in viral diseases, and highlighting a delicate immunological balance between host defense and self-tolerance during infection. Together, mechanisms of how polymorphism in immune-relevant genes impacts the antiviral immune response and the development of tissue damage are incompletely understood. A better understanding of how host genetic makeup influences the outcomes of viral infection has the potential to aid in the development of more effective medical interventions to prevent and treat severe viral disease.

Inflammation is an important part of the immune response to a pathogen; however, excess or prolonged inflammation can lead to cell death and tissue damage, generally through the accumulation of oxidative stress or the release of directly toxic immune mediators. Oxidative stress occurs when the generation of reactive species (RS) overwhelms a cell's ability to detoxify them, which can lead to cell damage and death[54, 55]. RS are produced

during myeloid cell activation, particularly in macrophages and neutrophils, and are important for killing extracellular and phagocytosed microbes[56, 57]. Toxic mediators such as those found in granulocyte granules or neutrophil extracellular traps, are used to combat pathogen survival in the extracellular space by chelating important cofactors, driving oxidative stress, and breaking down pathogen macromolecules[58-60]. While potently antimicrobial, these factors are generally not explicitly pathogen-targeted, and are associated with host tissue damage during disease[61-66]. Overall, while inflammatory factors are important for host control of viral infections, they are also associated with pathology and severe disease. Genetic predisposition of certain individuals to damaging inflammatory responses have been documented in many viral diseases[8, 67, 68], but often verified mechanisms of action for these risk factors are missing.

The spleen is an important immune organ that relies on different populations of specialized macrophages for optimal function at homeostasis and during infection, and murine cytomegalovirus (MCMV) is a large, dsDNA β-herpesvirus that predominantly infects myeloid, stromal, and parenchymal cells[132], with the ability to spread to various tissues throughout the body via circulating myeloid cells[133, 134]. The spleen is an important early reservoir for MCMV infection, and splenectomized mice display reduced systemic infection and mortality[135]. MCMV enters the spleen hours after infection at the MZ, and spreads into the red pulp starting around 2dpi[136]. While there is evidence that MCMV may infect marginal zone stromal cells early during infection, they do not appear to be the predominant infected cell type for spleen replication and progression[136]. Spleen and liver histopathology have been noted during acute MCMV infection in susceptible mice[137], however the cellular and/or molecular mediators of this phenotype remain mostly uncharacterized. As time progresses, MCMV spreads systemically, infecting cells in most

major organs, where it will establish latency[138, 139]. The importance of the spleen as an early reservoir and the association of MCMV with multiple organs suggests that a better understanding of how spleen pathology develops during early infection has the potential to offer widespread insights into mechanisms of infection-induced tissue damage throughout the body.

M.R2$^{k/b}$ mice are genetically identical to the MA/My parent strain, aside from heterozygosity for a 5.58Mb C57L-derived interval on chromosome 17 (*Cmv5*^{s}), which conveys susceptibility to acute MCMV infection presenting with significant spleen tissue damage[175]. Our prior data identified necrotic histopathology at the early marginal zone as the first apparent *Cmv5*^{s} phenotype, occurring prior to divergence in weight loss, viral load, or effector NK cell activation[175]. This data suggested that *Cmv5*^{s} may drive susceptibility to MCMV infection via the development of tissue damage, but immune processes underlying this acute viral infection-induced histopathology were not explored. In order to better understand the development of tissue damage during early MCMV infection in *Cmv5*^{s}-bearing M.R2$^{k/b}$ mice, we first honed in on the early marginal zone (MZ) damage, finding that early infected MZ macrophage loss leads to an increased infiltration of neutrophils and production of IL-6 and TGF-β1 in M.R2$^{k/b}$ spleens. This macrophage loss and inflammation at the MZ progressed through the red pulp, overall identifying *Cmv5*^{s}-driven inflammation and macrophage loss mirroring the spatial and temporal appearance of spleen tissue damage during acute MCMV infection.

Results.

Increased Neutrophil Accumulation at the M.R2$^{k/b}$ Marginal Zone Early During MCMV infection is Marked by Cell Death and Oxidative Stress. In prior work we identified tissue damage at the spleen MZ as the first apparent phenotype in M.R2$^{k/b}$ mice compared to MA/My parent strain[175]. This histopathology consistent with necrosis is apparent by 2 dpi and presents with accumulation of inflammatory infiltrates (Fig. 3.2A)[175]. To better assess this phenotype, we performed immunofluorescent (IF) imaging of Ly6G+ neutrophils in resistant MA/My and susceptible M.R2$^{k/b}$ strains. At baseline, neutrophils appeared distinctly cellular and spread predominantly throughout the red pulp of the spleen. Quantification of images and cells by flow cytometry revealed no differences in the abundance of neutrophils between strains (Fig. 3.2B). Once infected, neutrophils swarmed the MZ in both strains, with significantly increased accumulation in M.R2$^{k/b}$ spleens (Fig 3.2C). Analysis of splenocytes by flow cytometry mirrored this increase by trend, but did not reach significance (Fig. 3.2C). The lack of significance in the flow data coupled with the presence of large and less distinctly cellular clusters in the M.R2$^{k/b}$ images led us to hypothesize that the neutrophils in the M.R2$^{k/b}$ spleens may be dead or dying. To test this, we performed fluorescent TUNEL analysis with Ly6G co-staining. We found increased TUNEL positivity in the M.R2$^{k/b}$ spleens compared to MA/My, both overall and within the Ly6G+ area (Fig. 3.2D). These data demonstrate a *Cmv5^{s}*-driven increase in neutrophil accumulation and death at the MZ during early MCMV infection.

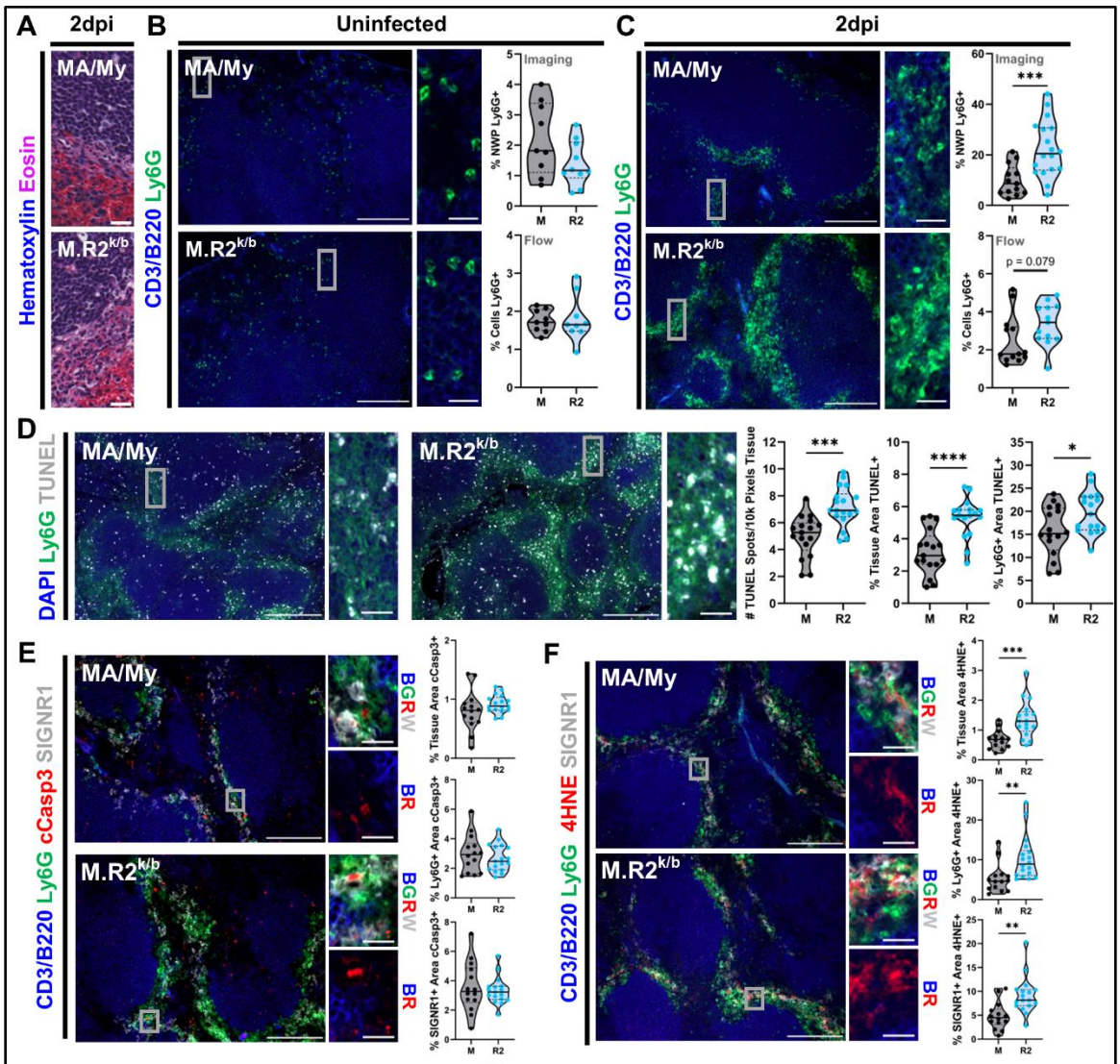

Figure 3.2. Increased Neutrophil Accumulation at the M.R2$^{k/b}$ Marginal Zone Early During MCMV infection is Marked by Cell Death and Oxidative Stress. **(A)** Representative spleen histology sections from indicated genotypes at 2 dpi. Representative images with quantification for **(B)** Uninfected Ly6G+ neutrophils (also includes flow analysis), **(C)** 2 dpi Ly6G+ neutrophils, (also includes flow analysis) **(D)** 2 dpi TUNEL assay with Ly6G+ neutrophils, **(E)** 2 dpi SIGNR1+ MZMs/Ly6G+ neutrophils and cCasp3, **(F)** 2 dpi SIGNR1+ MZMs/Ly6G+ neutrophils and 4HNE. Full image scale bars at 200 microns, insert scale bars at 20 microns. NWP = Non-White Pulp. Violin plots depict median (solid line) and quartile (dashed line) values. Data pooled from: **(B)** 3 independent experiments with total 9-10 mice per group **(C)** Imaging – 4 independent experiments with total 13-18 per group, Flow – 3 independent experiments with total 13 mice per group. **(D)** 4 independent experiments with total 17-18 mice per group. **(E, F)** 4 independent experiments with total 14-18 mice per group. Statistical comparisons made using an unpaired Welch's t-test, outliers are removed if identified by a Grubb's outlier test at alpha = 0.05. * $p < 0.05$, ** $p < 0.01$, *** $p < 0.001$, **** $p < 0.0001$.

Neutrophil death can occur by several different mechanisms with a range of immunological consequences. Neutrophil apoptosis and clearance are important feedback mechanisms designed to reduce inflammation and damage of surrounding tissue[176], while other cell death mechanisms such as pyroptosis and NETosis can exacerbate inflammation and

damage[177]. To ask if the neutrophils may be dying differently between strains, we additionally stained slides for cleaved caspase 3 (cCasp3), an important executioner caspase for apoptosis, alongside Ly6G and SIGNR1 to mark neutrophils and MZMs, respectively. We found no difference between strains in the amount of total cCasp3 staining, or cCasp3 localized within Ly6G+ or SIGNR1+ areas (Fig. 3.2E). The increased cell death by TUNEL coupled with no difference in apoptosis by cCasp3 may suggest that *Cmv5*^{s} drives a more inflammatory cell death pathway that occurs early during MCMV infection at the M.R2$^{k/b}$ MZ. Tissue damage from inflammation generally occurs as the result of increased oxidative stress. As testing for reactive species themselves is not feasible in fixed tissue sections, we measured splenic levels of 4-Hydroxynonenal (4HNE), a stable and toxic byproduct of lipid peroxidation whose buildup is caused by oxidative stress[178]. 4HNE staining was strongly localized to the marginal zone, where it accumulated at the interface between Ly6G+ neutrophils and SIGNR1+ MZMs. In line with our hypothesis, we found significantly increased 4HNE in the M.R2$^{k/b}$ spleens, both by total area positivity and by positivity within the Ly6G and SIGNR1 staining areas (Fig. 3.2F). Together this data shows increased inflammation at the M.R2$^{k/b}$ MZ very early during MCMV infection and coinciding with the appearance of MZ histopathology.

M.R2$^{k/b}$ Spleen Supernatants Have Increased IL-6, TGF-β1, and IFNβ Early after MCMV Infection. To delineate differences in the spleen immunological environment between strains, we ran multiplex ELISAs on 2 dpi spleen supernatants. Overall, there were high levels of antiviral response cytokines IFNγ and IFNβ, as well as classical inflammatory mediators IL-6, TNFα, and IL-1β, but all cytokines assayed were detectable in both strains at this timepoint (Fig. 3.3A). Importantly, we detected significant differences between strains, with M.R2$^{k/b}$ spleens showing increased IFNβ, TGF-β1, and IL-6 over

MA/My counterparts by more than 2-fold (Fig. 3.3B). This data shows differential immune environments between MA/My and M.R2$^{k/b}$ spleens during early MCMV infection, which may contribute to *Cmv5*^{s}-driven tissue damage and loss of viral control.

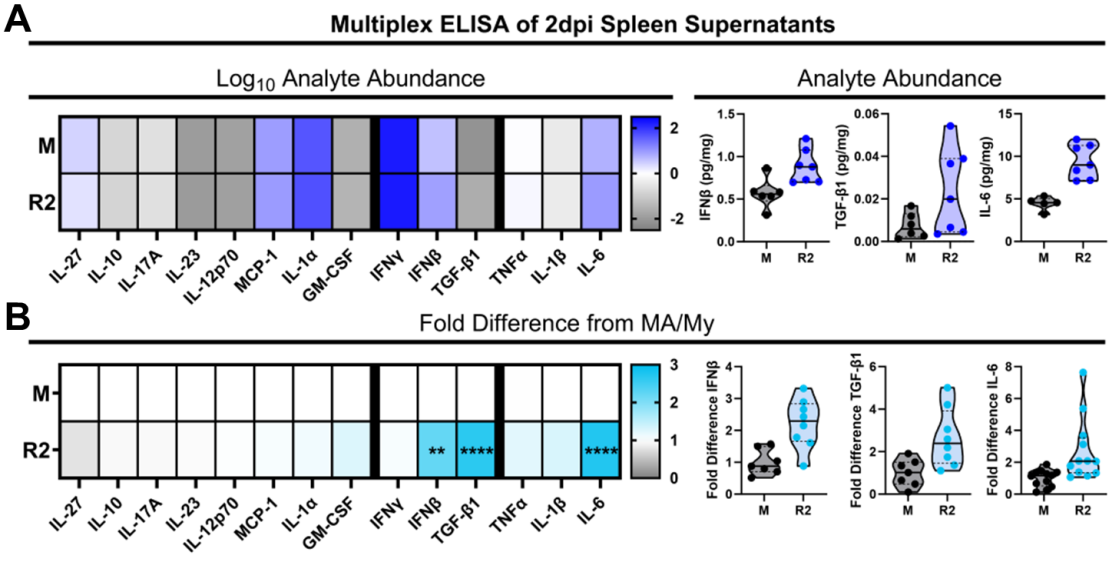

Figure 3.3. M.R2$^{k/b}$ Spleen Supernatants Have Increased IL-6, TGF-β1, and IFNβ Early after MCMV Infection. Multiplex ELISA of 2dpi spleen supernatants. **(A)** Representative log_{10} analyte abundance for all analytes assayed, with raw value violin plots for cytokines of interest. **(B)** Differences between strains presented as fold difference in abundance from MA/My control mean for each experiment. Data was normalized prior to pooling. Heatmaps depict mean values. Violin plots depict median (solid line) and quartile (dashed line) values. Data pooled from: **(A)** 2 independent experiments with total 6-7 mice per group. **(B) Left** (IL-27 to GM-CSF) – 2 independent experiments with total 6-7 mice per group, **Middle** (IFNγ to IFNβ) – 2 independent experiments with total 7-8 mice per group, **Right** (TNFα to IL-6) – 3 independent experiments with total 12 mice per group. Statistical comparisons made using a 2-way ANOVA with Sidak's multiple comparisons test. * $p < 0.05$, ** $p < 0.01$, *** $p < 0.001$, **** $p < 0.0001$.

Neutrophil Depletion Diminishes MZ TUNEL and 4HNE in M.R2$^{k/b}$ Mice Without Affecting Tissue Damage or Inflammation. Prolonged neutrophil swarming with associated cell death and inflammation could contribute to early marginal zone necrotic histopathology seen in the M.R2$^{k/b}$ spleens. To test this, we used a published regimen[179] to stably deplete neutrophils (Fig. 3.4A and see Methods). Depletion of neutrophils was assessed using IF imaging and intracellular staining for Ly6G by flow cytometry[179] (Fig. 3.4B). Evidence of inflammatory infiltrates at the marginal zones of M.R2$^{k/b}$ mice was eliminated with neutrophil depletion. However, necrotic-like histopathology including loss

of cellular definition, nuclear swelling, and pale cytoplasmic eosin staining[165] was still apparent (Fig. 3.4C). This data demonstrates that increased neutrophil accumulation at the M.R2$^{k/b}$ MZ is a symptom rather than the cause of *Cmv5*^{s}-driven MZ histopathology during early MCMV infection.

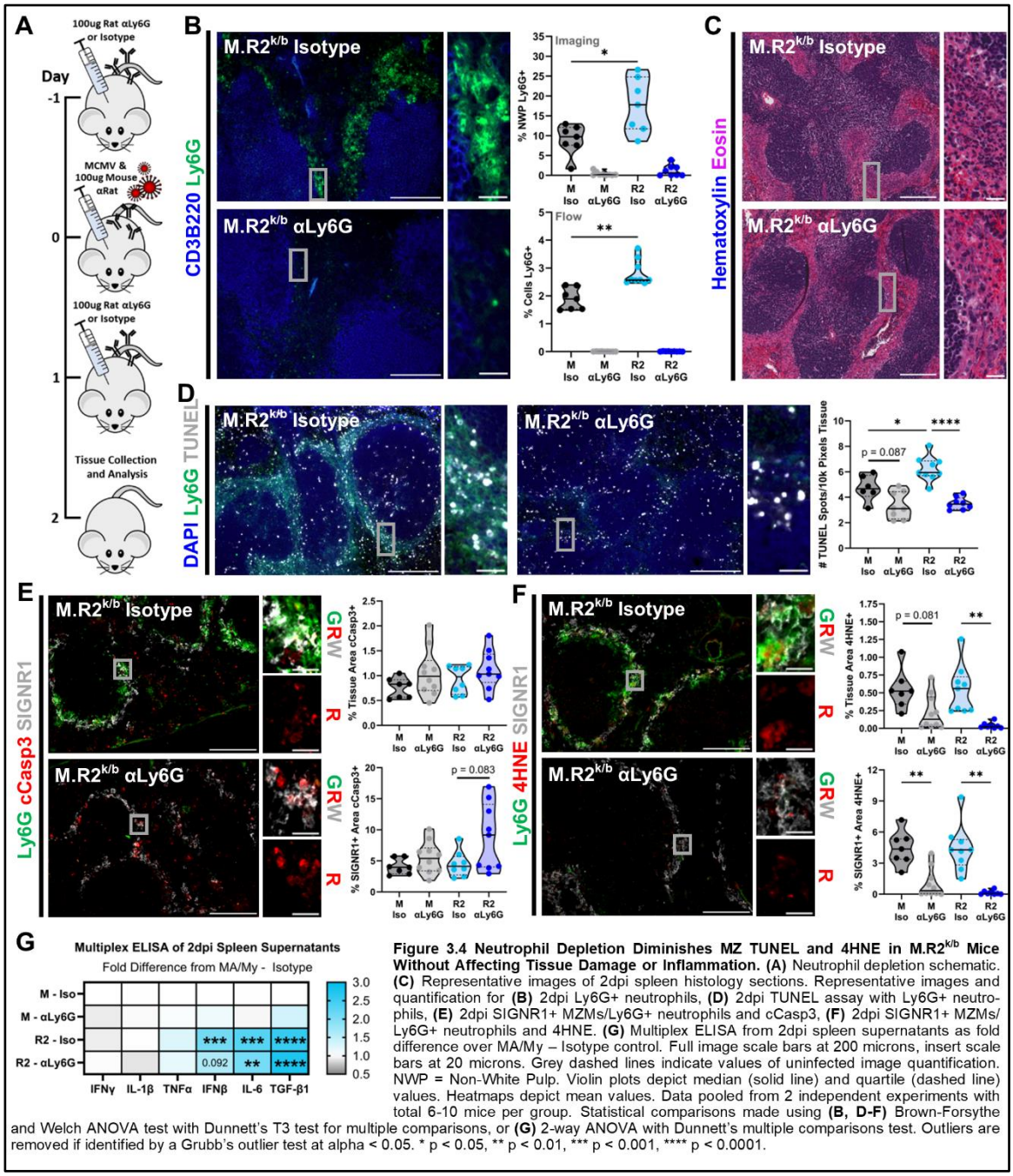

Figure 3.4 Neutrophil Depletion Diminishes MZ TUNEL and 4HNE in M.R2$^{k/b}$ Mice Without Affecting Tissue Damage or Inflammation. **(A)** Neutrophil depletion schematic. **(C)** Representative images of 2dpi spleen histology sections. Representative images and quantification for **(B)** 2dpi Ly6G+ neutrophils, **(D)** 2dpi TUNEL assay with Ly6G+ neutrophils, **(E)** 2dpi SIGNR1+ MZMs/Ly6G+ neutrophils and cCasp3, **(F)** 2dpi SIGNR1+ MZMs/Ly6G+ neutrophils and 4HNE. **(G)** Multiplex ELISA from 2dpi spleen supernatants as fold difference over MA/My – Isotype control. Full image scale bars at 200 microns, insert scale bars at 20 microns. Grey dashed lines indicate values of uninfected image quantification. NWP = Non-White Pulp. Violin plots depict median (solid line) and quartile (dashed line) values. Heatmaps depict mean values. Data pooled from 2 independent experiments with total 6-10 mice per group. Statistical comparisons made using **(B, D-F)** Brown-Forsythe and Welch ANOVA test with Dunnett's T3 test for multiple comparisons, or **(G)** 2-way ANOVA with Dunnett's multiple comparisons test. Outliers are removed if identified by a Grubb's outlier test at alpha < 0.05. * p < 0.05, ** p < 0.01, *** p < 0.001, **** p < 0.0001.

Depletion of neutrophils alleviated the higher TUNEL staining in M.R2$^{k/b}$ spleens over MA/My counterparts, although there was still cell death in the neutrophil depleted spleens, found predominantly at the MZ and in the red pulp (Fig. 3.4D). Interestingly, neutrophil depletion did not reduce spleen cCasp3, and may even result in higher cCasp3 staining on SIGNR1+ MZMs in the M.R2$^{k/b}$ spleens (Fig. 3.4E). In line with the idea that neutrophils were swarming the MZ and dying in an immunogenic manner, their depletion essentially eliminated the MZ buildup of 4HNE (Fig. 3.4F). To determine if neutrophils were responsible for the increased IL-6, TGF-β1, and IFNβ found in bulk spleen supernatants, we assessed changes in these cytokines in the neutrophil depleted mice. While neutrophil depletion had no effect on any of the assessed cytokines in MA/My mice, it eliminated the significant increase in IFNβ seen in the M.R2$^{k/b}$ spleens over MA/My counterparts (Fig. 3G). These data demonstrate that neutrophil accumulation is required for increased cell death and MZ buildup of oxidative stress, but not for *Cmv5*^{s}-mediated early MZ tissue damage or increased spleen IL-6 and TGF-β1.

Infection of Macrophages Coincides with MZ Neutrophil Recruitment and Spleen IL-6 Production During Early MCMV Infection. Having excluded neutrophils as the cause of MZ necrotic histopathology in M.R2$^{k/b}$ spleens, we next asked about other MZ-localized cells at 2dpi. Since 4HNE co-localized at the interface between neutrophils and SIGNR1+ MZMs, we investigated the state of MZ-localized macrophage populations (MZMs). CD169+ and SIGNR1+ MZMs line the MZ and surveil incoming blood for apoptotic cells and potential pathogens[130]. As expected in uninfected mice, a thick border of MZMs around the white pulp with spread-out, surveilling morphology was observed (Fig. 3.5A). After infection, there was a significant loss of both MZM populations in both strains, and

remaining cells appeared morphologically more ameboid and compact (Fig. 3.5B). There was no apparent loss or morphological changes seen in MAdCAM1+ MZ reticular cells (MZRCs) at the same timepoint (Fig. 3.5C, 3.5D).

MCMV has been shown to enter the spleen at the MZ around 6 hpi before spreading into the red pulp by around 2 dpi[136]. We next asked if MCMV localization and replication differed between strains during early MCMV infection, and whether we could better discern the mechanisms of MZM cell loss and neutrophil accumulation at an earlier timepoint. We infected MA/My and M.R2$^{k/b}$ mice with MCMV-GFP[180] and assessed infection at 36 hpi. We observed significant MZ-localization of MCMV-GFP at this timepoint, but no difference in the amount of positive area or intensity of staining between strains (Fig. 3.5E). Assessment of MZM populations revealed decreases in both populations from baseline levels, however loss was more pronounced in the SIGNR1+ MZMs, which had already reached the level seen at 2 dpi (Fig. 3.5F).

To determine if the loss of SIGNR1+ MZMs may be associated with MCMV at the marginal zone, we assessed co-localization of MCMV and SIGNR1. We found that 88% of MCMV-GFP+ area colocalized with SIGNR1+ MZMs, with 53% of SIGNR1+ area affected (Fig. 3.5G, Region 1). These data suggest that SIGNR1+ MZMs are a major splenic target of MCMV, which aligns with their loss during early infection. We hypothesized that the death of infected SIGNR1+ MZMs may be responsible for the early infiltration of neutrophils to the MZ. When we assessed MCMV-GFP MFI alongside proximity to Ly6G+ neutrophil clusters (cLy6G) we found higher MCMV-GFP staining was visually apparent in the MZMs directly next to neutrophil clusters (near cLy6G) (Fig. 3.5G, Region 2, Top), compared with MZMs located anywhere else in the spleen (far cLy6G) (Figure 3.5G, Region 2, Bottom).

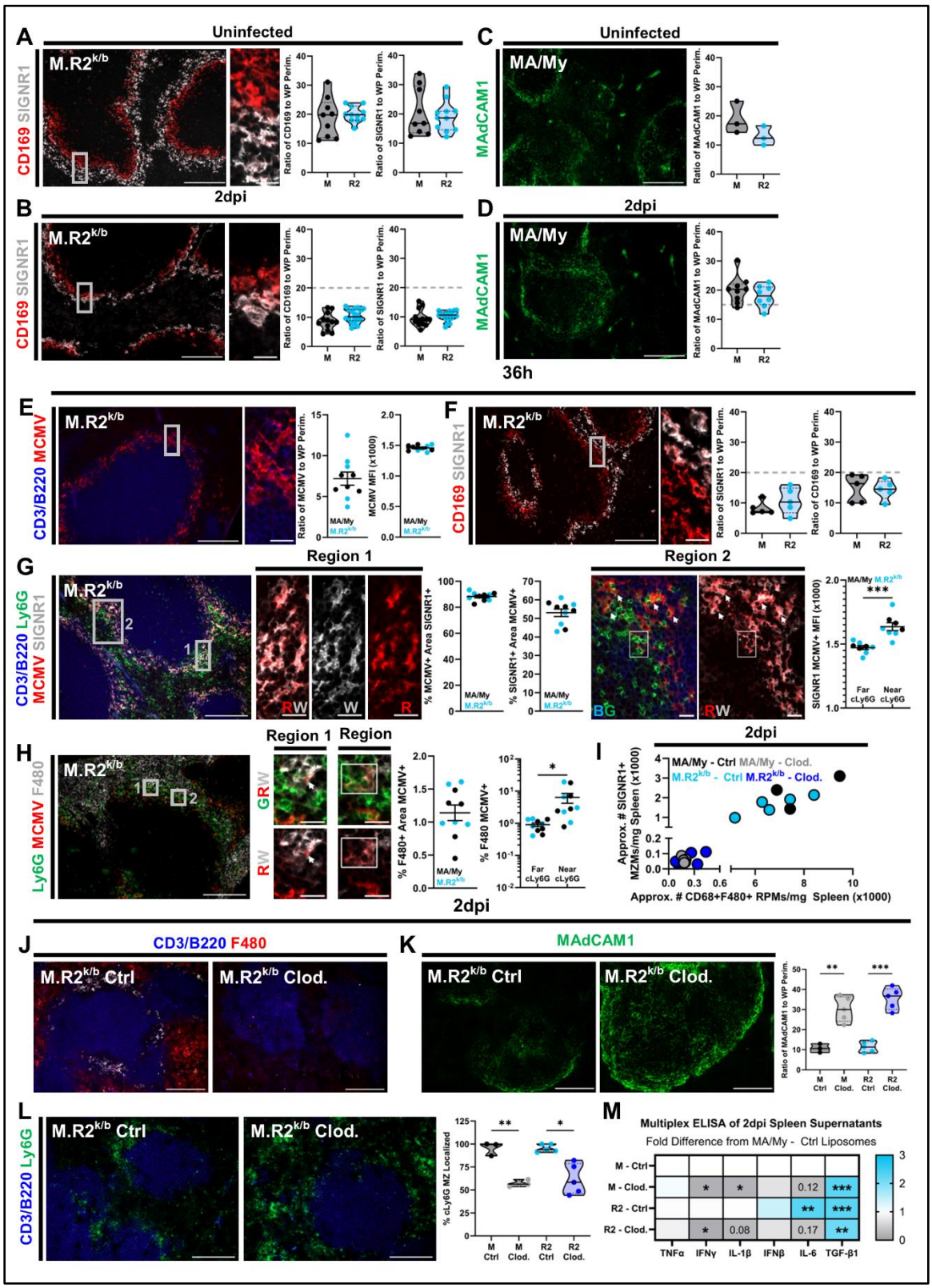
A
Uninfected
CD169 SIGNR1
M.R2k/b
Ratio of CD169 to WP Perim.
Ratio of SIGNR1 to WP Perim.
M
R2
B
2dpi
C
Uninfected
MAdCAM1
MA/My
Ratio of MAdCAM1 to WP Perim.
D
2dpi
36h
E
CD3/B220 MCMV
Ratio of MCMV to WP Perim.
MCMV MFI (x1000)
MA/My
M.R2k/b
F
CD169 SIGNR1
G
Region 1
Region 2
CD3/B220 Ly6G
MCMV SIGNR1
RW
W
R
BG
% MCMV+ Area SIGNR1+
% SIGNR1+ Area MCMV+
SIGNR1 MCMV+ MFI (x1000)
***
Far cLy6G
Near cLy6G
H
Region 1
Region
Ly6G MCMV F480
GRW
RW
% F480+ Area MCMV+
% F480 MCMV+
*
I
2dpi
MA/My - Ctrl
MA/My - Clod.
M.R2k/b - Ctrl
M.R2k/b - Clod.
Approx. # SIGNR1+ MZMs/mg Spleen (x1000)
Approx. # CD68+F480+ RPMs/mg Spleen (x1000)
J
CD3/B220 F480
M.R2k/b Ctrl
M.R2k/b Clod.
K
MAdCAM1
**
***
M Ctrl
M Clod.
R2 Ctrl
R2 Clod.
L
CD3/B220 Ly6G
% cLy6G MZ Localized
M
Multiplex ELISA of 2dpi Spleen Supernatants
Fold Difference from MA/My - Ctrl Liposomes
M - Ctrl
M - Clod.
R2 - Ctrl
R2 - Clod.
0.12
0.08
0.17
TNFα
IFNγ
IL-1β
IFNβ
IL-6
TGF-β1

Figure 3.5. Infection of Macrophages Coincides with MZ Neutrophil Recruitment and Spleen IL-6 Production During Early MCMV Infection. Representative images and quantification for **(A)** Uninfected MZMs, **(B)** 2dpi MZMs, **(C)** Uninfected MAdCAM1+ MZRCs, **(D)** 2dpi MAdCAM1+ MZRCs, **(E)** 36hpi MCMV-GFP, **(F)** 36hpi MZMs, **(G)** 36hpi MCMV-GFPI/SIGNR1+ MZMs/Ly6G+ neutrophils**,** and **(H)** 36hpi MCMV-GFP/F480+ RPMs/Ly6G+ neutrophils. **(I)** Approximate numbers of SIGNR1+ MZMs and CD68+F480+ RPMs/mg spleen at 2dpi with clodronate liposome or control liposome treatment. Quantities assessed using flow cytometry. **(J)** Representative images of spleen macrophage staining in 2dpi spleens with clodronate liposome or control liposome treatment. Representative images and quantification for 2dpi **(K)** MAdCAM1+ MZRCs or **(L)** Ly6G+ neutrophils, in spleens with clodronate liposome or control liposome treatment. **(M)** Multiplex ELISA from 2dpi macrophage depleted spleen supernatants as fold difference over MA/My treated with control liposomes. Statistics represented are comparisons to the MA/My – control liposomes group. Full image scale bars at 200 microns, insert scale bars at 20 microns. Grey dashed lines indicate values of uninfected image quantification. NWP = Non-White Pulp. Violin plots depict median (solid line) and quartile (dashed line) values. Dot plot error bars depict mean and SEM. Heatmaps depict mean values. Data pooled from: **(A)** 3 independent experiments with total 9-11 mice per group. **(B)** 4 independent experiments with total 13-18 mice per group. **(C)** 1 independent experiment with 3 mice per group. **(D)** 2 independent experiments with total 8-9 mice per group. **(E-H)** 1 independent experiment with 5 mice per group. **(I-M)** 1 independent experiment with 3-5 mice per group. Statistical comparisons made using **(A-H)** unpaired Welch's t-test, **(K, L)** Brown-Forsythe and Welch ANOVA test with Dunnett's T3 test for multiple comparisons, or **(M)** 2-way ANOVA with Dunnett's multiple comparisons test. Outliers are removed if identified by a Grubb's outlier test at alpha < 0.05. * $p < 0.05$, ** $p < 0.01$, *** $p < 0.001$, **** $p < 0.0001$.

Additionally, we observed direct contacts between Ly6G+ neutrophils and the MCMV-GFP+ SIGNR1+ MZMs (Fig. 3.5G, Region 2, Arrows), as well as MCMV-GFP+ SIGNR1+ cells displaying debris-like morphology (Fig. 3.5G, Region 2, Box). If immunogenic death of infected cells was responsible for neutrophil recruitment to the MZ during early infection, we would expect to see evidence of increased MCMV spread into surrounding cells closer to the neutrophil clusters. To test this, we co-stained slides with MCMV-GFP, Ly6G, and F480, a macrophage marker highly expressed on red pulp macrophages (RPMs) but not MZMs. While only 1.14% of F480+ area colocalized with MCMV-GFP, it was nearly exclusively found in RPMs that were immediately adjacent to Ly6G+ neutrophil clusters (Fig. 3.5H). Prior work has shown that progressing MCMV infection in macrophages leads to downregulation of cell surface markers including F480[180]. In line with this observation, we saw that while most MCMV-GFP+ RPMs had low levels of MCMV-GFP staining and bright F480, RPMs that had more MCMV-GFP staining coincided with diminished F480 (Fig. 3.5H, Region 1 vs. Region 2). Although low-level MCMV-GFP+ RPMs, particularly those containing brighter spots (Fig.3.5, Region 1), may be phagocytosing MCMV-GFP+ MZM debris, both situations (increased spread of infection via necrosis or increased phagocytosis of infected cell corpses) around neutrophil clusters support the hypothesis that MCMV-GFP+ MZMs may be dying.

We directly assessed the impact of MZMs on neutrophil recruitment to the marginal zone by depleting macrophages from the spleen using clodronate liposomes injected one day prior to MCMV infection, then examining the spleens at 2 dpi. We verified depletion of macrophages by flow cytometry (Fig. 3.5I) and IF imaging (Fig. 3.5J). We additionally verified that MAdCAM1+ MZRCs were not impacted by our macrophage depletion strategy, finding that the macrophage depleted spleens in both strains had significantly increased MAdCAM1 staining at the MZ (Fig. 3.5K). While neutrophils were still recruited to the macrophage depleted spleen, they were no longer specifically localized to the MZ, instead they were observed in smaller clumps throughout the red pulp (Fig. 3.5L). This data supports the hypothesis that MCMV-GFP+ MZMs contribute to the early recruitment of neutrophils to the MZ. Assessment of cytokines in the macrophage-depleted spleens at 2 dpi revealed macrophages as the source of the increased IL-6 seen in M.R2$^{k/b}$ spleens over MA/My (Fig. 3.5M), suggesting a *Cmv5*^{s}-driven increase in macrophage activation. Interestingly, depletion of macrophages in the M.R2$^{k/b}$ spleens did not alleviate the increased TGF-β1 over MA/My counterparts, instead inducing an increase in TGF-β1 comparable to the M.R2$^{k/b}$ samples (Fig. 3.5M). Together this data shows that macrophages are responsible for the differences in cytokine environment between strains, and supports a model in which the death of infected MZMs leads to MZ neutrophil infiltration early during MCMV infection.

M.R2$^{k/b}$ Spleens Display a Buildup of MZM Debris and Substantial RPM Loss Coinciding with Histopathology by day 4 of MCMV infection. Early splenic damage at the M.R2$^{k/b}$ MZ was shown to progress towards MZ dissolution with mounting cell death and debris along with a substantial loss of red pulp cellularity by 4 dpi[175]. MZ dissolution also occurred in the MA/My spleens, however the damage was less severe at 4 dpi and

showed minimal red pulp involvement[175] (Fig. 3.6A). To determine if the MZM populations are differently impacted after the initial loss, we stained MA/My and M.R2$^{k/b}$ spleen sections at 4 dpi. We found that MZM staining in the MA/My spleens was mostly gone, with some dim staining still apparent. However, M.R2$^{k/b}$ MZs displayed an increased buildup of bright, punctate debris-like MZM staining that aligned with clusters of cCasp3 (Fig. 3.6B). Due to disparity in the extent of red pulp damage between strains along with evidence suggesting a buildup of debris at the M.R2$^{k/b}$ MZ, we next assessed the state of RPMs at this later timepoint during acute infection. In uninfected spleens, RPMs blanketed the red pulp with bright F480 expression on the cell surface and mostly intracellular CD68 (Fig. 3.6C). While both strains displayed a loss of RPMs from baseline by 4 dpi, this was strikingly more evident in the M.R2$^{k/b}$ spleens (Fig. 3.6D). Additionally, M.R2$^{k/b}$ RPMs appeared morphologically abnormal, and in some areas damaged (Fig. 3.6D, Side Region). To determine if destruction at the MZ and in the red pulp of M.R2$^{k/b}$ spleens was limited to macrophages, we assessed the state of ERTR7+ fibroblasts which were comparable in uninfected spleens (Fig. 3.6E), as well as MAdCAM1+ MZRCs. At 4 dpi, there was a statistically significant difference between MA/My and M.R2$^{k/b}$ MZRCs, however neither strain appeared below the levels of staining seen at baseline. While both strains had lost ERTR7+ fibroblasts from baseline, there was no difference in the loss between strains (Fig. 3.6F). This data suggests that development of widespread spleen acellularity during MCMV infection is due to a specific regulation of macrophage loss by *Cmv5*^{s}.

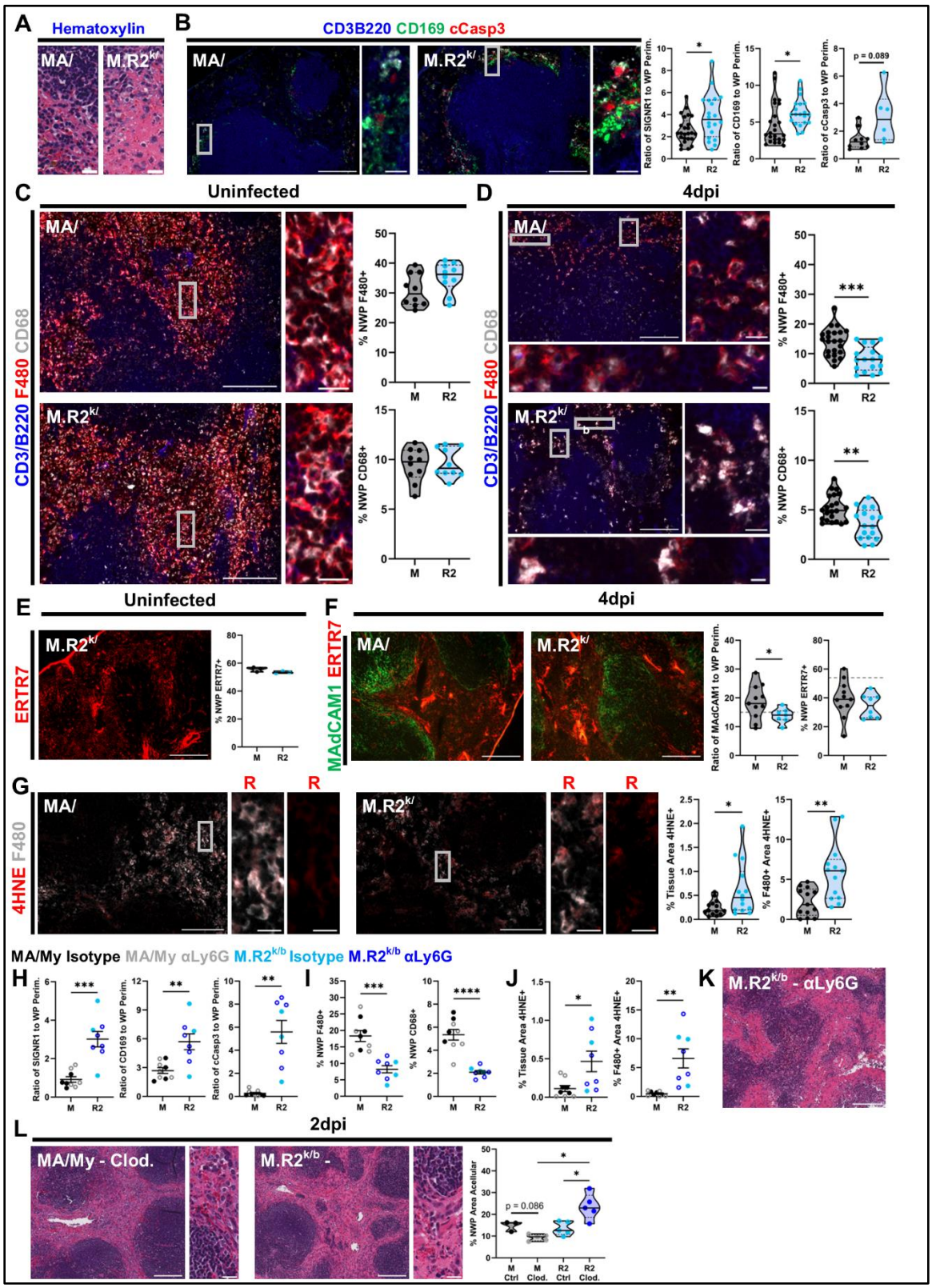
A
Hematoxylin
MA/
M.R2k/
B
CD3B220 CD169 cCasp3
MA/
M.R2k/
Ratio of SIGNR1 to WP Perim.
Ratio of CD169 to WP Perim.
Ratio of cCasp3 to WP Perim.
p = 0.089
C
Uninfected
D
4dpi
CD3/B220 F480 CD68
% NWP F480+
% NWP CD68+
E
Uninfected
ERTR7
% NWP ERTR7+
F
4dpi
MAdCAM1 ERTR7
Ratio of MAdCAM1 to WP Perim.
G
4HNE F480
R
% Tissue Area 4HNE+
% F480+ Area 4HNE+
MA/My Isotype MA/My αLy6G M.R2k/b Isotype M.R2k/b αLy6G
H
I
J
K
M.R2k/b - αLy6G
L
2dpi
MA/My - Clod.
M.R2k/b -
% NWP Area Acellular
p = 0.086
M Ctrl
M Clod.
R2 Ctrl
R2 Clod.

Figure 3.6. M.R2$^{k/b}$ Spleens Display a Buildup of MZM Debris and Substantial RPM Loss Coinciding with Histopathology by day 4 of MCMV infection. **(A)** Representative cropped images of spleen histology sections from indicated genotypes at 4dpi. Representative images and quantification for **(B)** 4dpi MZMs and cCasp3, **(C)** Uninfected RPMs, **(D)** 4dpi RPMs, **(E)** Uninfected ERTR7+ fibroblasts, **(F)** 4dpi ERTR7+ fibroblasts and MZRCs, and **(G)** 4dpi RPMs and 4HNE. **(H-J)** 4dpi neutrophil depletion image quantifications. **(K)** Representative image of neutrophil depleted spleen histology. **(L)** Representative images with quantification for macrophages depleted 2 dpi spleen sections. Full image scale bars at 200 microns, insert scale bars at 20 microns. Grey dashed lines indicate values of uninfected image quantification. NWP = Non-White Pulp. Violin plots depict median (solid line) and quartile (dashed line) values. Dot plot error bars depict mean and SEM. Data pooled from: **(B)** SIGNR1 and CD169 data - 7 independent experiments with total 20-24 mice per group, cCasp3 data - 2 independent experiments with total 6-10 mice per group. **(C)** 2 independent experiments with total 10 mice per group. **(D)** 6 independent experiments with total 17-22 mice per group. **(E)** 1 independent experiment with 3 mice per group. **(F)** 3 independent experiments with total 7-11 mice per group. **(G)** 4 independent experiments with total 14 mice per group. **(H-L)** 1 independent experiment with 3-5 mice per group. Statistical comparisons made using an unpaired Welch's t-test, outliers are removed if identified by a Grubb's outlier test at alpha = 0.05. * $p < 0.05$, ** $p < 0.01$, *** $p < 0.001$, **** $p < 0.0001$.

Asking if the loss of RPMs and abnormal morphology in the remaining cells at 4 dpi was associated with increased oxidative stress, we stained spleen sections with F480 and 4HNE. While 4HNE was apparent in both strains at this timepoint, there was significantly more staining in the M.R2$^{k/b}$ spleens and it localized with nearly all remaining M.R2$^{k/b}$ RPMs as well as around the MZ (Fig. 3.6G). This data suggests that M.R2$^{k/b}$ spleens have a continued high level of inflammation and oxidative stress at 4 dpi. As neutrophils were responsible for the increased 4HNE earlier at the M.R2$^{k/b}$ MZ, we asked if neutrophils were responsible for any of these 4 dpi macrophage phenotypes. Neutrophil depletion revealed no differences in buildup of MZM debris and cCasp3 at the MZ (Fig. 3.6H), loss of RPMs (Fig. 3.6I), or the buildup of 4HNE (Fig. 3.6J), with data from isotype-treated groups in both strains falling directly on top of data from groups that were depleted of neutrophils. In line with this, neutrophil depletion did not alleviate 4dpi *Cmv5*^{s} histopathology (Fig. 3.6K). Finally, we found that depleting macrophages from 2 dpi spleens, prior to F480+ RPM loss, induced significant acellularity in M.R2$^{k/b}$, but not MA/My, mice (Fig. 3.6L). Together this data identifies inflammation and macrophage loss mirroring the spatial and temporal regulation of tissue damage during acute MCMV infection in M.R2$^{k/b}$ mice.

Discussion.

We previously found that the activation and expansion of antiviral NK cells were similar in MA/My and M.R2$^{k/b}$. Additionally, no differences in the intrinsic ability of NK cells to become activated and perform basic functions were identified. In the current work, we further investigate this model, seeking to better understand the development of *Cmv5*^{s} histopathology. Though MZ MCMV infection, initial neutrophil recruitment, and the loss of MZMs at 36 hpi did not vary between strains, by 2dpi the M.R2$^{k/b}$ environment was significantly more inflammatory with higher IL-6 and TGF-β1 alongside increased MZ neutrophil infiltration and cell death, leading us to hypothesize a more immunologically focused mechanism of *Cmv5*^{s}. For example, myeloid cells, including both neutrophils and macrophages, could be more susceptible to oxidative stress in M.R2$^{k/b}$ mice, which prolongs the initial influx of neutrophils, and causes the death of MZMs and RPMs in a manner that propagates inflammation. This result could also be achieved by defects in phagocytic clearance of dead and dying cells, or any one of many metabolic processes influencing macrophage activation. Future studies will seek to assess differences in myeloid cell function that may contribute to this genetic divergence in pathology.

Data presented supports a model in which MCMV enters the spleen at the MZ and infects SIGNR1+ MZMs, which eventually die, spreading the virus to surrounding cells and recruiting neutrophils. Sometime shortly after the initial wave of neutrophil recruitment seen around 36 hpi, M.R2$^{k/b}$ mice diverge from MA/My counterparts, exhibiting increased neutrophil infiltration, death, and oxidative stress at the MZ. This could be explained by M.R2$^{k/b}$ neutrophils dying by a more immunogenic mechanism than MA/My neutrophils, which could prevent the resolution of inflammation and prolong inflammatory conditions directly and indirectly through damage to nearby infected MZMs. An alternative hypothesis

would be that dying MZMs recruit more neutrophils to the M.R2$^{k/b}$ MZ because they themselves are dying more immunogenically, or not being cleared effectively post-death leading to secondary necrosis.

Supporting the idea of impaired cell clearance post death, we show that at 4dpi, MZM debris builds up at the M.R2$^{k/b}$ MZ, and while clusters of cell debris colocalize with clusters of cCasp3, MZM cell debris does not perfectly colocalize with cCasp3, suggesting this buildup of cell debris may be caused in part by reduced clearance of apoptotic MZMs. However, inflammation and DAMP release caused by this secondary necrosis may lead to apoptosis of other MZ cells, such as MAdCAM1+ MZRCs, which are reduced in the M.R2$^{k/b}$ spleens at 4dpi. Of note, 4dpi M.R2$^{k/b}$ MZMs are marked by significant 4HNE staining, suggesting ongoing inflammation. Both strains exhibited a loss of RPMs from baseline at 4 dpi, but M.R2$^{k/b}$ spleens display increased loss over MA/My counterparts. Additionally, remaining M.R2$^{k/b}$ RPMs displayed abnormal morphology, appearing more ameboid, and in some cases fragmented, when compared to RPMs from MA/My mice at the same timepoint. This loss of macrophages could cause a buildup of MZM debris by depleting the spleen of available professional phagocytes. Future studies will seek to better characterize the mechanisms of cell death involved in M.R2$^{k/b}$ neutrophils and macrophages during MCMV infection, as well as any differences in phagocyte clearance of these dying cells.

Previous work suggested that stromal cells may be an early cell type infected at the MZ, however the reported data suggests that an additional unlabeled MZ cell type is also infected early, and quickly becomes the predominantly infected cell at the MZ by 2dpi[136]. Our data showed that by 36hpi, most MCMV-GFP+ cells in the spleen were SIGNR1+

MZMs. Evidence has shown that the presence of macrophages can protect fibroblasts from becoming infected, and their depletion *in vivo* causes increased MCMV replication in the spleen[181-183]. If depletion of macrophages prior to infection caused a more progressive infection in spleen fibroblasts, it could explain why neutrophils were more dispersed in the red pulp area rather than the MZ in macrophage depleted mice. Our data suggest an important role for macrophages in *Cmv5*^{s}-mediated MCMV infection and pathology.

Increased IFNβ seen at 2 dpi in M.R2$^{k/b}$ spleens was reduced with neutrophil depletion, and increased IL-6 was eliminated with the depletion of macrophages, however neither of these treatments reduced the increased TGF-β1. A clue to how this may be working comes from the evidence that macrophage depletion of MA/My mice induces an increase of TGF-β1 in line with that seen in M.R2$^{k/b}$ control spleens. Increased activation of fibroblasts and other stromal cell populations in macrophage depleted spleens, along with the increased need for them to phagocytosis dying cells and debris could lead to an increase in fibroblast TGF-β1 production in MA/My mice. Some of these activating pressures are more present in untreated M.R2$^{k/b}$ spleens during MCMV infection due to the high amounts of cell death in neutrophils, MZMs, and later RPMs, which could explain why TGF-β1 is increased without macrophage depletion in M.R2$^{k/b}$ mice. Future exploration will need to include a more in-depth characterization of stromal cells during MCMV infection in MA/My and M.R2$^{k/b}$ spleens.

Overall, we describe differential regulation of neutrophil recruitment, inflammation, and macrophage cell death corresponding with increased susceptibility in a genetic model of acute viral infection-induced tissue damage. This work, and future work using this model, serves to enhance our understanding of these processes in tissue damaging infections,

with the goal of increasing the efficacy of medical interventions for individuals experiencing severe pathology during viral infections.

Chapter IV: Conclusions and Future Directions

Working Model of *Cmv5*^{s}-Driven Susceptibility and Spleen Tissue Damage During Acute MCMV Infection. This section refers to Figure 4.1.

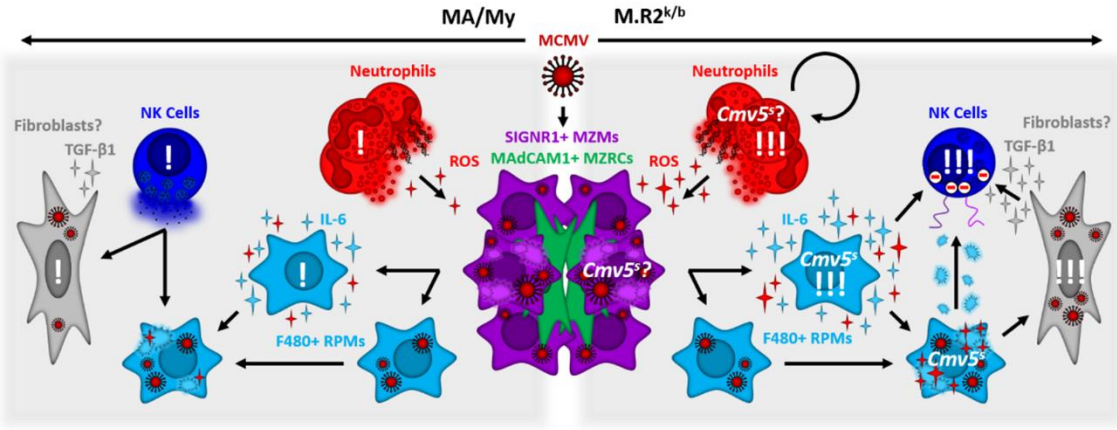

Figure 4.1. Working Model for the Development of *Cmv5*^{s}-Induced Susceptibility and Tissue Damage During Acute MCMV Infection.

With the information we've gathered regarding *Cmv5*^{s}-driven susceptibility and tissue damage during acute MCMV infection, we can put together a model of how things may be working together to induce and propagate pathology in M.R2$^{k/b}$ mice. MCMV enters the spleen at the MZ, and establishes infection in SIGNR1+ MZMs. The SIGNR1+ MZMs that were infected earliest show increased positivity for MCMV and begin to die around 36hpi: recruiting neutrophils, activating surrounding RPMs, and spreading the virus. This initial wave of neutrophil recruitment and SIGNR1+ MZM loss seen at 36hpi does not differ between strains, suggesting that the response to SIGNR1+ MZM loss, rather than the loss itself, is the target of the first "hit" of *Cmv5*^{s} located within the R5 genetic interval (or first *Cmv5*^{s} locus, *Cmv5*^{s}-L1). In line with this idea, there is no apparent difference in CD169 or SIGNR1 MZM loss by 2dpi, despite the increased infiltration of neutrophils and spleen IL-6/TGF-β1 in *Cmv5*^{s} mice. This data, along with the appearance of necrotic

histopathology at the marginal zone of MA/My-UHD mice, is consistent with the early cause of SIGNR1+ MZM death being the progression of MCMV infection in SIGNR1+ MZMs.

If the full 2dpi phenotype appears in the M.R5$^{k/b}$ mice, it makes the most sense that this first effect of *Cmv5*^{s} is an increased inflammatory activation of macrophages. In this case, an identical first wave of infected MZM loss around 36hpi leads to a rapid accumulation of neutrophils at the MZ that does not differ between strains. Death of SIGNR1+ MZMs in an immunogenic enough manner to recruit neutrophils would also activate surrounding macrophages, where *Cmv5*^{s} triggers an increased reaction, leading to more RPM IL-6 production and a stronger second wave of neutrophils than MA/My counterparts by 2dpi. In this model, the spread of MCMV is the major inducer of SIGNR1+ MZM death at the marginal zone, but an increased acute inflammatory reaction to this death by surrounding macrophages leads to the production and release of acute inflammatory mediators, exacerbating the death of infected MZMs. This increased death and professional phagocyte loss, along with the build-up of neutrophil corpses, activates surrounding fibroblasts to produce TGF-β1 and delays clearance of the MZ cell debris. Together this accounts for the 2dpi marginal zone necrotic histopathology in M.R5$^{k/b}$ and M.R2$^{k/b}$ mice, and a lack of additional input from *Cmv5*^{s} would allow NK cells to effectively clear the virus as it spreads into the red pulp, explaining why the M.R5$^{k/b}$ mice do not progress to increased viral load and widespread red pulp cell loss, despite the presence of significant MZ histopathology.

The M.R2$^{k/b}$ mice experience a second “hit” from *Cmv5*^{s}, located somewhere in the second *Cmv5*^{s} locus (*Cmv5*^{s}-L2), and occurring around 3dpi as the virus spreads into the red pulp.

A second effect of *Cmv5*^{s} being an increased susceptibility to activation- or oxidative stress-induced cell death, potentially via metabolic mediators, would explain how increased inflammation and death at the MZ progresses throughout the red pulp as RPMs become increasingly activated. The increased macrophage activation would likely lead to production of IL-12 and IL-18, which are cytokines associated with the upregulation of TIM3 on NK cells[102]. The increased macrophage death would increase viral spread directly and by allowing the virus to spread more rapidly through stromal cells[181-183], potentially overwhelming NK cell-mediated immunity. As time progresses, loss of professional phagocytes would cause a buildup of RPM debris and ongoing inflammation marked by high levels of DAMPs, further inhibiting NK cell function via checkpoint receptors TIM3 and LAG3[100]. This would present histologically as widespread red pulp acellularity and necrosis, and explain the loss of viral control evident in M.R2$^{k/b}$ mice by 4dpi.

Together this model proposes a cellular-level mechanism of action for *Cmv5*^{s}-driven MCMV susceptibility and spleen tissue damage, centered predominantly around macrophage-mediated inflammation and cell death. Within this model lies several testable genetic, molecular, and cellular hypotheses behind how MHC-linked polymorphisms translate into protein-level mediators, that regulate cellular functions and drive tissue pathology during acute viral infection. Experimental interrogation of these hypotheses will be required to fully understand *Cmv5*^{s}-mediated disease. Further discussion of these hypotheses and experiments constituting some immediate next steps toward progressing this work are outlined in the sections below.

Increased Inflammation Drives Necrotic Histopathology and Neutrophil Recruitment at the Early *Cmv5*^{s} Marginal Zone.

The starting hypothesis regarding the role of *Cmv5*^{s} in the development of MCMV susceptibility and spleen tissue damage is that while the infection of SIGNR1+ MZMs, their death, and the first wave of neutrophil recruitment to the MZ do not differ between strains, *Cmv5*^{s} causes surrounding macrophages to become more activated in response. We further hypothesize that this additional acute phase inflammation leads to an increase in immunogenic cell death and accumulation of neutrophils at the *Cmv5*^{s} marginal zone by 2dpi. We can break this down into two initial testable claims: (1) *Cmv5*^{s} macrophages have an increased inflammatory response to infected macrophage death, and (2) MZM necrosis is responsible for the increased *Cmv5*^{s} recruitment of neutrophils and necrotic histopathology.

Cmv5*^{s} *macrophages have an increased inflammatory response to infected macrophage death. This claim can be initially tested *in vitro*, which I strongly advise, as a working *in vitro* system for *Cmv5*^{s} regulation opens a lot of doors for mechanistic work that is difficult to do *in vivo* using a non-C57BL/6 mouse system. In this assay, macrophages are isolated from uninfected mice from both genotypes, and split into two groups. One group is infected *in vitro* with MCMV-GFP (M_i or $R2_i$), while the other remains uninfected and is labeled with a cell tracking dye (M_u or $R2_u$). Once a chunk of the infected cells has begun to round up, the labeled cells are added and allowed to incubate for a period of time prior to assessment (Fig. 4.2A). Upon completion of the co-culture assay, supernatants should be assessed for RS and LDH activity by commercial assay, along

with IL-6 and HMGB1 by ELISA or western blot. Uninfected cells should also be assessed for activation by flow cytometry.

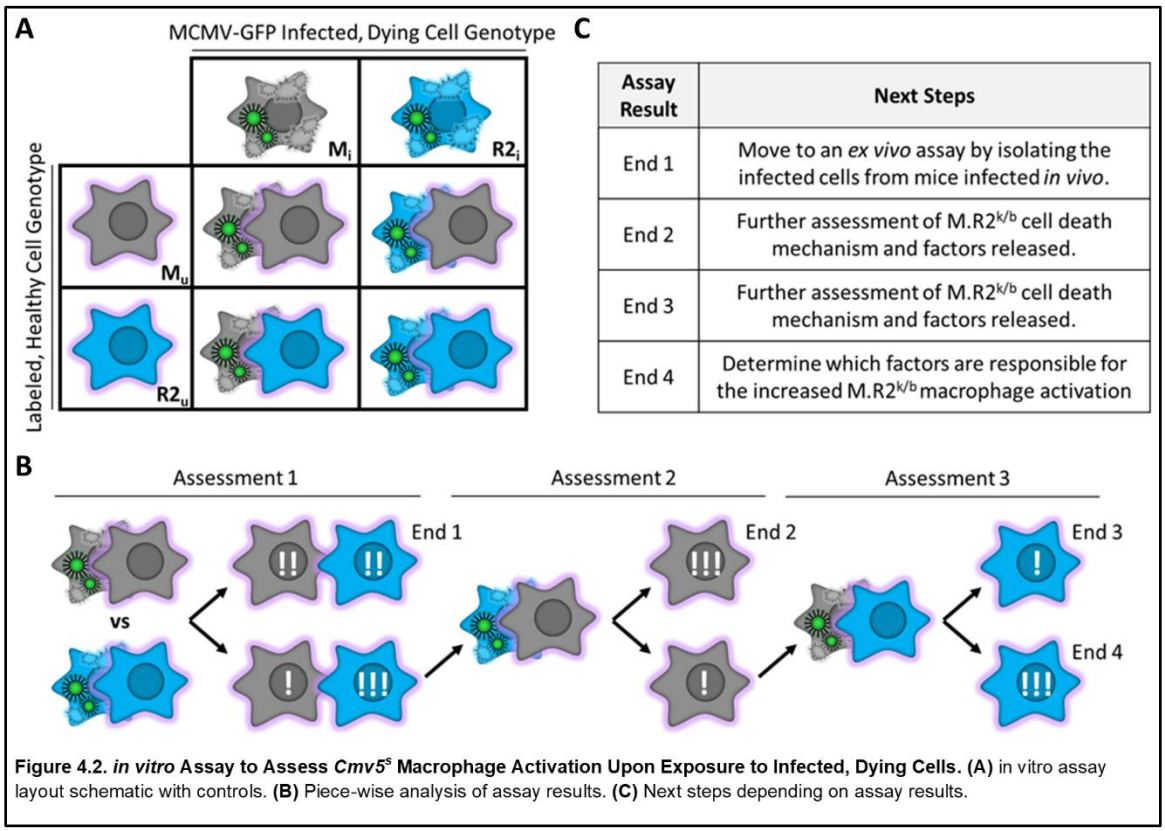

Figure 4.2. *in vitro* Assay to Assess *Cmv5*^{s} Macrophage Activation Upon Exposure to Infected, Dying Cells. (A) in vitro assay layout schematic with controls. **(B)** Piece-wise analysis of assay results. **(C)** Next steps depending on assay results.

The results of this assay are best assessed in a piece-meal manner, with individual outcomes bearing different conclusions (Fig. 4.2B). First, comparing M_i/M_u and $R2_i/R2_u$ assay control wells allows us to determine if we can see any differences between strains using this *in vitro* assay (Fig. 4.2B, Assessment 1). Observing no differences between these wells results in the remainder of this assay being inconclusive (Fig. 4.2B, End 1). However, if we are able to see increased M.R2$^{k/b}$ macrophage activation and/or inflammation, we can further assess the $R2_i/M_u$ well (Fig. 4.2B, Assessment 2). This well asks if the difference seen in macrophage activation between strains is due to the genotype of the dying cell. Seeing an increase in MA/My macrophage

activation/inflammation in this well suggests that the M.R2$^{k/b}$ macrophages are dying in a more immune-activating manner than the MA/My macrophages (Fig. 4.2B, End 2). Our model suggests that it is not the cell death event, but rather the reaction to it, that is regulated by *Cmv5^{s}*. If this is correct, we should see that MA/My macrophages are not more activated in the $R2_i/M_u$ well than they are in the M_i/M_u control. In this case we can proceed to the final experimental condition: the $M_i/R2_u$ well (Fig. 4.2B, Assessment 3). This well asks if the M.R2$^{k/b}$ macrophages are similarly highly activated in response to dying MA/My cells. If we see that the M.R2$^{k/b}$ macrophages now have reduced activation compared to the $R2_i/R2_u$ well, it suggests that *Cmv5^{s}* causes an increased susceptibility of surrounding M.R2$^{k/b}$ macrophages to something that is not released when the dying cells come from MA/My mice (Fig. 4.2B, End 3). Finally, the result that uninfected macrophages from M.R2$^{k/b}$ mice are similarly highly activated in the $R2_i/R2_u$ and $M_i/R2_u$ well is entirely consistent with our working model (Fig. 4.2B, End 4), and can be further dissected in additional experiments prior to testing *in vivo* (Fig. 4.2C).

MZM necrosis is responsible for the increased Cmv5^{s} recruitment of neutrophils and necrotic histopathology. This claim can be tested initially *in vivo* using low dose clodronate liposomes at 36hpi to induce apoptosis selectively in the MZMs[121, 184]. The readout for this assay would be 2dpi neutrophil recruitment and necrotic histopathology at the MZ. At the 36hpi timepoint, early neutrophil clusters forming around highly infected SIGNR1+ MZMs at the MZ, but there are no apparent differences between strains. Inducing apoptosis in MZMs at this timepoint would prevent the engagement of an immunogenic cell death pathway, and because this timepoint is prior to more significant RPM infection and activation, should also be cleared relatively quickly, preventing secondary necrosis. If our model is correct, induction of MZM apoptosis in M.R2$^{k/b}$ mice at

36hpi should prevent the *Cmv5*^{s}-driven increase in neutrophil accumulation and necrotic histopathology, demonstrating the requirement of immunogenic MZM death. Information obtained from this experiment could also support alternative hypotheses, for example, if the induction of apoptosis in MZMs does not eliminate the necrotic histopathology, it would support the idea that MZ necrosis comes from some sort of defect in *Cmv5*^{s} efferocytosis, leading to secondary necrosis. Additionally, if induction of MZM apoptosis eliminates the necrotic histopathology but does not decrease neutrophil infiltration, it suggests that increased MZ cell activation, rather than death, is responsible for the *Cmv5*^{s} MZ neutrophil recruitment. Results from this experiment would pave the way for follow up questions both *in vivo* and *in vitro* regarding mechanisms and causes of macrophage death, activation, and/or efferocytosis.

Increased Susceptibility to Activation- or Oxidate Stress-Induced Cell Death Drives *Cmv5*^{s} Red Pulp Pathology.

According to our model, the second major hypothesis regarding the role of *Cmv5*^{s} in the development of MCMV susceptibility and spleen tissue damage is that viral progression into the red pulp along with the increasing activation causes *Cmv5*^{s} RPMs to display an increased susceptibility to activation- or oxidative stress-induced cell death. We further hypothesize that this loss of RPMs is what drives the increased TGF-β1 production from spleen stromal cells and the buildup of debris at the MZ. Our macrophage depletion experiment confirms that depletion of macrophages from MA/My mice can cause an increase in TGF-β1 production in line with that seen in M.R2$^{k/b}$ mice, strongly supporting this piece of the model, however this will need to be repeated. This leaves us with one initial testable hypothesis: *Cmv5*^{s} macrophages are more susceptible to activation- or

oxidative stress-induced cell death. This can be relatively easily tested *in vitro* by exposing macrophages from *Cmv5*-disparate mice to a variety of activating stimuli and assessing cell death. I would suggest using an imaging readout for this cell death assay, as LDH activity degrades rapidly (and thus results are inconclusive for assays longer than ~4 hours), and bystander macrophages are likely to phagocytose at least some of the dead cells, which could confound analysis by flow cytometry. Imaging using a nuclear stain, a fixable viability dye, cCasp3, and F-actin should allow a good initial assessment of susceptibility to cell death, and whether that cell death is immunogenic. I would propose starting by stimulating the macrophages with CpG (ssDNA, TLR9 agonist), Poly I:C (dsRNA, TLR3 agonist), heat-inactivated MCMV, and 3dpi M.R2$^{k/b}$ spleen supernatants. This layout should give a broad view of potential mechanisms, depending on which (if any) wells have increased M.R2$^{k/b}$ cell death over MA/My.

In addition to the *in vitro* assay, time should be taken to further characterize the mechanisms of cell death occurring in *Cmv5*^{s} mice *in vivo*, starting around 60hpi. This can be done using imaging for various cell death pathway mediators over time, ideally using MCMV-GFP so infection of these macrophages can also be tracked. If the imaging becomes prohibitive, western blotting of spleen homogenates should be able to determine if different pathways are being activated in *Cmv5*-disparate spleens, but would have significantly reduced sensitivity due to the abundance of other cells in the spleen. Upon determination of cell death mechanism, inhibition/activation of the pathway *in vivo* should be assessed for contribution to 4dpi *Cmv5*^{s} pathology (increased viral load, red pulp acellularity, MZM debris buildup). If the cell death pathway is not apoptosis, this should be combined with an induction of apoptosis to determine if the RPM cell death needs to be immunogenic.

A Non-Conducive Immune Environment Prevents *Cmv5*^{s} NK Cells from Effectively Controlling Acute MCMV Infection.

Prior to infection, there were no differences between strains in the amount of NK cells in the spleen, the proportion of NK cells expressing Ly49G2, nor did we notice any apparent defects in NK cell maturation. Additionally, assessment of NK cell function revealed no differences in the ability of *Cmv5*^{s}-bearing M.R2$^{k/b}$ NK cells to perform basic effector functions upon stimulation *in vitro*. Assessment of the early NK cell response to MCMV infection at 2dpi additionally revealed no differences between strains, despite evidence of high levels of early NK cell activation, the beginning of effector Ly49G2+ subset expansion, and Ly49G2+ NK cell specific activation over Ly49G2- counterparts. This suggests no defects the ability of *Cmv5*^{s} NK cells to recognize and become activated in response to MCMV infection *in vivo*. Interestingly, at this timepoint we were able to identify necrotic histopathology along with inflammatory infiltrates at the M.R2$^{k/b}$ marginal zone, marking it as the first apparent *Cmv5*^{s} phenotype, prior to the divergence between strains in viral load, weight loss, or NK cell activation. This data suggests that the development of tissue damage is more likely to be the direct target of *Cmv5*^{s} than the regulation of NK cell function, as discussed above.

By 4dpi, *Cmv5*^{s} mice have significantly increased viral load and dramatic spleen tissue damage compared to MA/My counterparts, and spleen NK cells appear more activated by morphology (light scattering properties) and expression of activation-induced cell surface markers. Further assessment revealed an increased upregulation of non-classical checkpoint receptors TIM-3 and LAG-3 on *Cmv5*^{s} NK cells, but no defects in effector

function when stimulated *in vitro*. This data strongly suggests that something in the *in vivo* tissue environment is preventing NK cells from effectively exerting their effector functions and controlling MCMV infection in *Cmv5*^{s}-bearing mice. This could be explained by three different models: (1) Buildup of DAMPs and macrophage debris inhibit NK cell mediated MCMV control via checkpoint receptors, and this is why we have increased 4dpi viral load in M.R2$^{k/b}$ mice at 4dpi, (2) NK cells are required to prevent increased viral control, but are being inhibited by a different mechanism, or (3) progression of macrophage loss causes MCMV to spread more rapidly through stromal cells in *Cmv5*^{s} mice, ultimately overwhelming the NK cell response regardless of environmental inhibition.

If we were able to prevent *Cmv5*^{s}-driven RPM loss in M.R2$^{k/b}$ mice, assessment of the 4dpi viral load with this intervention could confirm or eliminate option (3) depending on whether the increased *Cmv5*^{s} viral load was resolved or not (respectively). If these mice still had increased viral load at 4dpi, the model proposed in (1) could be directly tested by additionally blocking TIM3 and/or LAG3 in vivo (starting around 2dpi, to make sure at least TIM3 has been upregulated) during infection and assessing 4dpi viral load. If we are unable to alleviate the increased viral load by blocking TIM3 and LAG3 in these mice, assessments should proceed to determine what else could be inhibiting NK cell function *in vivo* (model 2). If we do not have a model that shows increased viral load without the increased RPM loss, we can confirm model (1) if blocking TIM3 and LAG3 *in vivo* prevents the increased M.R2$^{k/b}$ 4dpi viral load, however a negative result in this experiment could be due to model (2) or model (3). Further testing from here gets trickier, as transfers of activated NK cells between MHC-mismatched mice is likely confounding, and depleting NK cells causes drastically increased viral load in both strains. In order to truly test this, we need to be able to separate the increased viral load from the increased RPM loss, so

if we do not get lucky with some of the genetic experiments proposed in the following section, I would propose postponing this question in favor of first characterizing the mechanism of *Cmv5*^{s} RPM loss at 4dpi.

Honing in on the Genetic Loci Responsible for *Cmv5*^{s}-Driven MCMV Susceptibility and Tissue Damage.

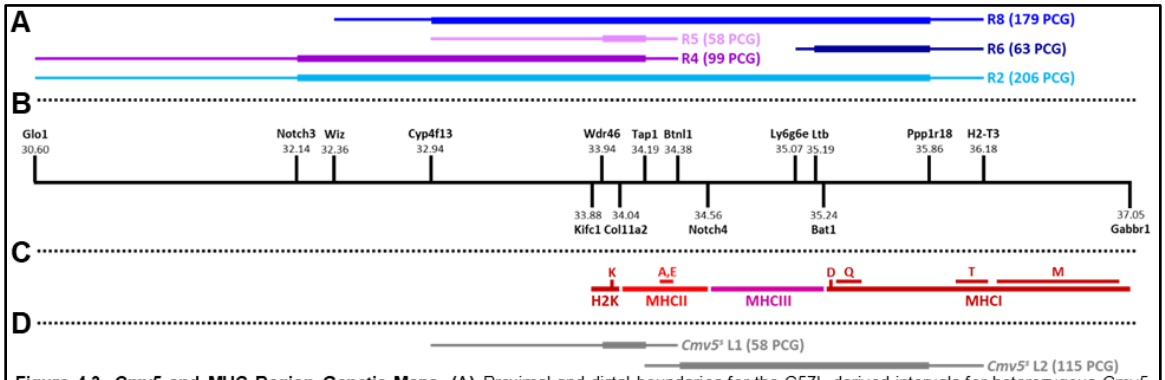

Figure 4.3. *Cmv5* and MHC Region Genetic Maps. (A) Proximal and distal boundaries for the C57L-derived intervals for heterozygous *Cmv5*-recombinant mouse strains identified and tested herein. Exact interval locations can be found in Table I. **(B)** Linear map of the *Cmv5* (top) and MHC (bottom) section boundary markers. **(C)** MHC region map with locations of major MHC-I and MHC-II molecules. **(D)** Proximal and distal boundaries *Cmv5*^{s} locus-containing intervals resulting from Chapter II mapping. Thin lines mark the space between MA/My-matching genotypes and thick lines depict the space between MA/My-differing genotypes. Exact location of genetic cross-overs fall somewhere in the area marked by the thin line.

Given the clinical importance of understanding genetic risk factors for severe outcomes of viral infection, identifying the genetic mediators of *Cmv5*^{s}-driven pathology is a critical future direction. Not only does this open up many additional tools and avenues of exploration essential for complete understanding of pathology in this system, but it also allows direct assessment of potentially comparable genetic susceptibility in human patients that could drive translation. By continued backcrossing of originally defined *Cmv5*^{s}-bearing M.H2$^{k/b}$ mouse[150] to MA/My parent and expanded genotyping coverage of the *Cmv5* interval, we were able to identify, establish, and test 5 *Cmv5*-recombinant congenic strains (intervals depicted in Fig. 4.3A) for *Cmv5*^{s}-driven MCMV susceptibility and tissue damage.

The M.R8$^{k/b}$ mouse (bearing the R8 interval, Fig. 4.3A - top), was the smallest C57L-derived interval to convey the full *Cmv5*^{s} phenotype *in vivo*, consisting of histopathology at the MZ and RP, as well as increased MCMV susceptibility defined by increased viral load and weight loss by 4dpi. This narrows the full phenotype *Cmv5* interval from the originally described 23.08 Mb region containing 428 protein coding genes (PCG), to the 3.82 Mb R8 region containing 179 PCG[18, 148] (Table IV). This constitutes a 6.04x reduction in the interval size and a 2.39x reduction in the total number of PCG, and hones all of the loci required for the full *Cmv5*^{s}-driven pathology to the MHC and immediately adjacent region (R8 interval, Fig. 4.3A – top, compared to Fig. 4.3C). Previously published whole exome sequencing[148] allows us to identify 80 of the 179 PCG in the R8 interval as containing coding polymorphisms, however any of the PCG within the C57L-derived interval could be responsible for the pathology due to polymorphisms in non-coding and regulatory regions that could convey differences in expression, splicing, or other modifications to the protein-level mediator. It could also be that a regulatory region in this interval conveys pathology during MCMV infection by influencing genes outside of the C57L-derived region, so in addition to our 179 PCG, we add 161 lncRNAs, 15 miRNAs, 5 snoRNAs, 6 snRNAs, 1 rRNA, and an unknown number of regulatory regions[18] (Table V) to the list of potential drivers for *Cmv5*^{s} pathology during MCMV infection.

All the information we have regarding genetic differences between the MA/My and C57L *Cmv5* haplotypes comes from exome sequencing done on the original *Cmv5*^{s}-bearing M.H2$^{k/b}$ mouse[148]. While the exome data has been extraordinarily helpful in the generation of genotyping primers and identifying differences in PCGs between strains, it is limited by its exclusion of most of the space contained within the interval. Therefore, immediate next steps in the assessment of the genetic mediators of *Cmv5*^{s} should be a comprehensive

characterization of the genetic differences between strains. This includes whole genome sequencing of the MA/My and M.R8$^{k/b}$ mice, allowing the identification of polymorphisms in non-coding regions such as RNA mediators and regulatory sequences. This would provide a comprehensive list of all of the potential drivers of *Cmv5*^{s} pathology during MCMV infection and allow us to increase our genotyping coverage, which would almost certainly reduce the phenotype associated interval sizes, as there are significant gaps between our genotyping markers, causing large areas of uncertainty with regards to interval boundaries (thin vs thick lines, see figure legend). In addition to the full genome sequencing, high-coverage RNA sequencing of splenocytes from uninfected MA/My and M.R8$^{k/b}$ mice would allow us to more clearly identify expression- and splicing-related gene differences, and could assist with the interpretation of genetic polymorphism in non-coding regions identified by the full genome analysis.

Generation of the M.R4$^{k/b}$ and M.R5$^{k/b}$ mice (bearing R4 and R5 intervals respectively, Fig. 4.3A – light and dark purple) allowed us to directly test the contribution of MHC-I molecule H-2K, along with some of the MHC-II region, to *Cmv5*^{s} pathology. Upon infection, M.R4$^{k/b}$ and M.R5$^{k/b}$ mice displayed a similar partial *Cmv5*^{s} phenotype consisting of MZ histopathology with minimal red pulp involvement and no increased weight loss or viral load by 4dpi. The consistent phenotypic presentation in two separate recombinant lines increases our confidence in the validity of this partial phenotype. As there was no increased pathology displayed in M.R4$^{k/b}$ over M.R5$^{k/b}$ mice, we are able to exclude genetic mediators that are present within the R4 but not R5 intervals (Fig. 4.3A – subtract R5 interval from R4 interval, Fig. 4.3B – Glo1 to Cyp4f13). This identifies a locus within the R5 interval as a contributor to *Cmv5*^{s} pathology during MCMV infection, however as M.R5$^{k/b}$ mice do not display substantial loss of red pulp cellularity, increased weight loss,

or increased viral load seen in the M.R2$^{k/b}$ (or M.R8$^{k/b}$) mice, there must be at least one additional contributing locus. Using this we can break up the full *Cmv5* interval into two separate contributing regions: locus 1 and locus 2 (L1 and L2, Fig. 4.3D). *Cmv5^{s}*-L1 lies within the R5 interval, while *Cmv5^{s}*-L2 is the remaining area within the R8 interval that conveys the full phenotype (subtracting out the R4-overlapping piece, see above).

An important assumption in our working model is that the M.R5$^{k/b}$ mouse will display all of the pathology seen in the M.R2$^{k/b}$ mice at 2dpi, consisting of the increased marginal zone necrotic histopathology, neutrophil infiltration, and IL-6/TGF-β1. While preliminary data may suggest this may be the case in M.R4$^{k/b}$ mice, at least for the histopathology and neutrophil infiltration, the 2dpi phenotype conveyed by the *Cmv5^{s}*-L1 interval remains to be fully characterized and is an essential future direction. If we assume that *Cmv5^{s}*-L1 conveys the full 2dpi pathology, our model suggests that the mediator within this first locus functions to increase the activation of macrophages surrounding the dying infected SIGNR1+ MZMs, this could occur via many different potential mechanisms. If we assume that the mediator of pathology within the *Cmv5^{s}*-L1 interval is a PCG with a coding polymorphism (for the sake of simplicity), MHC-II molecules emerge as high-priority targets. MHC-II molecules have been shown to act intracellularly to increase the response to TLR agonists[185]. The high expression of MHC-II on myeloid cells, coupled with the significant amount of polymorphism between MA/My and C57L MHC-II molecules, makes this mechanism an attractive target. Additionally, increased TLR signaling being the effect of *Cmv5^{s}*-L1 may explain why the MA/My-UHD and M.R5$^{k/b}$ mice had similar phenotypes at 4dpi.

The additional data that M.R2$^{k/b}$, M.R4$^{k/b}$, and M.R5$^{k/b}$ cells have increased MHC-II I-A/I-E antibody staining (clone M5/114.15.2) over MA/My counterparts *in vivo* allows us to conclude that even though the MHC-II loci are within the uncertainty area in the *Cmv5*^{s}-L1 interval, there are MHC-II differences in these mice. This could be due to differences in antibody binding due to protein polymorphism. As MA/My are I-E^{k} and I-A^{k}, and C57L mice are I-A^{b} (I-E^{null})[186], it could be that even though the M5/114.15.2 antibody positively binds both I-E^{k} and I-A^{b} [187], if it binds I-A^{b} with 3-5x higher affinity, it could explain the difference in MHC-II GMFI without necessarily being due to differences in MHC-II protein expression. This could be relatively easily tested using the high-coverage RNA sequencing proposed above, and by staining the cells with additional MHC-II antibody clones. This would verify if this increased GMFI is explained by antibody binding differences or differences in protein expression, but either outcome could potentially explain the *Cmv5*^{s}-L1 phenotype. If MHC-II differences are causing increased activation of *Cmv5*^{s} macrophages in response to stimulation, use of siRNA to knock down MHC-II expression *in vitro*, or siRNA liposomes *in vivo*, should reduce the phenotype. This could be further tested *in vitro* by expressing I-A^{b} in MA/My macrophages and assessing activation upon stimulation.

In addition to the H-2K/MHC-II region, generation of M.R6$^{k/b}$ mice (bearing the R6 interval, Fig. 4.3A – darkest blue) allowed us to directly test the contribution of the remaining MHC-I loci to *Cmv5*^{s} pathology (Compare Fig. 4.3A R6 interval to Fig. 4.3C MHCI region). Due to the importance of MHC-I, particularly H-2D, in this system[188, 189], we were surprised to find only minor differences between MA/My and M.R6$^{k/b}$ mice, despite M.R6$^{k/b}$ mice being heterozygous at H-2D. The largest phenotype associated with the R6 interval was the increased weight loss during infection, however the 3-4dpi slope began to level in these

mice while *Cmv5*^{s}-bearing M.R2$^{k/b}$ and M.R8$^{k/b}$ mice continued at a more consistent downward trend. In addition to this, M.R6$^{k/b}$ mice displayed a partial phenotype of increased NK cell activation. While the lack of increased viral load or apparent spleen damage suggests that M.R6$^{k/b}$ mice will not experience prolonged disease. the increased weight loss, even if it is resolving at 4/5dpi, is indicative of increased illness in M.R6$^{k/b}$ mice over MA/My counterparts during acute MCMV infection. Understanding this mechanism of action poses translational relevance for variation between individuals in response to the variety of acute and resolving illnesses humans experience on a regular basis. This R6 interval may or may not be required for full *Cmv5*^{s} pathology, however it does in itself convey some susceptibility to acute MCMV infection and is found within the full phenotype M.R8$^{k/b}$ region, cementing the contribution of an additional locus within this 1.11 Mb R6 interval containing 63 PCGs, of which 33 bear coding polymorphisms[18, 148] (Table IV).

Both the R5 and R6 intervals conveyed increased pathology during MCMV infection over MA/My counterparts. The R5 interval was associated with marginal zone destruction, while the R6 interval was associated with increased weight loss and NK cell activation, which may suggest an increased level of inflammation. A proposed immediate future direction is to breed the M.R5$^{k/b}$ and M.R6$^{k/b}$ mice together and test the combined strength of the regions to determine if the remainder of *Cmv5*^{s} pathology not contained within the R5 phenotype (red pulp acellularity and increased viral load) becomes synergistically apparent. This experiment with either show (a) no significant synergy, (b) some synergy that is still unable to match the R2/R8 pathology, or (c) a full *Cmv5*^{s} phenotype. If scenarios (a) or (b) are observed, it suggests the contribution of at least one additional locus to *Cmv5*^{s} pathology, bringing the total involvement to at least 3 loci. This third contributing locus would be found in the area between the R5 and R6 intervals (Fig. 4.3A), which

encompasses all of the MHCIII region of the MHC (Fig. 4.3C). The MHCIII region is home to many high-priority immune mediators, many of which hold coding polymorphisms between MA/My and C57L haplotypes[18, 148]. In this scenario, I would suggest that *Ager* and *Cfb* are the highest priority candidates, as the mutation found in *Ager* is located in a region important for protein oligomerization in response to DAMPs, and the mutation in *Cfb* is a premature stop codon that could significantly influence the alternative complement cascade. If scenario (c) is observed, it would exclude the MHCIII region polymorphisms as contributors to *Cmv5*^{s} pathology, further reducing the full phenotype-associated interval size. The R6 interval does not solely contain MHC-I molecules, and I propose inflammatory mediator *Ltb*, encoding TNF family member lymphotoxin beta, as the highest priority candidate for further investigation in this scenario. Differences in lymphotoxin beta signaling could link increased macrophage activation to increased cell death, causing the inflammatory loss of RPMs and increasing the viral load seen in full *Cmv5*^{s} phenotype M.R2$^{k/b}$ mice.

Understanding the Genetic Regulation of Acute Viral Infection Induced Tissue Damage Using *Cmv5* Model Mice.

While further assessment of the spleen tissue damage during early MCMV infection will be important in understanding the mechanisms of *Cmv5*^{s}-driven pathology, MCMV is a systemic disease that infects other organs as well. At 4dpi M.R2$^{k/b}$ mice are very sick, but they have not yet reached a humane endpoint, it will be important to determine if damage to other organs presents as the virus is allowed to spread in these mice, or if the damaging interactions are confined to the spleen. I would propose going out to 6dpi (if possible), and

assessing the state of inflammation in organs associated with MCMV pathology in other models, predominantly the liver, lungs, and kidney. The identification of inflammation and macrophage loss as mediators of *Cmv5*^{s}-driven tissue damage during acute MCMV infection suggests that these model mice will likely be susceptible to other viral infections, and depending on the mechanism of action, maybe even other classes of diseases. I would propose testing susceptibility of *Cmv5* model mice to other infectious stimuli (acute viral infection (influenza, LCMV-Armstrong), chronic viral infection (Hepatitis, LCMV-Clone13), intracellular bacterial infection, extracellular bacterial infection, etc. These avenues of exploration have the potential to drastically increase the disease relevance of this model system, and further assessment of required tissue/disease contexts needed for *Cmv5*^{s}-driven susceptibility and tissue damage will also provide *in vivo* mechanistic clues. For example, if *Cmv5*^{s}-driven pathology is confined to the spleen and liver and appears regardless of what kind of infection it is, it may suggest a mechanism involving erythrocytes, etc.

While identification of the genetic mediators is important in obtaining full understanding of *Cmv5*^{s}-driven pathology, medical intervention is unlikely to come at the genetic level, at least with current technology. This makes understanding of how these genetic mediators work to induce tissue pathology through molecular and cellular mediators in various contexts highly translationally relevant. Overall, the *Cmv5* model mice potentially offer widespread relevance to viral infection induced tissue damage outside of MCMV infection in the spleen, and while MCMV is a convenient model to explore these mechanisms, other models and organs should not be ignored as we learn more about *Cmv5*^{s}.

Materials and Methods

Animals. The original *Cmv5*^{s} (MA/My.C57L-H2$^{k/b}$) strain was produced from MA/My x C57L F1 with selective back-crossing to MA/My[150]. We have continued this backcrossing while screening offspring for recombination events using HRM-PCR (described below). Newly generated recombinant mice were then bred to MA/My parent strain, carried and used as the heterozygote (M.H2$^{k/b}$). Experimental groups use littermates and/or non-cohoused mice, as available. Individual experiments with controls are sex matched for either males or females of a similar age. Results have been pooled regardless of age/sex as we did not note significant differences in our phenotypes by these metrics. Experimental mice were bred and maintained in-house at UVA. All mouse experiments were performed in accordance with the Animal Welfare Act and approved by the UVA Animal Care and Use Committee.

***Cmv5*-Recombinant Animal Nomenclature.** All of the newly generated *Cmv5*-recombinant mice were derived from the MA/My.C57L-H2$^{k/b}$ parent strain, and long-form names would be as such: MA/My.C57L-H2$^{k/b}$-RX, where X is the number for the identified recombinant. However, as most recombinants are no longer heterozygous for the entire H2 region (H2$^{k/b}$), we refer to them as being heterozygous for the new recombinant interval more specifically in the format of M.RX$^{k/b}$. C57L-derived interval locations are found in Table I.

Cmv5-Recombinant Mice (GRCm38.p6 Reference Assembly)						
Mouse Strain	Proximal Boundaries[A]		Distal Boundaries		Size Range (Mb) [B]	Total Genes (Polymorphic)[C]
	Outer Limit	Inner Limit	Inner Limit	Outer Limit		
R0	17:30600081	17:32144547	17:50800015	17:53687821	18.65 – 23.08	428 (156)
R2	17:30600081	17:32144547	17:35867500	17:36189450	3.72 – 5.58	206 (89)
R4	17:30600081	17:32144547	17:34189560	17:34381106	2.04 – 3.78	99 (35)
R5	17:32941075	17:33949296	17:34189560	17:34381106	0.24 – 1.44	58 (25)
R6	17:35078174	17:35195079	17:35867500	17:36189450	0.67 – 1.11	63 (33)
R8	17:32367895	17:32941075	17:35867500	17:36189450	2.92 – 3.82	179 (80)

Table I. Genetic Interval Details for *Cmv5*-Recombinant Mice. (A) Chromosome 17 genomic positions for proximal and distal boundaries with outer (MA/My homozygous) and inner (MA/My heterozygous) limits for interval crossovers, including the first identified *Cmv5*^{s} "R0" strain that was further defined herein. **(B)** Interval range values defined but gene-specific PCR amplicons used for genotyping inner and outer limits (See Table II). **(C)** Total gene counts for each interval were determined using the UCSC genome browser[18] for protein coding genes within the associated interval (excluding pseudogenes). Polymorphic gene counts were derived from exome sequencing data[148].

Genotyping by HRM-PCR. DNA was isolated from toe and/or tail clips from pre-weanling pups. PCR was run using the Promega GoTaq® kit (Cat. M3008) reagents, dNTPs purchased from Genesee Scientific (Cat. 42-410), EvaGreen® dye purchased from Biotium (Cat. 31000), and appropriate primers from IDT Technologies. Recombinant offspring were screened using both inner boundary primers designed based on published whole exome sequence data[148] (Table II).

Genotyping Polymorphisms and Primers (GRCm38.p6 Reference Assembly)				
Gene	Polymorphism(s)		Genotyping Primers	
	Type	Location	Forward	Reverse
Glo1	1 SNP	17:30600118	CTGCTATGAAGTTCTCGCTC	CTGCTATGAAGTTCTCGCTC
Notch3	1 SNP	17:32144588	CATTGTGTAGGCACTGAACG	GTGAGATCAATGAGGACGAC
Wiz	1 SNP	17:32367917	CGTCTTGAAGTCAGGAAGCT	CACCCATCAACATCCTGCAA
Cyp4f13	1 SNP	17:32941145	AACACATCTGGGCCATGACT	AGCAATGAAGTTCGGGTGGA
Wdr46	2 SNPs	17:33949336, 17:33949338	CTTGAGCAGCAGCAGCAGAAG	CTAAGGGTCAACTTGGAGAC
Tap1	1 SNP	17:34189492	GCTGGAGTTTGCAAGTGATG	CTGCTGGGTTCTTCAGGAAA
Btnl1	1 SNP	17:34381084	GGACCTGAGAATGATGGGAT	CAACTCAGAGGAGGACAGTA
Ly6g6e	1 SNP	17:35078214	TGAGCAGGACCTATGCAATG	GGCTAGAGGAAGTCATGTAC
Ltb	2 SNPs	17:35195159, 17:35195179	GGCTCAGAAAAGACTGGATG	GAAGCATTGGATCTCTGAGG
Ppp1r18	1 SNP	17:35867446	ATCGCTTGTCCCAGATGCCA	CGATTCTGATGTACTGGTCC
H2-T3	3 SNPs	17:36189362, 17:36189405, 17:36189409	TCTCACACCATCCAGGTGATG	TGCTGCTGTCCACGTTTTCAG
Tbc1d5	1 SNP + 1 IFD	17:50799931, 17:50799955 -50799958	TGTTCAACTGTACCGGCATGC	AAGGCATCATTTGCTGCAGC
Sgo1	2 SNPs	17:53687717, 17:53687723	CACAAAATTCTCTTACTGGG	TTCAAGATACCCTTGAAGAC

Table II. Polymorphisms and Primers used for Genotyping *Cmv5*-Recombinant Mice. Locations of polymorphisms identified by previously published exome sequencing[148] and primers used for HRM-PCR genotyping. *Cmv5*-recombinant mice were genotyped using the inner boundary primers after establishment of both inner and outer boundaries (See Table I).

***In vivo* MCMV Infections.** All infected mice were given $2x10^5$ PFU MCMV intraperitoneally except for specifically labeled Ultra-High Dose (UHD) mice, which were given $6.5x10^5$ PFU. Viral titers were determined using M2-10B4 cells. ***Standard MCMV*:** Smith strain MCMV was purchased from ATCC and passaged through Balb/c weanlings 4-5 times for salivary gland preparations used in experiments. ***MCMV-GFP*:** *M36*-driven Green Fluorescence Protein (GFP) reporter MCMV (MCMV-GFP)[180] was kindly provided by Dr. Zsolt Rusics. MCMV-GFP was passaged twice through Balb/c weanlings for salivary gland preparations used in experiments.

Determination of Viral Load by qPCR. Viral load was determined by spleen DNA qPCR from infected mice at indicated timepoints, normalized to control plasmids as described[190]. PCR was run using the Promega GoTaq® kit (Cat. M3008) reagents, dNTPs purchased from Genesee Scientific (Cat. 42-410), SYBR® Green dye purchased from Invitrogen (Cat. S7563), Fluorescein purchased from BioRad (Cat. 1708780), and primers from IDT Technologies.

Flow Cytometry. ***Antibodies and Reagents:*** CD19 (6D5), CD3 (17A2), H-2D^k (15-5-5), H-2K^k (36-7-5), CD69 (H1.2F3), IFNγ (XMG1.2), KLRG1 (2F1), CD11b (M1/70), CD25 (PC61), TIGIT (1G9), LAG-3 (C9B7W), Eomes (W17001A), Ly6G (1A8), CD68 (FA-11), and F480 (BM8) were purchased from Biolegend; TIM-3 (5D12), CD3e (145-2C11), CD107a (1D4B), and Ly49G2 (4D11) were purchased from BD Biosciences; CD49b (DX5), NK1.1 (PK136), CD11b (M1/70), SIGNR1 (eBio22D1), and LIVE/DEAD™ fixable viability dyes (Cat. L34964 & L34966) were purchased from Invitrogen; CD25 (PC61.5) was purchased from eBioscience. Intracellular staining was performed using BD Biosciences Cytofix/CytoPerm™ kit (Cat. 554714). ***Gating:*** gating and analysis of flow cytometry data was done using FlowJo software version 10.8.1. All data was pre-gated on singlets (FSC-H x FSC-A), cells (FSC-A x SSC-A, debris exclusion), live (viability dye negative), and dump negative (CD3-, CD19-) prior to gating various subsets. *NK cells:* exclusion of SSC++ granulocytes, NK1.1+ or CD49b+. In some cases, further separation of NK cell subsets by expression of Ly49G2 was used for analysis. *Neutrophils:* Ly6G+. *Red Pulp Macrophages:* Ly6G-, CD68+, and F480+. *SIGNR1+ MZMs:* SIGNR1+. ***Cytometer:*** Samples were run on an Invitrogen Attune™ NxT flow cytometer with the Blue/Red/Violet6/Yellow configuration (Cat. A29004).

***In vitro* NK Cell Stimulations.** NK cells were isolated from mechanically dissociated splenocyte suspensions using Miltenyi magnetic NK Cell Isolation Kit (Cat. 130-115-818). NK cells were stimulated for 4 hours at 37°C using plate-bound αNK1.1 (PK136, 10μg/mL), recombinant IL-12p70 (purchased from Peprotech – Cat. 210-12, 5ng/mL) with IL-18 (purchased from Biolegend – Cat. 767002, 50ng/mL), or PMA (purchased from Sigma Cat. 79346, 50ng/mL) and Ionomycin (purchased from Thermo Fisher – Cat. 124222, 1μg/mL). αNK1.1 (PK136, a gift from W. Yokoyama) was produced from hybridoma in-house.

Histology Tissue Preparation and Section Quantification. Spleen sections were fixed at 4°C in 10% methanol-free formaldehyde prior to dehydration, paraffin embedding, slicing, and H&E staining by the UVA Research Histology Core. Stained slides were scanned using an Aperio ScanScope, and individual images were taken at 10x using Aperio ImageScope software version 12.4.3.5008. Images were analyzed using (Fiji Is

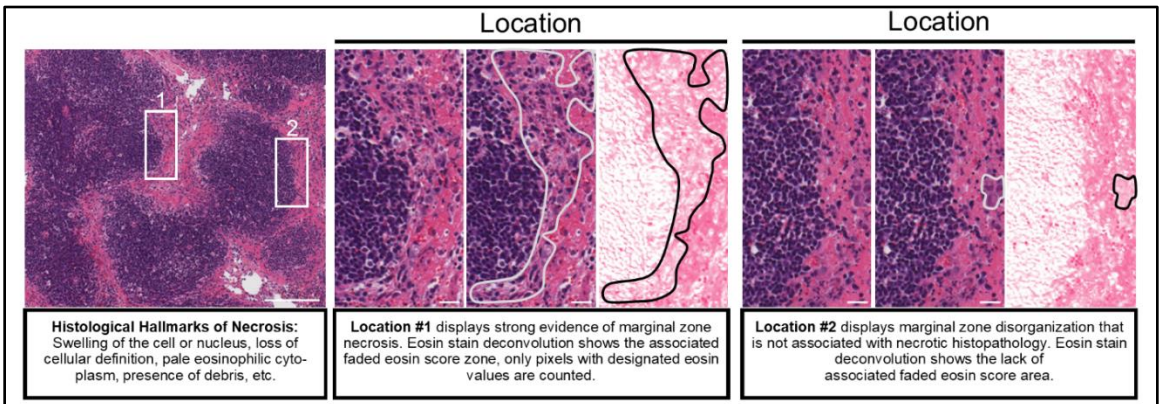

Figure 5.1. Faded Eosin Spleen Histopathology Quantification. 10x H&E-stained tissue section with 2 regions identified. Each identified region (location #1 and #2) is blown up and 3 images are displayed: leftmost image is the raw zoomed in image of the region, middle image contains an outline of area with necrosis-like pathology, and the rightmost image is the ImageJ eosin stain deconvolution with the same outline displaying the lighter eosin staining in these regions. Full image scale bar at 200 microns, insert scale bar at 20 microns.

Just) ImageJ 2.3.0. ***Histology Section Analysis:*** Acellular area and faded eosin score (Fig 5.1) were measured from 10x H&E images. First, images were opened and a

saturation threshold was used to remove non-tissue (whitespace) area. Images were split into channels using color deconvolutions for H&E (Hematoxylin 1 – “BLUE”) and H&E 2 (Hematoxylin 2 – “PURPLE”, Eosin – “PINK”, and Artifacts – “GREEN”). Artifacts were amplified to reduce background, and removed from the deconvoluted images. Next, saturation was measured over the entire area of each deconvoluted channel and settings were calculated for white pulp, faded eosin, and acellular area measurements. These equations are a result of large batch manual trial and error using saturations from different slides and experiments. These calculations are not perfect by any means, but they are consistent, transparent, and pretty good (Table III). Once each image is analyzed, masks of all measured areas are saved.

Histology Section Analysis Definitions		
Measurement		**Determination**

White Pulp Area	WP-Eosin	if (PinkMEAN >= 170) {WPEosin = PinkMED + 40;
		if (WPEosin > 255) {WPEosin = 255;}} else {WPEosin = PinkMED + 10;}
		
		PinkTHRESHOLD (WPEosin, 255), Size >= 3000
		Fill holes, create mask

	WP-Hematoxylin	if (PurpleMED <= 40 && PinkMIN >= 20) {WPHema = PurpleMED;} else if (PurpleMED <= 40) {WPHema = PurpleMED + 5;} else {WPHema = PurpleMED + 10;} PurpleTHRESHOLD (1, WPHema), Size >= 3000 Fill holes, create mask
	WP Mask	WPEosin Mask + WPHema Mask, MEASURE.
Faded Eosin Area		if (PinkMED >= 190) {FEa = 165; FEb = 210;} else if (PinkMED >= 180) {FEa = 165; FEb = 210;} else {FEa = 155; FEb = 200;} PinkTHRESHOLD (FEa, FEb), Size >= 75, MEASURE.
Acellular Area		if (BlueMED > 215) {AC = 254;} else {AC = 234;} BlueTHRESHOLD (AC, 255), Size >=250, MEASURE.

Table III. Histology Section Analysis Definitions. PinkMED = PINK channel median value, PinkMEAN = PINK channel mean value, PinkMIN = PINK channel minimum value, PurpleMED = PURPLE channel median value, and BlueMED = BLUE channel median value.

Data Pooling for *Cmv5* Recombinant Mice. See Figure 5.2. Each independent experiment (left column) contains Cmv5s negative control (M) and positive control (R2)

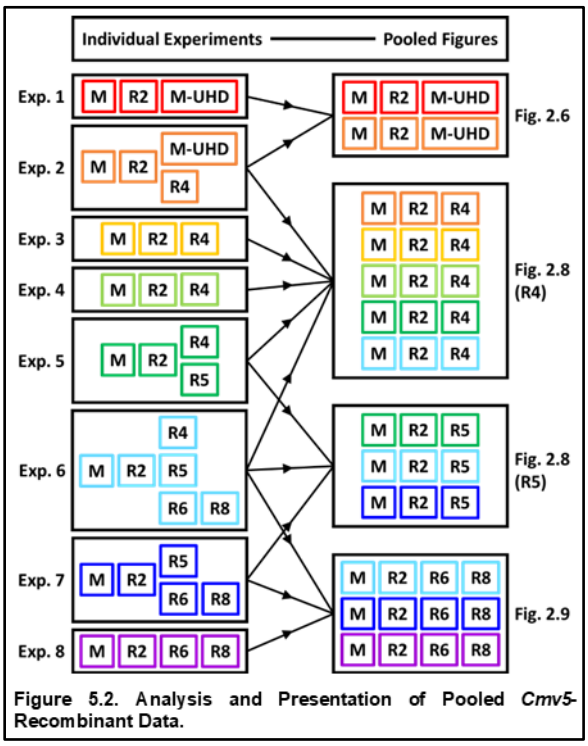

Figure 5.2. Analysis and Presentation of Pooled *Cmv5*-Recombinant Data.

run alongside one or more experimental groups (M-UHD, R4, R5, R6/R8). Each experimental group was paired with the controls from the same experiment (color matching), and pooled with other experiments of the same kind (figures, right column) to assess differences between the control and experimental groups. This approach enables comparative analysis of distinct experimental and control groups (ie. M/R2 vs R4), but does not allow cross-figure statistical comparisons (ie. R4 vs R5), as these two strains were not run together each time.

Immunofluorescent Staining. Spleen tissues were snap frozen using Isopentane and Liquid Nitrogen prior to being cryosectioned by the UVA Research Histology Core. Slides were stored at -80°C or -70°C until fixation in ice cold Methanol at -20°C and blocked using 2% Normal Mouse Serum, 3% BSA, and anti-CD16/32 Fc Block reagent (24G2, produced from hybridoma in-house). When using Biotin/Streptavidin for staining, slides were additionally blocked using Vector Streptavidin/Biotin Blocking Kit (Cat. SP-2002). Primary antibody incubations were done overnight at 4°C, secondary antibody or streptavidin incubations were done for 1 hour at room temperature. After staining and washing, slides were mounted with Invitrogen ProLong™ Gold Antifade Mountant (Cat. P36930) and imaged on a Zeiss Axio Imager M2 widefield fluorescent microscope. ***Antibodies and***

Reagents: Ly6G (1A8), CD3 (17A2), B220 (RA3-6B2), CD169 (3D6.112), F480 (BM8), CD68 (FA-11), Goat anti-Armenian Hamster (Poly4055), Donkey anti-Rabbit (Poly 4064), and conjugated streptavidin were purchased from Biolegend. SIGNR1 (eBio22D1), GFP (Cat. G10362), Goat anti-Armenian Hamster (Cat. A78964), Goat anti-Rabbit (Cat. A21428), and conjugated streptavidin were purchased from Invitrogen. MAdCAM-1 (MECA-367) was purchased from eBioscience, anti-fibroblast (ERTR7) was purchased from Novus Biologicals, 4HNE (Cat. BS-6313R) was purchased from Bioss, and Cleaved Caspase 3 (Asp175, Cat. 9661) was purchased from Cell Signaling Technologies. ***Imaging Analysis and Presentation:*** Images were analyzed using (Fiji Is Just) ImageJ version 2.14.0/1.54f. Scale bars were added to images and adjustments made to brightness and contrast using Zen 2.3.0 (blue edition). Adjustments to brightness and contrast were made uniformly over the entire image.

TUNEL Assay. Formaldehyde fixed and paraffin embedded spleen sections were hydrated and assayed for cell death using the Click-iT™ Plus TUNEL (terminal deoxynucleotidyl transferase dUTP nick end labeling) Assay Kit from Invitrogen (Cat. C10619). After the TUNEL assay, slides were stained for Ly6G (1A8) and imaged as described above.

Multiplex ELISA from Spleen Supernatants. To prepare spleen supernatants, a piece of spleen was weighed, finely minced into a small volume of PBS, and kept on ice until all spleens had been harvested. Once all samples were collected, tubes were spun at 300xg for 10min and supernatant was stored at -80°C or -70°C prior to running the ELISA. Multiplex LEGENDPlex™ ELISAs were purchased from Biolegend either as the pre-defined Mouse Inflammation Panel (Cat. 740446) or mix and match kits for specific

cytokines of interest. Samples were run on an Invitrogen Attune™ NxT flow cytometer and analyzed using FlowJo software. Experiment-to-experiment analyte raw values varied while relative differences between strains were maintained. Pooled data normalized to the MA/My control group for each experiment has been presented.

Neutrophil Depletion. All injections were given intraperitoneally and all in vivo antibodies were purchased from BioXCell. The day prior to MCMV infection (day -1), mice were given 100 µg Rat anti-Ly6G (1A8) or Rat IgG2a, κ Isotype (2A3). On day 0, all mice were given 100 µg Mouse anti-Rat (MAR 18.5) and infected with MCMV. The next day (day 1), mice were given an additional 100 µg anti-Ly6G or isotype injection. Mice were sacrificed and tissue harvested for analysis on day 2, or given an additional 100 µg anti-Ly6G or isotype injection on day 3 prior to harvest on day 4. Regimen adapted for use with our MCMV infection model[179]. Neutrophil depletion was verified by flow cytometry using intracellular Ly6G staining[179], and immunofluorescent imaging of spleen sections.

Macrophage Depletion. Mice were injected with 140 ul clodronate-containing or control liposomes (Encapsula Nanosciences, Cat. CLD-8901) intravenously 1 day prior to MCMV infection. Macrophage depletion was assessed by flow cytometry and immunofluorescent imaging of spleen sections.

Statistical Analysis. Tests used to make statistical comparisons are noted in the figure legends. All statistical analysis was performed using GraphPad Prism software version 10.0.0-10.0.3. Statistical significance is noted in graphs using asterisks * $p < 0.05$, ** $p < 0.01$, *** $p < 0.001$, **** $p < 0.0001$.

Cmv5-Recombinant Interval Genes and RNA Species.

Table IV. *Cmv5*-Recombinant C57L-Derived Region Protein-Coding Genes[18, 148]

Cmv5-Recombinant	Protein Coding Genes	
	Coding Polymorphisms	**No Coding Polymorphisms**
M.R2$^{k/b}$ (R2 Interval)	Dnah8, Rrp1b, Notch3, Ephx3, Brd4, Wiz, Cyp4f15, Zfp811, Zfp799, Cyp4f13, Kifc1, Daxx, Rgl2, Wdr46, Rps18, Vps52, H2-K1, Ring1, H2-Ke6, Slc39a7, Col11a2, H2-Oa, H2-DMa, H2-DMb2, H2-DMb1, Psmb9, Tap1, Psmb8, Tap2, H2-Ob, H2-Ab1, H2-Aa, H2-Eb1, H2-Eb2, Btnl2, Btnl1, BC051142, Btnl4, Btnl6, Notch4, Ager, Fkbpl, Atf6b, Tnxb, C4b, Cyp21a1, Stk19, Nelfe, Cfb, Sapcd1, Msh5, Ly6g6d, Ly6g6e, Ly6g5c, Csnk2b, Gpank1, Apom, Bag6, Prrc2a, Lst1, Ltb, Nfkbil1, H2-D1, H2-Q1, H2-Q2, H2-Q4, H2-Q5, H2-Q6, H2-Q7, Pou5f1, Cchcr1, Cdsn, Emprin, Mucl3, Vars2, Gtf2h4, Ddr1, Mdc1, Ppp1r18, 2310061I04Rik, Atat1, H2-T23, H2-T22, Gm11127, Gm7030, Gm8909.	Glp1r, Umodl1, Abcg1, Tff3, Tff2, Tff1, Tmprss3, Ubash3a, Rsph1, Slc37a1, Pde9a, Wdr4, Ndufv3, Pknox1, Cbs, U2af1, Cryaa, Sik1, Hsf2bp, Akap8, Akap8l, Rasal3, Pglyrp2, Cyp4f39, Cyp4f17, Cyp4f16, Cyp4f37, Cyp4f40, Zfp871, Zfp870, Cyp4f14, Zfp472, Zfp952, Zfp763, Zfp563, Morc2b, Olfr55, Olfr239, Olfr1564, Zfp955a, Olfr63, Zfp955b, Zfp81, Zfp101, Actl9, Gm4125, Adamts10, Myo1f, Zfp414, Pram1, Hnrnpm, Rab11b, Angptl4, Kank3, Rps28, Ndufa7, Cd320, Smim40, Tapbp, Zbtb22, Pfdn6, B3galt4, Rxrb, Brd2, Gpsm3, Pbx2, Rnf5, Agpat1, Egfl8, Ppt2, Prrt1, Dxo, Skiv2l, Gm20547, C2, Zbtb12, Ehmt2, Slc44a4, Neu1, Hspa1b, Hspa1a, Gm20481, Hspa1l, Lsm2, Vars, Vwa7, Clic1, Ddah2, Mpig6b, Ly6g6c, Ly6g6f, Abhd16a, Ly6g5b, D17H6S53E, Aif1, Tnf, Lta, Gm16181, Atp6v1g2, Ddx39b, H2-Q10, Tcf19, Psors1c2, Sfta2, Muc21, Ier3, Flot1, Tubb5, Nrm, Dhx16, Mrps18b, Ppp1r10, Abcf1, Prr3, Gnl1, H2-T24, Gm6034, H2-Bl, H2-T10, Gm19684.
M.R8$^{k/b}$ (R8 Interval)	Cyp4f15, Zfp811, Zfp799, Cyp4f13, Kifc1, Daxx, Rgl2, Wdr46, Rps18, Vps52, H2-K1, Ring1, H2-Ke6, Slc39a7, Col11a2, H2-Oa, H2-DMa, H2-DMb2, H2-DMb1, Psmb9, Tap1, Psmb8, Tap2, H2-Ob, H2-Ab1, H2-Aa, H2-Eb1, H2-Eb2, Btnl2, Btnl1, BC051142, Btnl4, Btnl6, Notch4, Ager, Fkbpl, Atf6b, Tnxb, C4b, Cyp21a1, Stk19, Nelfe, Cfb, Sapcd1, Msh5, Ly6g6d, Ly6g6e, Ly6g5c, Csnk2b, Gpank1, Apom, Bag6, Prrc2a, Lst1, Ltb, Nfkbil1, H2-D1, H2-Q1, H2-Q2, H2-Q4, H2-Q5, H2-Q6, H2-Q7, Pou5f1, Cchcr1, Cdsn, Emprin, Mucl3, Vars2, Gtf2h4, Ddr1, Mdc1, Ppp1r18, 2310061I04Rik, Atat1, H2-T23, H2-T22, Gm11127, Gm7030, Gm8909.	Rasal3, Pglyrp2, Cyp4f39, Cyp4f17, Cyp4f16, Cyp4f37, Cyp4f40, Zfp871, Zfp870, Cyp4f14, Zfp472, Zfp952, Zfp763, Zfp563, Morc2b, Olfr55, Olfr239, Olfr1564, Zfp955a, Olfr63, Zfp955b, Zfp81, Zfp101, Actl9, Gm4125, Adamts10, Myo1f, Zfp414, Pram1, Hnrnpm, Rab11b, Angptl4, Kank3, Rps28, Ndufa7, Cd320, Smim40, Tapbp, Zbtb22, Pfdn6, B3galt4, Rxrb, Brd2, Gpsm3, Pbx2, Rnf5, Agpat1, Egfl8, Ppt2, Prrt1, Dxo, Skiv2l, Gm20547, C2, Zbtb12, Ehmt2, Slc44a4, Neu1, Hspa1b, Hspa1a, Gm20481, Hspa1l, Lsm2, Vars, Vwa7, Clic1, Ddah2, Mpig6b, Ly6g6c, Ly6g6f, Abhd16a, Ly6g5b, D17H6S53E, Aif1, Tnf, Lta, Gm16181, Atp6v1g2, Ddx39b, H2-Q10, Tcf19, Psors1c2, Sfta2, Muc21, Ier3, Flot1, Tubb5, Nrm, Dhx16, Mrps18b, Ppp1r10, Abcf1, Prr3, Gnl1, H2-T24, Gm6034, H2-Bl, H2-T10, Gm19684.
M.R5$^{k/b}$ (R5 Interval)	Kifc1, Daxx, Rgl2, Wdr46, Rps18, Vps52, H2-K1, Ring1, H2-Ke6, Slc39a7, Col11a2, H2-Oa, H2-DMa, H2-DMb2, H2-DMb1, Psmb9, Tap1, Psmb8, Tap2, H2-Ob, H2-Ab1, H2-Aa, H2-Eb1, H2-Eb2, Btnl2.	Zfp472, Zfp952, Zfp763, Zfp563, Morc2b, Olfr55, Olfr239, Olfr1564, Zfp955a, Olfr63, Zfp955b, Zfp81, Zfp101, Actl9, Gm4125, Adamts10, Myo1f, Zfp414, Pram1, Hnrnpm, Rab11b, Angptl4, Kank3, Rps28, Ndufa7, Cd320, Smim40, Tapbp, Zbtb22, Pfdn6, B3galt4, Rxrb, Brd2.
M.R6$^{k/b}$ (R6 Interval)	Ly6g5c, Csnk2b, Gpank1, Apom, Bag6, Prrc2a, Lst1, Ltb, Nfkbil1, H2-D1, H2-Q1, H2-Q2, H2-Q4, H2-Q5, H2-Q6, H2-Q7, Pou5f1, Cchcr1, Cdsn, Emprin, Mucl3, Vars2, Gtf2h4, Ddr1, Mdc1, Ppp1r18, 2310061I04Rik, Atat1, H2-T23, H2-T22, Gm11127, Gm7030, Gm8909.	Ly6g6f, Abhd16a, Ly6g5b, D17H6S53E, Aif1, Tnf, Lta, Gm16181, Atp6v1g2, Ddx39b, H2-Q10, Tcf19, Psors1c2, Sfta2, Muc21, Ier3, Flot1, Tubb5, Nrm, Dhx16, Mrps18b, Ppp1r10, Abcf1, Prr3, Gnl1, H2-T24, Gm6034, H2-Bl, H2-T10, Gm19684.

Table V. *Cmv5*-Recombinant C57L-Derived Region RNA Mediators[18, 148]

Cmv5-Recombinant	lncRNA Genes[a]	miRNAs	Other RNAs
M.R2$^{k/b}$ (R2 Interval)	Gm50252, Glo1, 1700097N02Rik, Dnah8, Dnah8, Dnah8, Gm41561, Dnah8, Gm9937, Gm50242, Gm10503, Gm41562, Gm50249, Gm15318, Gm15318, Gm15318, Gm15318, Gm15318, Gm15318, Ubash3a, Ubash3a, Gm50218, Gm50218, Gm50218, Slc37a1, Slc37a1, Slc37a1, Slc37a1, Slc37a1, Gm9902, Gm50138, Pde9a, Gm50138, Pde9a, Wdr4, Wdr4, Wdr4, Gm50103, Wdr4, Ndufv3, Ndufv3, Gm50105, 4833413E03Rik, 4833413E03Rik, 4833413E03Rik, AC166172.1, Gm50107, Cbs, U2af1, Gm50222, Gm50222, Gm50225, Gm49999, Gm49999, Sik1, Gm50000, 2310015A16Rik, Hsf2bp, Hsf2bp, Hsf2bp, Rrp1b, Rrp1b, Gm17276, Gm17276, Gm17276, Brd4, Gm26549, Akap8, Akap8, Akap8l, Akap8l, Wiz, Wiz, A530088E08Rik, A530088E08Rik, A530088E08Rik, A530088E08Rik, A530088E08Rik, Cyp4f39, Cyp4f17, Cyp4f16, Cyp4f15, Gm50046, Zfp871, Gm17115, Gm26693, Gm50050, Gm50051, Zfp870, Cyp4f13, Zfp952, Zfp763, Morc2b, Olfr63, Zfp955b, Zfp101, Zfp101, Adamts10, Zfp414, Gm20507, Hnrnpm, Hnrnpm, Hnrnpm, Rab11b, Rab11b, Gm17251, Angptl4, 4931413I07Rik, Kank3, Rps28, Ndufa7, Ndufa7, Ndufa7, Ndufa7, Ndufa7, BC051226, BC051226, BC051226, BC051226, Daxx, Daxx, Daxx, Gm19412, Gm19412, Tapbp, Tapbp, Gm50037, Rps18, Rps18, Rps18, Vps52, AA388235, H2-K1, Gm26940, Slc39a7, Col11a2, Col11a2, BC051537, BC051537, Gm50333, Brd2, Brd2, H2-DMa, Brd2, H2-DMa, Brd2, Gm50336, H2-DMa, H2-DMa, Gm50335, H2-DMb1, Gm20496, Gm20496, Tap2, Gm15821, H2-Ob, H2-Ob, H2-Ab1, H2-Aa, Gm20513, Gm20513, BC051142, BC051142, Btnl4, Notch4, Notch4, Notch4, Notch4, Ager, Gm20463, Gm20460, Gm20461, Cyp21a1, C4a, C4a, C4a, C4a, C4a, Stk19, C2, C2, C2, Ehmt2, Ehmt2, 1110038B12Rik, 1110038B12Rik, 1110038B12Rik, Gm10501, Lsm2, Lsm2, Lsm2, Lsm2, Msh5, Ly6g6d, Ly6g6d, Abhd16a, Gpank1, Gm20522, Prrc2a, Gm17705, Aif1, Nfkbil1, Ddx39b, Gm11131, H2-Q5, Gm19553, Cchcr1, Sfta2, Gm9573, Gm20483, Gtf2h4, Gm4577, Gm20443, Gm20442, 4833427F10Rik, Ppp1r18os, 2310061I04Rik, 2310061I04Rik, Gm16279, Atat1, Atat1, Mrps18b, Ppp1r10, Gm20508, A930015D03Rik, BC023719, 2410017I17Rik, 2410017I17Rik, 2410017I17Rik, Gm8909, Gm8909, Gm20478.	Gm24026, Gm24970, Gm22201, Gm27740, Mir219a-1, Mir219c, Gm27471, Mir6971, Mir6970, Mir6972, Mir6973a, Mir6974, Mir6975, Mir8094, Gm28033, Mir1894, Mir877.	Gm24661, Gm25447, Gm23294, Gm25555, Gm22943, Gm23111, Gm24389, Snord52, Gm25744, Gm23421, Gm23442, Gm22589, Gm25128, Gm23864.
M.R8$^{k/b}$ (R8 Interval)	Wiz, Wiz, A530088E08Rik, A530088E08Rik, A530088E08Rik, A530088E08Rik, A530088E08Rik, Cyp4f39, Cyp4f17, Cyp4f16, Cyp4f15, Gm50046, Zfp871, Gm17115, Gm26693, Gm50050, Gm50051, Zfp870, Cyp4f13, Zfp952, Zfp763, Morc2b, Olfr63, Zfp955b, Zfp101, Zfp101, Adamts10, Zfp414, Gm20507, Hnrnpm, Hnrnpm, Hnrnpm, Rab11b, Rab11b, Gm17251, Angptl4, 4931413I07Rik, Kank3, Rps28, Ndufa7, Ndufa7, Ndufa7, Ndufa7, Ndufa7, BC051226, BC051226, BC051226, Daxx, Daxx, Daxx, Gm19412, Gm19412, Tapbp, Tapbp, Gm50037, Rps18, Rps18, Rps18, Vps52, AA388235, H2-K1, Gm26940, Slc39a7, Col11a2, Col11a2, BC051537, BC051537, Gm50333, Brd2, Brd2, H2-DMa, Brd2, H2-DMa, Brd2, Gm50336, H2-DMa, H2-DMa, Gm50335, H2-DMb1, Gm20496, Gm20496, Tap2, Gm15821, H2-Ob, H2-Ob, H2-Ab1, H2-Aa, Gm20513, Gm20513, BC051142, BC051142, Btnl4, Notch4, Notch4, Notch4, Notch4, Ager, Gm20463, Gm20460, Gm20461, Cyp21a1, C4a, C4a, C4a, C4a, C4a, C4a, Stk19, C2, C2, C2, Ehmt2, Ehmt2, 1110038B12Rik, 1110038B12Rik, 1110038B12Rik, Gm10501, Lsm2, Lsm2, Lsm2, Lsm2, Msh5, Ly6g6d, Ly6g6d, Abhd16a, Gpank1, Gm20522, Prrc2a, Gm17705, Aif1, Nfkbil1, Ddx39b, Gm11131, H2-Q5, Gm19553, Cchcr1, Sfta2, Gm9573, Gm20483, Gtf2h4, Gm4577, Gm20443, Gm20442, 4833427F10Rik, Ppp1r18os, 2310061I04Rik, 2310061I04Rik, Gm16279, Atat1, Atat1, Mrps18b, Ppp1r10, Gm20508, A930015D03Rik, BC023719, 2410017I17Rik, 2410017I17Rik, 2410017I17Rik, Gm8909, Gm8909, Gm20478.	Gm22201, Gm27740, Mir219a-1, Mir219c, Gm27471, Mir6971, Mir6970, Mir6972, Mir6973a, Mir6974, Mir6975, Mir8094, Gm28033, Mir1894, Mir877.	Gm23294, Gm25555, Gm22943, Gm23111, Gm24389, Snord52, Gm25744, Gm23421, Gm23442, Gm22589, Gm25128, Gm23864.

M.R5$^{k/b}$ (R5 Interval)	Cyp4f13, Zfp952, Zfp763, Morc2b, Olfr63, Zfp955b, Zfp101, Zfp101, Adamts10, Zfp414, Gm20507, Hnrnpm, Hnrnpm, Hnrnpm, Rab11b, Rab11b, Gm17251, Angptl4, 4931413I07Rik, Kank3, Rps28, Ndufa7, Ndufa7, Ndufa7, Ndufa7, Ndufa7, BC051226, BC051226, BC051226, Daxx, Daxx, Daxx, Gm19412, Gm19412, Tapbp, Tapbp, Gm50037, Rps18, Rps18, Rps18, Vps52, AA388235, H2-K1, Gm26940, Slc39a7, Col11a2, Col11a2, BC051537, BC051537, Gm50333, Brd2, Brd2, H2-DMa, Brd2, H2-DMa, Brd2, Gm50336, H2-DMa, H2-DMa, Gm50335, H2-DMb1, Gm20496, Gm20496, Tap2, Gm15821, H2-Ob, H2-Ob, H2-Ab1, H2-Aa, Gm20513, Gm20513.	Gm27740, Mir219a-1, Mir219c.	Gm25555, Gm22943, Gm23111.
M.R6$^{k/b}$ (R6 Interval)	Abhd16a, Gpank1, Gm20522, Prrc2a, Gm17705, Aif1, Nfkbil1, Ddx39b, Gm11131, H2-Q5, Gm19553, Cchcr1, Sfta2, Gm9573, Gm20483, Gtf2h4, Gm4577, Gm20443, Gm20442, 4833427F10Rik, Ppp1r18os, 2310061I04Rik, 2310061I04Rik, Gm16279, Atat1, Atat1, Mrps18b, Ppp1r10, Gm20508, A930015D03Rik, BC023719, 2410017I17Rik, 2410017I17Rik, 2410017I17Rik, Gm8909, Gm8909, Gm20478.	Mir6973a, Mir6974, Mir6975, Mir8094, Gm28033, Mir1894, Mir877.	Gm23442, Gm22589, Gm25128, Gm23864.

[a] Genes listed more than once have multiple lncRNAs noted within the gene, each counting as a separate lncRNA species.

References

1. J. L. Casanova. 2015. Human genetic basis of interindividual variability in the course of infection. *Proc Natl Acad Sci U S A* 112: E7118-7127.
2. J. L. Casanova. 2015. Severe infectious diseases of childhood as monogenic inborn errors of immunity. *Proc Natl Acad Sci U S A* 112: E7128-7137.
3. C. Klein Herenbrink, D. A. Sykes, P. Donthamsetti, M. Canals, T. Coudrat, J. Shonberg, P. J. Scammells, B. Capuano, P. M. Sexton, S. J. Charlton, J. A. Javitch, A. Christopoulos and J. R. Lane. 2016. The role of kinetic context in apparent biased agonism at GPCRs. *Nat Commun* 7: 10842.
4. C. Thomas, I. Moraga, D. Levin, P. O. Krutzik, Y. Podoplelova, A. Trejo, C. Lee, G. Yarden, S. E. Vleck, J. S. Glenn, G. P. Nolan, J. Piehler, G. Schreiber and K. C. Garcia. 2011. Structural linkage between ligand discrimination and receptor activation by type I interferons. *Cell* 146: 621-632.
5. G. Voisinne, M. Locard-Paulet, C. Froment, E. Maturin, M. G. Menoita, L. Girard, V. Mellado, O. Burlet-Schiltz, B. Malissen, A. Gonzalez de Peredo and R. Roncagalli. 2022. Kinetic proofreading through the multi-step activation of the ZAP70 kinase underlies early T cell ligand discrimination. *Nat Immunol* 23: 1355-1364.
6. D. E. Gordon, J. Hiatt, M. Bouhaddou, V. V. Rezelj, S. Ulferts, H. Braberg, A. S. Jureka, K. Obernier, J. Z. Guo, J. Batra, R. M. Kaake, A. R. Weckstein, T. W. Owens, M. Gupta, S. Pourmal, E. W. Titus, M. Cakir, M. Soucheray, M. McGregor, Z. Cakir, G. Jang, M. J. O'Meara, T. A. Tummino, Z. Zhang, H. Foussard, A. Rojc, Y. Zhou, D. Kuchenov, R. Huttenhain, J. Xu, M. Eckhardt, D. L. Swaney, J. M. Fabius, M. Ummadi, B. Tutuncuoglu, U. Rathore, M. Modak, P. Haas, K. M. Haas, Z. Z. C. Naing, E. H. Pulido, Y. Shi, I. Barrio-Hernandez, D. Memon, E. Petsalaki, A. Dunham, M. C. Marrero, D. Burke, C. Koh, T. Vallet, J. A. Silvas, C. M. Azumaya, C. Billesbolle, A. F. Brilot, M. G. Campbell, A. Diallo, M. S. Dickinson, D. Diwanji, N. Herrera, N. Hoppe, H. T. Kratochvil, Y. Liu, G. E. Merz, M. Moritz, H. C. Nguyen, C. Nowotny, C. Puchades, A. N. Rizo, U. Schulze-Gahmen, A. M. Smith, M. Sun, I. D. Young, J. Zhao, D. Asarnow, J. Biel, A. Bowen, J. R. Braxton, J. Chen, C. M. Chio, U. S. Chio, I. Deshpande, L. Doan, B. Faust, S. Flores, M. Jin, K. Kim, V. L. Lam, F. Li, J. Li, Y. L. Li, Y. Li, X. Liu, M. Lo, K. E. Lopez, A. A. Melo, F. R. Moss, 3rd, P. Nguyen, J. Paulino, K. I. Pawar, J. K. Peters, T. H. Pospiech, Jr., M. Safari,

S. Sangwan, K. Schaefer, P. V. Thomas, A. C. Thwin, R. Trenker, E. Tse, T. K. M. Tsui, F. Wang, N. Whitis, Z. Yu, K. Zhang, Y. Zhang, F. Zhou, D. Saltzberg, Q. S. B. Consortium, A. J. Hodder, A. S. Shun-Shion, D. M. Williams, K. M. White, R. Rosales, T. Kehrer, L. Miorin, E. Moreno, A. H. Patel, S. Rihn, M. M. Khalid, A. Vallejo-Gracia, P. Fozouni, C. R. Simoneau, T. L. Roth, D. Wu, M. A. Karim, M. Ghoussaini, I. Dunham, F. Berardi, S. Weigang, M. Chazal, J. Park, J. Logue, M. McGrath, S. Weston, R. Haupt, C. J. Hastie, M. Elliott, F. Brown, K. A. Burness, E. Reid, M. Dorward, C. Johnson, S. G. Wilkinson, A. Geyer, D. M. Giesel, C. Baillie, S. Raggett, H. Leech, R. Toth, N. Goodman, K. C. Keough, A. L. Lind, C. Zoonomia, R. J. Klesh, K. R. Hemphill, J. Carlson-Stevermer, J. Oki, K. Holden, T. Maures, K. S. Pollard, A. Sali, D. A. Agard, Y. Cheng, J. S. Fraser, A. Frost, N. Jura, T. Kortemme, A. Manglik, D. R. Southworth, R. M. Stroud, D. R. Alessi, P. Davies, M. B. Frieman, T. Ideker, C. Abate, N. Jouvenet, G. Kochs, B. Shoichet, M. Ott, M. Palmarini, K. M. Shokat, A. Garcia-Sastre, J. A. Rassen, R. Grosse, O. S. Rosenberg, K. A. Verba, C. F. Basler, M. Vignuzzi, A. A. Peden, P. Beltrao and N. J. Krogan. 2020. Comparative host-coronavirus protein interaction networks reveal pan-viral disease mechanisms. *Science* 370.

7. S. G. Tangye, W. Al-Herz, A. Bousfiha, C. Cunningham-Rundles, J. L. Franco, S. M. Holland, C. Klein, T. Morio, E. Oksenhendler, C. Picard, A. Puel, J. Puck, M. R. J. Seppanen, R. Somech, H. C. Su, K. E. Sullivan, T. R. Torgerson and I. Meyts. 2022. Human Inborn Errors of Immunity: 2022 Update on the Classification from the International Union of Immunological Societies Expert Committee. *J Clin Immunol* 42: 1473-1507.
8. T. H. Mogensen. 2022. Genetic susceptibility to viral disease in humans. *Clin Microbiol Infect* 28: 1411-1416.
9. M. Similuk and T. Kuijpers. 2023. Nature and nurture: understanding phenotypic variation in inborn errors of immunity. *Front Cell Infect Microbiol* 13: 1183142.
10. J. L. Casanova and L. Abel. 2022. From rare disorders of immunity to common determinants of infection: Following the mechanistic thread. *Cell* 185: 3086-3103.
11. L. Kobrynski, R. W. Powell and S. Bowen. 2014. Prevalence and morbidity of primary immunodeficiency diseases, United States 2001-2007. *J Clin Immunol* 34: 954-961.

12. D. J. M. Crouch and W. F. Bodmer. 2020. Polygenic inheritance, GWAS, polygenic risk scores, and the search for functional variants. *Proc Natl Acad Sci U S A* 117: 18924-18933.

13. Y. Li, M. Oosting, S. P. Smeekens, M. Jaeger, R. Aguirre-Gamboa, K. T. T. Le, P. Deelen, I. Ricano-Ponce, T. Schoffelen, A. F. M. Jansen, M. A. Swertz, S. Withoff, E. van de Vosse, M. van Deuren, F. van de Veerdonk, A. Zhernakova, J. W. M. van der Meer, R. J. Xavier, L. Franke, L. A. B. Joosten, C. Wijmenga, V. Kumar and M. G. Netea. 2016. A Functional Genomics Approach to Understand Variation in Cytokine Production in Humans. *Cell* 167: 1099-1110 e1014.

14. P. Jin and E. Wang. 2003. Polymorphism in clinical immunology - From HLA typing to immunogenetic profiling. *J Transl Med* 1: 8.

15. V. Tam, N. Patel, M. Turcotte, Y. Bosse, G. Pare and D. Meyre. 2019. Benefits and limitations of genome-wide association studies. *Nat Rev Genet* 20: 467-484.

16. A. R. Martin, M. Kanai, Y. Kamatani, Y. Okada, B. M. Neale and M. J. Daly. 2019. Clinical use of current polygenic risk scores may exacerbate health disparities. *Nat Genet* 51: 584-591.

17. S. Nurk, S. Koren, A. Rhie, M. Rautiainen, A. V. Bzikadze, A. Mikheenko, M. R. Vollger, N. Altemose, L. Uralsky, A. Gershman, S. Aganezov, S. J. Hoyt, M. Diekhans, G. A. Logsdon, M. Alonge, S. E. Antonarakis, M. Borchers, G. G. Bouffard, S. Y. Brooks, G. V. Caldas, N. C. Chen, H. Cheng, C. S. Chin, W. Chow, L. G. de Lima, P. C. Dishuck, R. Durbin, T. Dvorkina, I. T. Fiddes, G. Formenti, R. S. Fulton, A. Fungtammasan, E. Garrison, P. G. S. Grady, T. A. Graves-Lindsay, I. M. Hall, N. F. Hansen, G. A. Hartley, M. Haukness, K. Howe, M. W. Hunkapiller, C. Jain, M. Jain, E. D. Jarvis, P. Kerpedjiev, M. Kirsche, M. Kolmogorov, J. Korlach, M. Kremitzki, H. Li, V. V. Maduro, T. Marschall, A. M. McCartney, J. McDaniel, D. E. Miller, J. C. Mullikin, E. W. Myers, N. D. Olson, B. Paten, P. Peluso, P. A. Pevzner, D. Porubsky, T. Potapova, E. I. Rogaev, J. A. Rosenfeld, S. L. Salzberg, V. A. Schneider, F. J. Sedlazeck, K. Shafin, C. J. Shew, A. Shumate, Y. Sims, A. F. A. Smit, D. C. Soto, I. Sović, J. M. Storer, A. Streets, B. A. Sullivan, F. Thibaud-Nissen, J. Torrance, J. Wagner, B. P. Walenz, A. Wenger, J. M. D. Wood, C. Xiao, S. M. Yan, A. C. Young, S. Zarate, U. Surti, R. C. McCoy, M. Y. Dennis, I. A. Alexandrov, J. L. Gerton, R. J. O'Neill, W. Timp, J. M. Zook, M. C. Schatz, E. E.

Eichler, K. H. Miga and A. M. Phillippy. 2022. The complete sequence of a human genome. *Science* 376: 44-53.

18. R. H. Waterston, K. Lindblad-Toh, E. Birney, J. Rogers, J. F. Abril, P. Agarwal, R. Agarwala, R. Ainscough, M. Alexandersson, P. An, S. E. Antonarakis, J. Attwood, R. Baertsch, J. Bailey, K. Barlow, S. Beck, E. Berry, B. Birren, T. Bloom, P. Bork, M. Botcherby, N. Bray, M. R. Brent, D. G. Brown, S. D. Brown, C. Bult, J. Burton, J. Butler, R. D. Campbell, P. Carninci, S. Cawley, F. Chiaromonte, A. T. Chinwalla, D. M. Church, M. Clamp, C. Clee, F. S. Collins, L. L. Cook, R. R. Copley, A. Coulson, O. Couronne, J. Cuff, V. Curwen, T. Cutts, M. Daly, R. David, J. Davies, K. D. Delehaunty, J. Deri, E. T. Dermitzakis, C. Dewey, N. J. Dickens, M. Diekhans, S. Dodge, I. Dubchak, D. M. Dunn, S. R. Eddy, L. Elnitski, R. D. Emes, P. Eswara, E. Eyras, A. Felsenfeld, G. A. Fewell, P. Flicek, K. Foley, W. N. Frankel, L. A. Fulton, R. S. Fulton, T. S. Furey, D. Gage, R. A. Gibbs, G. Glusman, S. Gnerre, N. Goldman, L. Goodstadt, D. Grafham, T. A. Graves, E. D. Green, S. Gregory, R. Guigó, M. Guyer, R. C. Hardison, D. Haussler, Y. Hayashizaki, L. W. Hillier, A. Hinrichs, W. Hlavina, T. Holzer, F. Hsu, A. Hua, T. Hubbard, A. Hunt, I. Jackson, D. B. Jaffe, L. S. Johnson, M. Jones, T. A. Jones, A. Joy, M. Kamal, E. K. Karlsson, D. Karolchik, A. Kasprzyk, J. Kawai, E. Keibler, C. Kells, W. J. Kent, A. Kirby, D. L. Kolbe, I. Korf, R. S. Kucherlapati, E. J. Kulbokas, D. Kulp, T. Landers, J. P. Leger, S. Leonard, I. Letunic, R. Levine, J. Li, M. Li, C. Lloyd, S. Lucas, B. Ma, D. R. Maglott, E. R. Mardis, L. Matthews, E. Mauceli, J. H. Mayer, M. McCarthy, W. R. McCombie, S. McLaren, K. McLay, J. D. McPherson, J. Meldrim, B. Meredith, J. P. Mesirov, W. Miller, T. L. Miner, E. Mongin, K. T. Montgomery, M. Morgan, R. Mott, J. C. Mullikin, D. M. Muzny, W. E. Nash, J. O. Nelson, M. N. Nhan, R. Nicol, Z. Ning, C. Nusbaum, M. J. O'Connor, Y. Okazaki, K. Oliver, E. Overton-Larty, L. Pachter, G. Parra, K. H. Pepin, J. Peterson, P. Pevzner, R. Plumb, C. S. Pohl, A. Poliakov, T. C. Ponce, C. P. Ponting, S. Potter, M. Quail, A. Reymond, B. A. Roe, K. M. Roskin, E. M. Rubin, A. G. Rust, R. Santos, V. Sapojnikov, B. Schultz, J. Schultz, M. S. Schwartz, S. Schwartz, C. Scott, S. Seaman, S. Searle, T. Sharpe, A. Sheridan, R. Shownkeen, S. Sims, J. B. Singer, G. Slater, A. Smit, D. R. Smith, B. Spencer, A. Stabenau, N. Stange-Thomann, C. Sugnet, M. Suyama, G. Tesler, J. Thompson, D. Torrents, E. Trevaskis, J. Tromp, C. Ucla, A. Ureta-Vidal, J. P. Vinson, A. C. Von Niederhausern, C. M. Wade, M. Wall, R. J. Weber, R. B. Weiss,

M. C. Wendl, A. P. West, K. Wetterstrand, R. Wheeler, S. Whelan, J. Wierzbowski, D. Willey, S. Williams, R. K. Wilson, E. Winter, K. C. Worley, D. Wyman, S. Yang, S. P. Yang, E. M. Zdobnov, M. C. Zody and E. S. Lander. 2002. Initial sequencing and comparative analysis of the mouse genome. *Nature* 420: 520-562.

19. A. Kumanovics, T. Takada and K. F. Lindahl. 2003. Genomic organization of the mammalian MHC. *Annu Rev Immunol* 21: 629-657.
20. V. Matzaraki, V. Kumar, C. Wijmenga and A. Zhernakova. 2017. The MHC locus and genetic susceptibility to autoimmune and infectious diseases. *Genome Biol* 18: 76.
21. J. Trowsdale and J. C. Knight. 2013. Major histocompatibility complex genomics and human disease. *Annu Rev Genomics Hum Genet* 14: 301-323.
22. S. Kim, J. Poursine-Laurent, S. M. Truscott, L. Lybarger, Y. J. Song, L. Yang, A. R. French, J. B. Sunwoo, S. Lemieux, T. H. Hansen and W. M. Yokoyama. 2005. Licensing of natural killer cells by host major histocompatibility complex class I molecules. *Nature* 436: 709-713.
23. L. L. Lanier. 2005. NK cell recognition. *Annu Rev Immunol* 23: 225-274.
24. K. Kärre, H. G. Ljunggren, G. Piontek and R. Kiessling. 1986. Selective rejection of H-2-deficient lymphoma variants suggests alternative immune defence strategy. *Nature* 319: 675-678.
25. L. J. Berg, A. M. Pullen, B. Fazekas de St Groth, D. Mathis, C. Benoist and M. M. Davis. 1989. Antigen/MHC-specific T cells are preferentially exported from the thymus in the presence of their MHC ligand. *Cell* 58: 1035-1046.
26. N. L. La Gruta, S. Gras, S. R. Daley, P. G. Thomas and J. Rossjohn. 2018. Understanding the drivers of MHC restriction of T cell receptors. *Nat Rev Immunol* 18: 467-478.
27. R. M. Zinkernagel and P. C. Doherty. 1974. Restriction of in vitro T cell-mediated cytotoxicity in lymphocytic choriomeningitis within a syngeneic or semiallogeneic system. *Nature* 248: 701-702.
28. J. Neefjes, M. L. Jongsma, P. Paul and O. Bakke. 2011. Towards a systems understanding of MHC class I and MHC class II antigen presentation. *Nat Rev Immunol* 11: 823-836.

29. P. J. Bjorkman and P. Parham. 1990. STRUCTURE, FUNCTION, AND DIVERSITY OF CLASS I MAJOR HISTOCOMPATIBILITY COMPLEX MOLECULES. *Annual Review of Biochemistry* 59: 253-288.
30. P. Parham, C. E. Lomen, D. A. Lawlor, J. P. Ways, N. Holmes, H. L. Coppin, R. D. Salter, A. M. Wan and P. D. Ennis. 1988. Nature of polymorphism in HLA-A, -B, and -C molecules. *Proceedings of the National Academy of Sciences* 85: 4005-4009.
31. M. P. Martin and M. Carrington. 2005. Immunogenetics of viral infections. *Curr Opin Immunol* 17: 510-516.
32. A. E. Kennedy, U. Ozbek and M. T. Dorak. 2017. What has GWAS done for HLA and disease associations? *Int J Immunogenet* 44: 195-211.
33. W. M. Howell. 2014. HLA and disease: guilt by association. *Int J Immunogenet* 41: 1-12.
34. K. E. Noll, M. T. Ferris and M. T. Heise. 2019. The Collaborative Cross: A Systems Genetics Resource for Studying Host-Pathogen Interactions. *Cell Host Microbe* 25: 484-498.
35. S. M. Vidal, D. Malo, J. F. Marquis and P. Gros. 2008. Forward genetic dissection of immunity to infection in the mouse. *Annu Rev Immunol* 26: 81-132.
36. R. Karki and T. D. Kanneganti. 2021. The 'cytokine storm': molecular mechanisms and therapeutic prospects. *Trends Immunol* 42: 681-705.
37. G. L. Lin, J. P. McGinley, S. B. Drysdale and A. J. Pollard. 2018. Epidemiology and Immune Pathogenesis of Viral Sepsis. *Front Immunol* 9: 2147.
38. M. Hirschenberger, V. Hunszinger and K. M. J. Sparrer. 2021. Implications of Innate Immunity in Post-Acute Sequelae of Non-Persistent Viral Infections. *Cells* 10.
39. B. Sundaresan, F. Shirafkan, K. Ripperger and K. Rattay. 2023. The Role of Viral Infections in the Onset of Autoimmune Diseases. *Viruses* 15.
40. M. A. Ruffner, K. E. Sullivan and S. E. Henrickson. 2017. Recurrent and Sustained Viral Infections in Primary Immunodeficiencies. *Front Immunol* 8: 665.
41. L. K. Dropulic and J. I. Cohen. 2011. Severe viral infections and primary immunodeficiencies. *Clin Infect Dis* 53: 897-909.

42. A. Apelbaum, G. Yarden, S. Warszawski, D. Harari and G. Schreiber. 2013. Type I interferons induce apoptosis by balancing cFLIP and caspase-8 independent of death ligands. *Mol Cell Biol* 33: 800-814.

43. Y. A. Mebratu, B. F. Dickey, C. Evans and Y. Tesfaigzi. 2008. The BH3-only protein Bik/Blk/Nbk inhibits nuclear translocation of activated ERK1/2 to mediate IFNgamma-induced cell death. *J Cell Biol* 183: 429-439.

44. G. N. Barber. 2000. The interferons and cell death: guardians of the cell or accomplices of apoptosis? *Semin Cancer Biol* 10: 103-111.

45. D.-W. Zhang, J. Shao, J. Lin, N. Zhang, B.-J. Lu, S.-C. Lin, M.-Q. Dong and J. Han. 2009. RIP3, an Energy Metabolism Regulator That Switches TNF-Induced Cell Death from Apoptosis to Necrosis. *Science* 325: 332-336.

46. O. Micheau and J. Tschopp. 2003. Induction of TNF receptor I-mediated apoptosis via two sequential signaling complexes. *Cell* 114: 181-190.

47. G. van Loo and M. J. M. Bertrand. 2023. Death by TNF: a road to inflammation. *Nat Rev Immunol* 23: 289-303.

48. S. Bin, L. Xin, Z. Lin, Z. Jinhua, G. Rui and Z. Xiang. 2021. Targeting miR-10a-5p/IL-6R axis for reducing IL-6-induced cartilage cell ferroptosis. *Exp Mol Pathol* 118: 104570.

49. Y. P. Moodley, N. L. A. Misso, A. K. Scaffidi, M. Fogel-Petrovic, R. J. McAnulty, G. J. Laurent, P. J. Thompson and D. A. Knight. 2003. Inverse Effects of Interleukin-6 on Apoptosis of Fibroblasts from Pulmonary Fibrosis and Normal Lungs. *American Journal of Respiratory Cell and Molecular Biology* 29: 490-498.

50. G. Gdynia, M. Keith, J. Kopitz, M. Bergmann, A. Fassl, A. N. Weber, J. George, T. Kees, H. W. Zentgraf, O. D. Wiestler, P. Schirmacher and W. Roth. 2010. Danger signaling protein HMGB1 induces a distinct form of cell death accompanied by formation of giant mitochondria. *Cancer Res* 70: 8558-8568.

51. F. Ye, W. Chai, M. Xie, M. Yang, Y. Yu, L. Cao and L. Yang. 2019. HMGB1 regulates erastin-induced ferroptosis via RAS-JNK/p38 signaling in HL-60/NRAS(Q61L) cells. *Am J Cancer Res* 9: 730-739.

52. J. Xu, X. Zhang, R. Pelayo, M. Monestier, C. T. Ammollo, F. Semeraro, F. B. Taylor, N. L. Esmon, F. Lupu and C. T. Esmon. 2009. Extracellular histones are major mediators of death in sepsis. *Nat Med* 15: 1318-1321.

53. L. M. Zheng, A. Zychlinsky, C. C. Liu, D. M. Ojcius and J. D. Young. 1991. Extracellular ATP as a trigger for apoptosis or programmed cell death. *Journal of Cell Biology* 112: 279-288.

54. H. Sies, C. Berndt and D. P. Jones. 2017. Oxidative Stress. *Annu Rev Biochem* 86: 715-748.

55. L. Galluzzi, I. Vitale, S. A. Aaronson, J. M. Abrams, D. Adam, P. Agostinis, E. S. Alnemri, L. Altucci, I. Amelio, D. W. Andrews, M. Annicchiarico-Petruzzelli, A. V. Antonov, E. Arama, E. H. Baehrecke, N. A. Barlev, N. G. Bazan, F. Bernassola, M. J. M. Bertrand, K. Bianchi, M. V. Blagosklonny, K. Blomgren, C. Borner, P. Boya, C. Brenner, M. Campanella, E. Candi, D. Carmona-Gutierrez, F. Cecconi, F. K. Chan, N. S. Chandel, E. H. Cheng, J. E. Chipuk, J. A. Cidlowski, A. Ciechanover, G. M. Cohen, M. Conrad, J. R. Cubillos-Ruiz, P. E. Czabotar, V. D'Angiolella, T. M. Dawson, V. L. Dawson, V. De Laurenzi, R. De Maria, K. M. Debatin, R. J. DeBerardinis, M. Deshmukh, N. Di Daniele, F. Di Virgilio, V. M. Dixit, S. J. Dixon, C. S. Duckett, B. D. Dynlacht, W. S. El-Deiry, J. W. Elrod, G. M. Fimia, S. Fulda, A. J. Garcia-Saez, A. D. Garg, C. Garrido, E. Gavathiotis, P. Golstein, E. Gottlieb, D. R. Green, L. A. Greene, H. Gronemeyer, A. Gross, G. Hajnoczky, J. M. Hardwick, I. S. Harris, M. O. Hengartner, C. Hetz, H. Ichijo, M. Jaattela, B. Joseph, P. J. Jost, P. P. Juin, W. J. Kaiser, M. Karin, T. Kaufmann, O. Kepp, A. Kimchi, R. N. Kitsis, D. J. Klionsky, R. A. Knight, S. Kumar, S. W. Lee, J. J. Lemasters, B. Levine, A. Linkermann, S. A. Lipton, R. A. Lockshin, C. Lopez-Otin, S. W. Lowe, T. Luedde, E. Lugli, M. MacFarlane, F. Madeo, M. Malewicz, W. Malorni, G. Manic, J. C. Marine, S. J. Martin, J. C. Martinou, J. P. Medema, P. Mehlen, P. Meier, S. Melino, E. A. Miao, J. D. Molkentin, U. M. Moll, C. Munoz-Pinedo, S. Nagata, G. Nunez, A. Oberst, M. Oren, M. Overholtzer, M. Pagano, T. Panaretakis, M. Pasparakis, J. M. Penninger, D. M. Pereira, S. Pervaiz, M. E. Peter, M. Piacentini, P. Pinton, J. H. M. Prehn, H. Puthalakath, G. A. Rabinovich, M. Rehm, R. Rizzuto, C. M. P. Rodrigues, D. C. Rubinsztein, T. Rudel, K. M. Ryan, E. Sayan, L. Scorrano, F. Shao, Y. Shi, J. Silke, H. U. Simon, A. Sistigu, B. R. Stockwell, A. Strasser, G. Szabadkai, S. W. G. Tait, D. Tang, N. Tavernarakis, A. Thorburn, Y. Tsujimoto, B. Turk, T. Vanden Berghe, P. Vandenabeele, M. G. Vander Heiden, A. Villunger, H. W. Virgin, K. H. Vousden, D. Vucic, E. F. Wagner, H. Walczak, D. Wallach, Y. Wang, J. A. Wells, W. Wood, J. Yuan, Z. Zakeri, B. Zhivotovsky, L. Zitvogel, G. Melino and G. Kroemer.

2018. Molecular mechanisms of cell death: recommendations of the Nomenclature Committee on Cell Death 2018. *Cell Death Differ* 25: 486-541.

56. F. C. Fang. 2004. Antimicrobial reactive oxygen and nitrogen species: concepts and controversies. *Nat Rev Microbiol* 2: 820-832.
57. M. Herb and M. Schramm. 2021. Functions of ROS in Macrophages and Antimicrobial Immunity. *Antioxidants (Basel)* 10.
58. G. Lominadze, D. W. Powell, G. C. Luerman, A. J. Link, R. A. Ward and K. R. McLeish. 2005. Proteomic analysis of human neutrophil granules. *Mol Cell Proteomics* 4: 1503-1521.
59. T. N. Mayadas, X. Cullere and C. A. Lowell. 2014. The multifaceted functions of neutrophils. *Annu Rev Pathol* 9: 181-218.
60. V. Brinkmann, U. Reichard, C. Goosmann, B. Fauler, Y. Uhlemann, D. S. Weiss, Y. Weinrauch and A. Zychlinsky. 2004. Neutrophil Extracellular Traps Kill Bacteria. *Science* 303: 1532-1535.
61. C. Silvestre-Roig, Q. Braster, K. Wichapong, E. Y. Lee, J. M. Teulon, N. Berrebeh, J. Winter, J. M. Adrover, G. S. Santos, A. Froese, P. Lemnitzer, A. Ortega-Gomez, R. Chevre, J. Marschner, A. Schumski, C. Winter, L. Perez-Olivares, C. Pan, N. Paulin, T. Schoufour, H. Hartwig, S. Gonzalez-Ramos, F. Kamp, R. T. A. Megens, K. A. Mowen, M. Gunzer, L. Maegdefessel, T. Hackeng, E. Lutgens, M. Daemen, J. von Blume, H. J. Anders, V. O. Nikolaev, J. L. Pellequer, C. Weber, A. Hidalgo, G. A. F. Nicolaes, G. C. L. Wong and O. Soehnlein. 2019. Externalized histone H4 orchestrates chronic inflammation by inducing lytic cell death. *Nature* 569: 236-240.
62. C. M. S. Silva, C. W. S. Wanderley, F. P. Veras, F. Sonego, D. C. Nascimento, A. V. Gonçalves, T. V. Martins, D. F. Cólon, V. F. Borges, V. S. Brauer, L. E. A. Damasceno, K. P. Silva, J. E. Toller-Kawahisa, S. S. Batah, A. L. J. Souza, V. S. Monteiro, A. E. R. Oliveira, P. B. Donate, D. Zoppi, M. C. Borges, F. Almeida, H. I. Nakaya, A. T. Fabro, T. M. Cunha, J. C. Alves-Filho, D. S. Zamboni and F. Q. Cunha. 2021. Gasdermin D inhibition prevents multiple organ dysfunction during sepsis by blocking NET formation. *Blood* 138: 2702-2713.
63. C. W. Ong, P. T. Elkington, S. Brilha, C. Ugarte-Gil, M. T. Tome-Esteban, L. B. Tezera, P. J. Pabisiak, R. C. Moores, T. Sathyamoorthy, V. Patel, R. H. Gilman, J. C. Porter and J. S. Friedland. 2015. Neutrophil-Derived MMP-8 Drives AMPK-

Dependent Matrix Destruction in Human Pulmonary Tuberculosis. *PLoS Pathog* 11: e1004917.

64. F. Denorme, I. Portier, J. L. Rustad, M. J. Cody, C. V. de Araujo, C. Hoki, M. D. Alexander, R. Grandhi, M. R. Dyer, M. D. Neal, J. J. Majersik, C. C. Yost and R. A. Campbell. 2022. Neutrophil extracellular traps regulate ischemic stroke brain injury. *J Clin Invest* 132.
65. S. Rawat, S. Vrati and A. Banerjee. 2021. Neutrophils at the crossroads of acute viral infections and severity. *Mol Aspects Med* 81: 100996.
66. A. Aroca-Crevillen, T. Vicanolo, S. Ovadia and A. Hidalgo. 2024. Neutrophils in Physiology and Pathology. *Annu Rev Pathol* 19: 227-259.
67. J. L. Forbester and I. R. Humphreys. 2021. Genetic influences on viral-induced cytokine responses in the lung. *Mucosal Immunol* 14: 14-25.
68. J.-L. Casanova and L. Abel. 2021. Mechanisms of viral inflammation and disease in humans. *Science* 374: 1080-1086.
69. P. Wong and E. G. Pamer. 2003. CD8 T cell responses to infectious pathogens. *Annu Rev Immunol* 21: 29-70.
70. N. K. Bjorkstrom, B. Strunz and H. G. Ljunggren. 2022. Natural killer cells in antiviral immunity. *Nat Rev Immunol* 22: 112-123.
71. K. S. Tuano, N. Seth and J. Chinen. 2021. Secondary immunodeficiencies: An overview. *Ann Allergy Asthma Immunol* 127: 617-626.
72. E. O. Long, H. S. Kim, D. Liu, M. E. Peterson and S. Rajagopalan. 2013. Controlling natural killer cell responses: integration of signals for activation and inhibition. *Annu Rev Immunol* 31: 227-258.
73. I. Prager and C. Watzl. 2019. Mechanisms of natural killer cell-mediated cellular cytotoxicity. *J Leukoc Biol* 105: 1319-1329.
74. N. Kayagaki, N. Yamaguchi, M. Nakayama, K. Takeda, H. Akiba, H. Tsutsui, H. Okamura, K. Nakanishi, K. Okumura and H. Yagita. 1999. Expression and Function of TNF-Related Apoptosis-Inducing Ligand on Murine Activated NK Cells1. *The Journal of Immunology* 163: 1906-1913.
75. Y. Oshimi, S. Oda, Y. Honda, S. Nagata and S. Miyazaki. 1996. Involvement of Fas ligand and Fas-mediated pathway in the cytotoxicity of human natural killer cells. *The Journal of Immunology* 157: 2909-2915.

76. J. A. Lopez, O. Susanto, M. R. Jenkins, N. Lukoyanova, V. R. Sutton, R. H. Law, A. Johnston, C. H. Bird, P. I. Bird, J. C. Whisstock, J. A. Trapani, H. R. Saibil and I. Voskoboinik. 2013. Perforin forms transient pores on the target cell plasma membrane to facilitate rapid access of granzymes during killer cell attack. *Blood* 121: 2659-2668.

77. L. Shi, R. P. Kraut, R. Aebersold and A. H. Greenberg. 1992. A natural killer cell granule protein that induces DNA fragmentation and apoptosis. *Journal of Experimental Medicine* 175: 553-566.

78. E. Reefman, J. G. Kay, S. M. Wood, C. Offenhauser, D. L. Brown, S. Roy, A. C. Stanley, P. C. Low, A. P. Manderson and J. L. Stow. 2010. Cytokine secretion is distinct from secretion of cytotoxic granules in NK cells. *J Immunol* 184: 4852-4862.

79. C. Fauriat, E. O. Long, H. G. Ljunggren and Y. T. Bryceson. 2010. Regulation of human NK-cell cytokine and chemokine production by target cell recognition. *Blood* 115: 2167-2176.

80. S. N. Waggoner, S. D. Reighard, I. E. Gyurova, S. A. Cranert, S. E. Mahl, E. P. Karmele, J. P. McNally, M. T. Moran, T. R. Brooks, F. Yaqoob and C. E. Rydyznski. 2016. Roles of natural killer cells in antiviral immunity. *Curr Opin Virol* 16: 15-23.

81. J. S. Orange. 2013. Natural killer cell deficiency. *J Allergy Clin Immunol* 132: 515-525.

82. G. M. Konjevic, A. M. Vuletic, K. M. Mirjacic Martinovic, A. K. Larsen and V. B. Jurisic. 2019. The role of cytokines in the regulation of NK cells in the tumor environment. *Cytokine* 117: 30-40.

83. L. Muller, P. Aigner and D. Stoiber. 2017. Type I Interferons and Natural Killer Cell Regulation in Cancer. *Front Immunol* 8: 304.

84. J. R. Ortaldo, A. Mantovani, D. Hobbs, M. Rubinstein, S. Pestka and R. B. Herberman. 1983. Effects of several species of human leukocyte interferon on cytotoxic activity of NK cells and monocytes. *Int J Cancer* 31: 285-289.

85. M. Tomura, X.-Y. Zhou, S. Maruo, H.-J. Ahn, T. Hamaoka, H. Okamura, K. Nakanishi, T. Tanimoto, M. Kurimoto and H. Fujiwara. 1998. A Critical Role for IL-18 in the Proliferation and Activation of NK1.1+CD3− Cells1. *The Journal of Immunology* 160: 4738-4746.

86. E. Marcenaro, M. Della Chiesa, F. Bellora, S. Parolini, R. Millo, L. Moretta and A. Moretta. 2005. IL-12 or IL-4 prime human NK cells to mediate functionally divergent interactions with dendritic cells or tumors. *J Immunol* 174: 3992-3998.

87. L. Cifaldi, G. Prencipe, I. Caiello, C. Bracaglia, F. Locatelli, F. De Benedetti and R. Strippoli. 2015. Inhibition of natural killer cell cytotoxicity by interleukin-6: implications for the pathogenesis of macrophage activation syndrome. *Arthritis Rheumatol* 67: 3037-3046.

88. S. Viel, A. Marçais, F. S. Guimaraes, R. Loftus, J. Rabilloud, M. Grau, S. Degouve, S. Djebali, A. Sanlaville, E. Charrier, J. Bienvenu, J. C. Marie, C. Caux, J. Marvel, L. Town, N. D. Huntington, L. Bartholin, D. Finlay, M. J. Smyth and T. Walzer. 2016. TGF-β inhibits the activation and functions of NK cells by repressing the mTOR pathway. *Sci Signal* 9: ra19.

89. S. Gasser, S. Orsulic, E. J. Brown and D. H. Raulet. 2005. The DNA damage pathway regulates innate immune system ligands of the NKG2D receptor. *Nature* 436: 1186-1190.

90. R. Gastpar, C. Gross, L. Rossbacher, J. Ellwart, J. Riegger and G. Multhoff. 2004. The cell surface-localized heat shock protein 70 epitope TKD induces migration and cytolytic activity selectively in human NK cells. *J Immunol* 172: 972-980.

91. S. Hosomi, J. Grootjans, M. Tschurtschenthaler, N. Krupka, J. D. Matute, M. B. Flak, E. Martinez-Naves, M. Gomez Del Moral, J. N. Glickman, M. Ohira, L. L. Lanier, A. Kaser and R. Blumberg. 2017. Intestinal epithelial cell endoplasmic reticulum stress promotes MULT1 up-regulation and NKG2D-mediated inflammation. *J Exp Med* 214: 2985-2997.

92. L. L. Lanier. 2015. NKG2D Receptor and Its Ligands in Host Defense. *Cancer Immunol Res* 3: 575-582.

93. E. Pogge von Strandmann, V. R. Simhadri, B. von Tresckow, S. Sasse, K. S. Reiners, H. P. Hansen, A. Rothe, B. Boll, V. L. Simhadri, P. Borchmann, P. J. McKinnon, M. Hallek and A. Engert. 2007. Human leukocyte antigen-B-associated transcript 3 is released from tumor cells and engages the NKp30 receptor on natural killer cells. *Immunity* 27: 965-974.

94. C. L. Fuller, G. Ruthel, K. L. Warfield, D. L. Swenson, C. M. Bosio, M. J. Aman and S. Bavari. 2007. NKp30-dependent cytolysis of filovirus-infected human dendritic cells. *Cell Microbiol* 9: 962-976.

95. O. Hershkovitz, B. Rosental, L. A. Rosenberg, M. E. Navarro-Sanchez, S. Jivov, A. Zilka, O. Gershoni-Yahalom, E. Brient-Litzler, H. Bedouelle, J. W. Ho, K. S. Campbell, B. Rager-Zisman, P. Despres and A. Porgador. 2009. NKp44 receptor mediates interaction of the envelope glycoproteins from the West Nile and dengue viruses with NK cells. *J Immunol* 183: 2610-2621.

96. M. Jarahian, M. Fiedler, A. Cohnen, D. Djandji, G. J. Hammerling, C. Gati, A. Cerwenka, P. C. Turner, R. W. Moyer, C. Watzl, H. Hengel and F. Momburg. 2011. Modulation of NKp30- and NKp46-mediated natural killer cell responses by poxviral hemagglutinin. *PLoS Pathog* 7: e1002195.

97. O. Mandelboim, N. Lieberman, M. Lev, L. Paul, T. I. Arnon, Y. Bushkin, D. M. Davis, J. L. Strominger, J. W. Yewdell and A. Porgador. 2001. Recognition of haemagglutinins on virus-infected cells by NKp46 activates lysis by human NK cells. *Nature* 409: 1055-1060.

98. F. M. Karlhofer, R. K. Ribaudo and W. M. Yokoyama. 1992. MHC class I alloantigen specificity of Ly-49+ IL-2-activated natural killer cells. *Nature* 358: 66-70.

99. N. Wagtmann, R. Biassoni, C. Cantoni, S. Verdiani, M. S. Malnati, M. Vitale, C. Bottino, L. Moretta, A. Moretta and E. O. Long. 1995. Molecular clones of the p58 NK cell receptor reveal immunoglobulin-related molecules with diversity in both the extra-and intracellular domains. *Immunity* 2: 439-449.

100. A. C. Anderson, N. Joller and V. K. Kuchroo. 2016. Lag-3, Tim-3, and TIGIT: Co-inhibitory Receptors with Specialized Functions in Immune Regulation. *Immunity* 44: 989-1004.

101. I. P. da Silva, A. Gallois, S. Jimenez-Baranda, S. Khan, A. C. Anderson, V. K. Kuchroo, I. Osman and N. Bhardwaj. 2014. Reversal of NK-cell exhaustion in advanced melanoma by Tim-3 blockade. *Cancer Immunol Res* 2: 410-422.

102. L. C. Ndhlovu, S. Lopez-Verges, J. D. Barbour, R. B. Jones, A. R. Jha, B. R. Long, E. C. Schoeffler, T. Fujita, D. F. Nixon and L. L. Lanier. 2012. Tim-3 marks human natural killer cell maturation and suppresses cell-mediated cytotoxicity. *Blood* 119: 3734-3743.

103. Y. Wolf, A. C. Anderson and V. K. Kuchroo. 2020. TIM3 comes of age as an inhibitory receptor. *Nat Rev Immunol* 20: 173-185.

104. M. Li, P. Xia, Y. Du, S. Liu, G. Huang, J. Chen, H. Zhang, N. Hou, X. Cheng, L. Zhou, P. Li, X. Yang and Z. Fan. 2014. T-cell immunoglobulin and ITIM domain

(TIGIT) receptor/poliovirus receptor (PVR) ligand engagement suppresses interferon-gamma production of natural killer cells via beta-arrestin 2-mediated negative signaling. *J Biol Chem* 289: 17647-17657.

105. S. Liu, H. Zhang, M. Li, D. Hu, C. Li, B. Ge, B. Jin and Z. Fan. 2013. Recruitment of Grb2 and SHIP1 by the ITT-like motif of TIGIT suppresses granule polarization and cytotoxicity of NK cells. *Cell Death Differ* 20: 456-464.
106. S. Narayanan, P. J. Ahl, V. A. Bijin, N. Kaliaperumal, S. G. Lim, C.-I. Wang, A.-M. Fairhurst and J. E. Connolly. 2020. LAG3 is a Central Regulator of NK Cell Cytokine Production. *bioRxiv*: 2020.2001.2031.928200.
107. I. Ohs, L. Ducimetiere, J. Marinho, P. Kulig, B. Becher and S. Tugues. 2017. Restoration of Natural Killer Cell Antimetastatic Activity by IL12 and Checkpoint Blockade. *Cancer Res* 77: 7059-7071.
108. A. Kubota, S. Kubota, S. Lohwasser, D. L. Mager and F. Takei. 1999. Diversity of NK Cell Receptor Repertoire in Adult and Neonatal Mice. *The Journal of Immunology* 163: 212-216.
109. M. G. Brown, A. A. Scalzo, L. R. Stone, P. Y. Clark, Y. Du, B. Palanca and W. M. Yokoyama. 2001. Natural killer gene complex (Nkc) allelic variability in inbred mice: evidence for Nkc haplotypes. *Immunogenetics* 53: 584-591.
110. J. M. Cronk, K. H. Dziewulska, P. Puchalski, R. B. Crittenden, M. L. Hammarskjold and M. G. Brown. 2022. Altered-Self MHC Class I Sensing via Functionally Disparate Paired NK Cell Receptors Counters Murine Cytomegalovirus gp34-Mediated Immune Evasion. *J Immunol* 209: 1545-1554.
111. G. Alter, M. P. Martin, N. Teigen, W. H. Carr, T. J. Suscovich, A. Schneidewind, H. Streeck, M. Waring, A. Meier, C. Brander, J. D. Lifson, T. M. Allen, M. Carrington and M. Altfeld. 2007. Differential natural killer cell-mediated inhibition of HIV-1 replication based on distinct KIR/HLA subtypes. *J Exp Med* 204: 3027-3036.
112. M. P. Martin, X. Gao, J. H. Lee, G. W. Nelson, R. Detels, J. J. Goedert, S. Buchbinder, K. Hoots, D. Vlahov, J. Trowsdale, M. Wilson, S. J. O'Brien and M. Carrington. 2002. Epistatic interaction between KIR3DS1 and HLA-B delays the progression to AIDS. *Nat Genet* 31: 429-434.
113. X. Gao, Y. Jiao, L. Wang, X. Liu, W. Sun, B. Cui, Z. Chen and Y. Zhao. 2010. Inhibitory KIR and specific HLA-C gene combinations confer susceptibility to or protection against chronic hepatitis B. *Clin Immunol* 137: 139-146.

114. S. I. Khakoo, C. L. Thio, M. P. Martin, C. R. Brooks, X. Gao, J. Astemborski, J. Cheng, J. J. Goedert, D. Vlahov, M. Hilgartner, S. Cox, A. M. Little, G. J. Alexander, M. E. Cramp, S. J. O'Brien, W. M. Rosenberg, D. L. Thomas and M. Carrington. 2004. HLA and NK cell inhibitory receptor genes in resolving hepatitis C virus infection. *Science* 305: 872-874.

115. M. M. Naiyer, S. A. Cassidy, A. Magri, V. Cowton, K. Chen, S. Mansour, H. Kranidioti, B. Mbiribindi, P. Rettman, S. Harris, L. J. Fanning, A. Mulder, F. H. J. Claas, A. D. Davidson, A. H. Patel, M. A. Purbhoo and S. I. Khakoo. 2017. KIR2DS2 recognizes conserved peptides derived from viral helicases in the context of HLA-C. *Science Immunology* 2: eaal5296.

116. M. Carrington, S. Wang, M. P. Martin, X. Gao, M. Schiffman, J. Cheng, R. Herrero, A. C. Rodriguez, R. Kurman, R. Mortel, P. Schwartz, A. Glass and A. Hildesheim. 2005. Hierarchy of resistance to cervical neoplasia mediated by combinations of killer immunoglobulin-like receptor and human leukocyte antigen loci. *J Exp Med* 201: 1069-1075.

117. R. E. Mebius and G. Kraal. 2005. Structure and function of the spleen. *Nat Rev Immunol* 5: 606-616.

118. Y. Goltsev, N. Samusik, J. Kennedy-Darling, S. Bhate, M. Hale, G. Vazquez, S. Black and G. P. Nolan. 2018. Deep Profiling of Mouse Splenic Architecture with CODEX Multiplexed Imaging. *Cell* 174: 968-981 e915.

119. A. G. N, J. A. Guillen, G. Gallardo, M. Diaz, J. V. de la Rosa, I. H. Hernandez, M. Casanova-Acebes, F. Lopez, C. Tabraue, S. Beceiro, C. Hong, P. C. Lara, M. Andujar, S. Arai, T. Miyazaki, S. Li, A. L. Corbi, P. Tontonoz, A. Hidalgo and A. Castrillo. 2013. The nuclear receptor LXRalpha controls the functional specialization of splenic macrophages. *Nat Immunol* 14: 831-839.

120. M. Kohyama, W. Ise, B. T. Edelson, P. R. Wilker, K. Hildner, C. Mejia, W. A. Frazier, T. L. Murphy and K. M. Murphy. 2009. Role for Spi-C in the development of red pulp macrophages and splenic iron homeostasis. *Nature* 457: 318-321.

121. P. Aichele, J. Zinke, L. Grode, R. A. Schwendener, S. H. Kaufmann and P. Seiler. 2003. Macrophages of the splenic marginal zone are essential for trapping of blood-borne particulate antigen but dispensable for induction of specific T cell responses. *J Immunol* 171: 1148-1155.

122. J. M. den Haan and G. Kraal. 2012. Innate immune functions of macrophage subpopulations in the spleen. *J Innate Immun* 4: 437-445.

123. A. Lanoue, M. R. Clatworthy, P. Smith, S. Green, M. J. Townsend, H. E. Jolin, K. G. Smith, P. G. Fallon and A. N. McKenzie. 2004. SIGN-R1 contributes to protection against lethal pneumococcal infection in mice. *J Exp Med* 200: 1383-1393.

124. P. Seiler, P. Aichele, B. Odermatt, H. Hengartner, R. M. Zinkernagel and R. A. Schwendener. 1997. Crucial role of marginal zone macrophages and marginal zone metallophils in the clearance of lymphocytic choriomeningitis virus infection. *Eur J Immunol* 27: 2626-2633.

125. P. D. Uchil, R. Pi, K. A. Haugh, M. S. Ladinsky, J. D. Ventura, B. S. Barrett, M. L. Santiago, P. J. Bjorkman, G. Kassiotis, X. Sewald and W. Mothes. 2019. A Protective Role for the Lectin CD169/Siglec-1 against a Pathogenic Murine Retrovirus. *Cell Host Microbe* 25: 87-100 e110.

126. G. Pirgova, A. Chauveau, A. J. MacLean, J. G. Cyster and T. I. Arnon. 2020. Marginal zone SIGN-R1(+) macrophages are essential for the maturation of germinal center B cells in the spleen. *Proc Natl Acad Sci U S A* 117: 12295-12305.

127. R. Backer, T. Schwandt, M. Greuter, M. Oosting, F. Jungerkes, T. Tuting, L. Boon, T. O'Toole, G. Kraal, A. Limmer and J. M. den Haan. 2010. Effective collaboration between marginal metallophilic macrophages and CD8+ dendritic cells in the generation of cytotoxic T cells. *Proc Natl Acad Sci U S A* 107: 216-221.

128. Y. Miyake, K. Asano, H. Kaise, M. Uemura, M. Nakayama and M. Tanaka. 2007. Critical role of macrophages in the marginal zone in the suppression of immune responses to apoptotic cell-associated antigens. *J Clin Invest* 117: 2268-2278.

129. G. Kovtunovych, M. A. Eckhaus, M. C. Ghosh, H. Ollivierre-Wilson and T. A. Rouault. 2010. Dysfunction of the heme recycling system in heme oxygenase 1-deficient mice: effects on macrophage viability and tissue iron distribution. *Blood* 116: 6054-6062.

130. A. Bellomo, R. Gentek, R. Golub and M. Bajenoff. 2021. Macrophage-fibroblast circuits in the spleen. *Immunol Rev* 302: 104-125.

131. P. Dutta, F. F. Hoyer, L. S. Grigoryeva, H. B. Sager, F. Leuschner, G. Courties, A. Borodovsky, T. Novobrantseva, V. M. Ruda, K. Fitzgerald, Y. Iwamoto, G. Wojtkiewicz, Y. Sun, N. Da Silva, P. Libby, D. G. Anderson, F. K. Swirski, R.

Weissleder and M. Nahrendorf. 2015. Macrophages retain hematopoietic stem cells in the spleen via VCAM-1. *J Exp Med* 212: 497-512.

132. A. Krmpotic, I. Bubic, B. Polic, P. Lucin and S. Jonjic. 2003. Pathogenesis of murine cytomegalovirus infection. *Microbes Infect* 5: 1263-1277.
133. L. P. Daley-Bauer, L. J. Roback, G. M. Wynn and E. S. Mocarski. 2014. Cytomegalovirus hijacks CX3CR1(hi) patrolling monocytes as immune-privileged vehicles for dissemination in mice. *Cell Host Microbe* 15: 351-362.
134. C. A. Stoddart, R. D. Cardin, J. M. Boname, W. C. Manning, G. B. Abenes and E. S. Mocarski. 1994. Peripheral blood mononuclear phagocytes mediate dissemination of murine cytomegalovirus. *J Virol* 68: 6243-6253.
135. D. A. Katzenstein, G. S. Yu and M. C. Jordan. 1983. Lethal infection with murine cytomegalovirus after early viral replication in the spleen. *J Infect Dis* 148: 406-411.
136. K. M. Hsu, J. R. Pratt, W. J. Akers, S. I. Achilefu and W. M. Yokoyama. 2009. Murine cytomegalovirus displays selective infection of cells within hours after systemic administration. *J Gen Virol* 90: 33-43.
137. J. Trgovcich, D. Stimac, B. Polić, A. Krmpotić, E. Pernjak-Pugel, J. Tomac, M. Hasan, B. Wraber and S. Jonjić. 2000. Immune responses and cytokine induction in the development of severe hepatitis during acute infections with murine cytomegalovirus. *Arch Virol* 145: 2601-2618.
138. J. L. Pollock, R. M. Presti, S. Paetzold and H. W. t. Virgin. 1997. Latent murine cytomegalovirus infection in macrophages. *Virology* 227: 168-179.
139. K. M. Sitnik, F. Krstanovic, N. Godecke, U. Rand, T. Kubsch, H. Maass, Y. Kim, I. Brizic and L. Cicin-Sain. 2023. Fibroblasts are a site of murine cytomegalovirus lytic replication and Stat1-dependent latent persistence in vivo. *Nat Commun* 14: 3087.
140. J. F. Bukowski, B. A. Woda, S. Habu, K. Okumura and R. M. Welsh. 1983. Natural killer cell depletion enhances virus synthesis and virus- induced hepatitis in vivo. *J Immunol* 131: 1531-1538.
141. A. A. Scalzo, N. A. Fitzgerald, C. R. Wallace, A. E. Gibbons, Y. C. Smart, R. C. Burton and G. R. Shellam. 1992. The effect of the Cmv-1 resistance gene, which is linked to the natural killer cell gene complex, is mediated by natural killer cells. *J Immunol* 149: 581-589.

142. A. A. Scalzo, P. A. Lyons, N. A. Fitzgerald, C. A. Forbes, W. M. Yokoyama and G. R. Shellam. 1995. Genetic mapping of *Cmv1* in the region of mouse chromosome 6 encoding the NK gene complex-associated loci Ly49 and musNKR-P1. *Genomics* 27: 435-441.

143. J. E. Grundy, J. S. Mackenzie and N. F. Stanley. 1981. Influence of H-2 and non-H-2 genes on resistance to murine cytomegalovirus infection. *Infect Immun* 32: 277-286.

144. A. A. Scalzo, A. J. Corbett, W. D. Rawlinson, G. M. Scott and M. A. Degli-Esposti. 2007. The interplay between host and viral factors in shaping the outcome of cytomegalovirus infection. *Immunol Cell Biol* 85: 46-54.

145. X. Xie, M. D. Stadnisky and M. G. Brown. 2009. MHC class I Dk locus and Ly49G2+ NK cells confer H-2k resistance to murine cytomegalovirus. *J Immunol* 182: 7163-7171.

146. X. Xie, M. D. Stadnisky, E. R. Coats, M. M. Ahmed Rahim, A. Lundgren, W. Xu, A. P. Makrigiannis and M. G. Brown. 2010. MHC class I D(k) expression in hematopoietic and nonhematopoietic cells confers natural killer cell resistance to murine cytomegalovirus. *Proc Natl Acad Sci U S A* 107: 8754-8759.

147. A. Gamache, J. M. Cronk, W. T. Nash, P. Puchalski, A. Gillespie, H. Wei, L. Gray, M. L. Hammarskjold, W. Xu and M. G. Brown. 2019. Ly49R activation receptor drives self-MHC-educated NK cell immunity against cytomegalovirus infection. *Proc Natl Acad Sci U S A* 116: 26768-26778.

148. A. Gillespie, H. Lee, C. Robertson, M. Cabot and M. G. Brown. 2017. Genome-Wide Exome Analysis of Cmv5-Disparate Mouse Strains that Differ in Host Resistance to Murine Cytomegalovirus Infection. *G3 (Bethesda)* 7: 1979-1984.

149. A. L. Gillespie, J. Teoh, H. Lee, J. Prince, M. D. Stadnisky, M. Anderson, W. Nash, C. Rival, H. Wei, A. Gamache, C. R. Farber, K. Tung and M. G. Brown. 2016. Genomic Modifiers of Natural Killer Cells, Immune Responsiveness and Lymphoid Tissue Remodeling Together Increase Host Resistance to Viral Infection. *PLoS Pathog* 12: e1005419.

150. X. Xie, A. Dighe, P. Clark, P. Sabastian, S. Buss and M. G. Brown. 2007. Deficient major histocompatibility complex-linked innate murine cytomegalovirus immunity in MA/My.L-H2b mice and viral downregulation of H-2k class I proteins. *J Virol* 81: 229-236.

151. A. Dighe, M. Rodriguez, P. Sabastian, X. Xie, M. McVoy and M. G. Brown. 2005. Requisite H2k role in NK cell-mediated resistance in acute murine cytomegalovirus-infected MA/My mice. *J Immunol* 175: 6820-6828.

152. D. Oth, G. Lussier, V. C. Cainelli-Gebara and J. M. Dupuy. 1991. Susceptibility to murine hepatitis virus (type 3)-induced paralysis is influenced by class I genes of the MHC. *European journal of immunogenetics : official journal of the British Society for Histocompatibility and Immunogenetics* 18: 405-410.

153. M. Makino, H. C. Morse, 3rd, T. N. Fredrickson and J. W. Hartley. 1990. H-2-associated and background genes influence the development of a murine retrovirus-induced immunodeficiency syndrome. *J Immunol* 144: 4347-4355.

154. D. N. Cooper, M. Krawczak, C. Polychronakos, C. Tyler-Smith and H. Kehrer-Sawatzki. 2013. Where genotype is not predictive of phenotype: towards an understanding of the molecular basis of reduced penetrance in human inherited disease. *Hum Genet* 132: 1077-1130.

155. A. D. Kenney, J. A. Dowdle, L. Bozzacco, T. M. McMichael, C. St Gelais, A. R. Panfil, Y. Sun, L. S. Schlesinger, M. Z. Anderson, P. L. Green, C. B. Lopez, B. R. Rosenberg, L. Wu and J. S. Yount. 2017. Human Genetic Determinants of Viral Diseases. *Annu Rev Genet* 51: 241-263.

156. M. Makino, H. C. Morse, T. N. Fredrickson and J. W. Hartley. 1990. H-2-associated and background genes influence the development of a murine retrovirus-induced immunodeficiency syndrome. *J Immunol* 144: 4347-4355.

157. L. L. Lanier. 2005. NK Cell Recognition. *Annu Rev Immunol* 23: 225-274.

158. S. Kim, J. Poursine-Laurent, S. M. Truscott, L. Lybarger, Y. Song, L. Yang, A. R. French, J. B. Sunwoo, S. Lemieux, T. H. Hansen and W. M. Yokoyama. 2005. Licensing of natural killer cells by host major histocompatibility complex class I molecules. *Nature* 436: 709-713.

159. J. E. Boudreau and K. C. Hsu. 2018. Natural Killer Cell Education and the Response to Infection and Cancer Therapy: Stay Tuned. *Trends Immunol* 39: 222-239.

160. B. A. Parikh, M. D. Bern, S. J. Piersma, L. Yang, D. L. Beckman, J. Poursine-Laurent, B. Plougastel-Douglas and W. M. Yokoyama. 2020. Control of Viral Infection by Natural Killer Cell Inhibitory Receptors. *Cell Rep* 32: 107969.

161. P. Brodin, K. Karre and P. Hoglund. 2009. NK cell education: not an on-off switch but a tunable rheostat. *Trends Immunol* 30: 143-149.

162. C. Mouse Genome Sequencing, R. H. Waterston, K. Lindblad-Toh, E. Birney, J. Rogers, J. F. Abril, P. Agarwal, R. Agarwala, R. Ainscough, M. Alexandersson, P. An, S. E. Antonarakis, J. Attwood, R. Baertsch, J. Bailey, K. Barlow, S. Beck, E. Berry, B. Birren, T. Bloom, P. Bork, M. Botcherby, N. Bray, M. R. Brent, D. G. Brown, S. D. Brown, C. Bult, J. Burton, J. Butler, R. D. Campbell, P. Carninci, S. Cawley, F. Chiaromonte, A. T. Chinwalla, D. M. Church, M. Clamp, C. Clee, F. S. Collins, L. L. Cook, R. R. Copley, A. Coulson, O. Couronne, J. Cuff, V. Curwen, T. Cutts, M. Daly, R. David, J. Davies, K. D. Delehaunty, J. Deri, E. T. Dermitzakis, C. Dewey, N. J. Dickens, M. Diekhans, S. Dodge, I. Dubchak, D. M. Dunn, S. R. Eddy, L. Elnitski, R. D. Emes, P. Eswara, E. Eyras, A. Felsenfeld, G. A. Fewell, P. Flicek, K. Foley, W. N. Frankel, L. A. Fulton, R. S. Fulton, T. S. Furey, D. Gage, R. A. Gibbs, G. Glusman, S. Gnerre, N. Goldman, L. Goodstadt, D. Grafham, T. A. Graves, E. D. Green, S. Gregory, R. Guigo, M. Guyer, R. C. Hardison, D. Haussler, Y. Hayashizaki, L. W. Hillier, A. Hinrichs, W. Hlavina, T. Holzer, F. Hsu, A. Hua, T. Hubbard, A. Hunt, I. Jackson, D. B. Jaffe, L. S. Johnson, M. Jones, T. A. Jones, A. Joy, M. Kamal, E. K. Karlsson, D. Karolchik, A. Kasprzyk, J. Kawai, E. Keibler, C. Kells, W. J. Kent, A. Kirby, D. L. Kolbe, I. Korf, R. S. Kucherlapati, E. J. Kulbokas, D. Kulp, T. Landers, J. P. Leger, S. Leonard, I. Letunic, R. Levine, J. Li, M. Li, C. Lloyd, S. Lucas, B. Ma, D. R. Maglott, E. R. Mardis, L. Matthews, E. Mauceli, J. H. Mayer, M. McCarthy, W. R. McCombie, S. McLaren, K. McLay, J. D. McPherson, J. Meldrim, B. Meredith, J. P. Mesirov, W. Miller, T. L. Miner, E. Mongin, K. T. Montgomery, M. Morgan, R. Mott, J. C. Mullikin, D. M. Muzny, W. E. Nash, J. O. Nelson, M. N. Nhan, R. Nicol, Z. Ning, C. Nusbaum, M. J. O'Connor, Y. Okazaki, K. Oliver, E. Overton-Larty, L. Pachter, G. Parra, K. H. Pepin, J. Peterson, P. Pevzner, R. Plumb, C. S. Pohl, A. Poliakov, T. C. Ponce, C. P. Ponting, S. Potter, M. Quail, A. Reymond, B. A. Roe, K. M. Roskin, E. M. Rubin, A. G. Rust, R. Santos, V. Sapojnikov, B. Schultz, J. Schultz, M. S. Schwartz, S. Schwartz, C. Scott, S. Seaman, S. Searle, T. Sharpe, A. Sheridan, R. Shownkeen, S. Sims, J. B. Singer, G. Slater, A. Smit, D. R. Smith, B. Spencer, A. Stabenau, N. Stange-Thomann, C. Sugnet, M. Suyama, G. Tesler, J. Thompson, D. Torrents, E. Trevaskis, J. Tromp, C. Ucla, A. Ureta-Vidal, J. P. Vinson, A. C. Von Niederhausern, C. M. Wade, M.

Wall, R. J. Weber, R. B. Weiss, M. C. Wendl, A. P. West, K. Wetterstrand, R. Wheeler, S. Whelan, J. Wierzbowski, D. Willey, S. Williams, R. K. Wilson, E. Winter, K. C. Worley, D. Wyman, S. Yang, S. P. Yang, E. M. Zdobnov, M. C. Zody and E. S. Lander. 2002. Initial sequencing and comparative analysis of the mouse genome. *Nature* 420: 520-562.

163. X. Xie, A. Dighe, P. Clark, P. Sabastian, S. Buss and M. G. Brown. 2007. Deficient major histocompatibility complex-linked innate murine cytomegalovirus immunity in MA/My.L-*H2*^{b} mice and viral downregulation of H-2^{k} class I proteins. *J Virol* 81: 229-236 PMID: 17050600.
164. A. Gillespie, H. Lee, C. Robertson, M. Cabot and M. G. Brown. 2017. Genome-Wide Exome Analysis of Cmv5-Disparate Mouse Strains That Differ in Host Resistance to Murine Cytomegalovirus Infection. *G3*.
165. S. A. Elmore, D. Dixon, J. R. Hailey, T. Harada, R. A. Herbert, R. R. Maronpot, T. Nolte, J. E. Rehg, S. Rittinghausen, T. J. Rosol, H. Satoh, J. D. Vidal, C. L. Willard-Mack and D. M. Creasy. 2016. Recommendations from the INHAND Apoptosis/Necrosis Working Group. *Toxicol Pathol* 44: 173-188.
166. D. Zarcone, E. F. Prasthofer, F. Malavasi, V. Pistoia, A. F. LoBuglio and C. E. Grossi. 1987. Ultrastructural analysis of human natural killer cell activation. *Blood* 69: 1725-1736.
167. S. H. Lee, M. F. Fragoso and C. A. Biron. 2012. Cutting edge: a novel mechanism bridging innate and adaptive immunity: IL-12 induction of CD25 to form high-affinity IL-2 receptors on NK cells. *J Immunol* 189: 2712-2716.
168. S. H. Robbins, M. S. Tessmer, T. Mikayama and L. Brossay. 2004. Expansion and contraction of the NK cell compartment in response to murine cytomegalovirus infection. *J Immunol* 173: 259-266.
169. T. Nabekura and L. L. Lanier. 2016. Tracking the fate of antigen-specific versus cytokine-activated natural killer cells after cytomegalovirus infection. *J Exp Med* 213: 2745-2758.
170. A. Kåse, M. H. Johansson, M. Y. Olsson-Alheim, K. Kärre and P. Höglund. 1998. External and internal calibration of the MHC class I-specific receptor Ly49A on murine natural killer cells. *J Immunol* 161: 6133-6138.
171. N. Kim and H. S. Kim. 2018. Targeting Checkpoint Receptors and Molecules for Therapeutic Modulation of Natural Killer Cells. *Front Immunol* 9: 2041.

172. S. Gill, A. E. Vasey, A. De Souza, J. Baker, A. T. Smith, H. E. Kohrt, M. Florek, K. D. Gibbs, Jr., K. Tate, D. S. Ritchie and R. S. Negrin. 2012. Rapid development of exhaustion and down-regulation of eomesodermin limit the antitumor activity of adoptively transferred murine natural killer cells. *Blood* 119: 5758-5768.

173. J. A. Wagner, P. Wong, T. Schappe, M. M. Berrien-Elliott, C. Cubitt, N. Jaeger, M. Lee, C. R. Keppel, N. D. Marin, J. A. Foltz, L. Marsala, C. C. Neal, R. P. Sullivan, S. E. Schneider, M. P. Keppel, N. Saucier, M. A. Cooper and T. A. Fehniger. 2020. Stage-Specific Requirement for Eomes in Mature NK Cell Homeostasis and Cytotoxicity. *Cell Rep* 31: 107720.

174. L. K. Hanson, J. S. Slater, Z. Karabekian, H. W. t. Virgin, C. A. Biron, M. C. Ruzek, N. van Rooijen, R. P. Ciavarra, R. M. Stenberg and A. E. Campbell. 1999. Replication of murine cytomegalovirus in differentiated macrophages as a determinant of viral pathogenesis. *J Virol* 73: 5970-5980.

175. J. L. Annis, J. B. W. Duncan, H. O. Billcheck, A. G. Kuzma, R. B. Crittenden and M. G. Brown. 2024. Multiple Immune and Genetic Mechanisms Contribute to Cmv5s-Driven Susceptibility and Tissue Damage during Acute Murine Cytomegalovirus Infection. *J Immunol*.

176. O. Soehnlein and L. Lindbom. 2010. Phagocyte partnership during the onset and resolution of inflammation. *Nat Rev Immunol* 10: 427-439.

177. E. Perez-Figueroa, P. Alvarez-Carrasco, E. Ortega and C. Maldonado-Bernal. 2021. Neutrophils: Many Ways to Die. *Front Immunol* 12: 631821.

178. M. Breitzig, C. Bhimineni, R. Lockey and N. Kolliputi. 2016. 4-Hydroxy-2-nonenal: a critical target in oxidative stress? *Am J Physiol Cell Physiol* 311: C537-C543.

179. G. Boivin, J. Faget, P. B. Ancey, A. Gkasti, J. Mussard, C. Engblom, C. Pfirschke, C. Contat, J. Pascual, J. Vazquez, N. Bendriss-Vermare, C. Caux, M. C. Vozenin, M. J. Pittet, M. Gunzer and E. Meylan. 2020. Durable and controlled depletion of neutrophils in mice. *Nat Commun* 11: 2762.

180. S. Baasch, P. Giansanti, J. Kolter, A. Riedl, A. J. Forde, S. Runge, S. Zenke, R. Elling, A. Halenius, S. Brabletz, H. Hengel, B. Kuster, T. Brabletz, L. Cicin-Sain, R. Arens, A. Vlachos, J. C. Rohr, M. P. Stemmler, M. Kopf, Z. Ruzsics and P. Henneke. 2021. Cytomegalovirus subverts macrophage identity. *Cell* 184: 3774-3793 e3725.

181. S. Hamano, H. Yoshida, H. Takimoto, K. Sonoda, K. Osada, X. He, Y. Minamishima, G. Kimura and K. Nomoto. 1998. Role of macrophages in acute murine cytomegalovirus infection. *Microbiol Immunol* 42: 607-616.

182. H. E. Farrell, N. Davis-Poynter, K. Bruce, C. Lawler, L. Dolken, M. Mach and P. G. Stevenson. 2015. Lymph Node Macrophages Restrict Murine Cytomegalovirus Dissemination. *J Virol* 89: 7147-7158.

183. M. K. Selgrade and J. E. Osborn. 1974. Role of Macrophages in Resistance to Murine Cytomegalovirus. *Infection and Immunity* 10: 1383-1390.

184. T. L. McGaha, Y. Chen, B. Ravishankar, N. van Rooijen and M. C. Karlsson. 2011. Marginal zone macrophages suppress innate and adaptive immunity to apoptotic cells in the spleen. *Blood* 117: 5403-5412.

185. X. Liu, Z. Zhan, D. Li, L. Xu, F. Ma, P. Zhang, H. Yao and X. Cao. 2011. Intracellular MHC class II molecules promote TLR-triggered innate immune responses by maintaining activation of the kinase Btk. *Nat Immunol* 12: 416-424.

186. D. J. Mathis, C. Benoist, V. E. Williams, 2nd, M. Kanter and H. O. McDevitt. 1983. Several mechanisms can account for defective E alpha gene expression in different mouse haplotypes. *Proc Natl Acad Sci U S A* 80: 273-277.

187. A. Bhattacharya, M. E. Dorf and T. A. Springer. 1981. A shared alloantigenic determinant on Ia antigens encoded by the I-A and I-E subregions: evidence for I region gene duplication. *J Immunol* 127: 2488-2495.

188. X. Xie, M. D. Stadnisky and M. G. Brown. 2009. MHC class I Dk locus and Ly49G2+ NK cells confer H-2k resistance to murine cytomegalovirus. *J Immunol* 182: 7163-7171.

189. X. Xie, M. D. Stadnisky, E. R. Coats, M. M. Ahmed Rahim, A. Lundgren, W. Xu, A. P. Makrigiannis and M. G. Brown. 2010. MHC class I D(k) expression in hematopoietic and nonhematopoietic cells confers natural killer cell resistance to murine cytomegalovirus. *Proc Natl Acad Sci U S A* 107: 8754-8759.

190. R. L. Wheat, P. Y. Clark and M. G. Brown. 2003. Quantitative measurement of infectious murine cytomegalovirus genomes in real-time PCR. *J Virol Methods* 112: 107-113.